On the Interactions of Magnetic Fluctuations, Zonal Flows, & Microturbulence in Fusion Plasmas

by

Zachary R. Williams

A dissertation submitted in partial fulfillment of
the requirements for the degree of

Doctor of Philosophy

(Physics)

at the

UNIVERSITY OF WISCONSIN–MADISON

2019

Date of final oral examination: 6/28/2019

The dissertation is approved by the following members of the Final Oral Committee:
Paul W. Terry, Professor, Physics
John S. Sarff, Professor, Physics
Carl R. Sovinec, Professor, Engineering Physics
Chris C. Hegna, Professor, Engineering Physics

To Russ, Karen, Sarah, Adam, Anna, Jesse, and Bethany

"It is a right, yes a duty, to search in cautious manner for the numbers, sizes, and weights, the norms for everything God has created. For He himself has let man take part in the knowledge of these things ... For these secrets are not of the kind whose research should be forbidden; rather they are set before our eyes like a mirror so that by examining them we observe to some extent the goodness and wisdom of the Creator."

- Johannes Kepler

ACKNOWLEDGMENTS

My first and foremost thanks goes to Paul Terry, who plucked a graduate student panicked about funding out of his trouble with an offer for a summer research gig, and has since been a priceless teacher, mentor, and guide. Infinite thanks also to M.J. Pueschel, whose patience and willingness to address my many, many questions on the path of teaching me how to do research is one of the primary reasons I made it all the way through grad school.

Thank you to Jim Reardon, who very early on in my graduate career recognized in me an interest and aptitude for teaching, and was always intentional about fostering and encouraging that interest. I am very fortunate to have pursued this passion and now begin a career in it, due in no small part to your investment.

A very special thanks to all members of the Cascave: Adrian, Ben, Garth, Ian, Jason, and Justin. Thank you all for the productive discussions, and more importantly for the friendships in the office that kept me sane over the years.

To the incoming class of 2013 physics graduate students (the Best years), thank you for being a fantastic community of fast friends. We survived the qual, the core courses, and figuring out the slight beginnings of what adult life might look like. I'm glad to have shared this journey with each of you.

Thank you to my church families, both at Blackhawk Church here in Madison and Summit Church in Orlando, Florida. I could write an entire separate thesis expressing the incredible value you have added to my life over the years, and that still would not be enough to adequately convey my gratitude.

To my hometown crew: Albert, David, Justin, Karl, Matthew, and Timmy. I am thankful for lifelong friendships that have continued through graduate school, and I'm sure will remain for many years to come.

Finally, I want to thank my family, all of whom have supported me in this long journey from the beginning, and have never failed to remind me that I have what it takes.

CONTENTS

LIST OF TABLES

LIST OF FIGURES

ABSTRACT

An understanding of how turbulence affects transport levels in magnetic confinement fusion devices is essential in working towards the goal of sustainable fusion energy. The primary focus of this thesis is to analyze the fundamentally multi-scale nature of the interaction between large-scale magnetic fluctuations and small-scale microturbulence.

This interaction manifests on the Madison Symmetric Torus Reversed-Field Pinch (MST RFP), in which large-scale tearing instabilities dominate standard discharges. When operating in an improved-confinement regime called Pulsed Parallel Current Drive, tearing mode activity is reduced, resulting in an increase in gradients towards the edge of the device that drive microturbulence. Radially local flux-tube gyrokinetic simulations using the GENE code show that an accurate characterization of microturbulence requires an inclusion of tearing mode fluctuations. In the absence of tearing effects, the reversed-field pinch produces strong zonal flows that completely quench turbulence and transport; there are multiple potential contributors to this unique zonal-flow-dominated regime discussed in this work, including the role of collisionality, Rosenbluth-Hinton residuals, and secondary instability. When modeling tearing mode effects into the simulation through an ad-hoc, constant-in-time perturbation, the zonal structures degrade and transport increases to values in much closer agreement with experiment. This observation is described through the physical picture of magnetic-flutter-induced zonal flow erosion, expressed previously via analytic theory.

These findings of the importance of interactions between tearing modes, zonal flows, and microturbulence in the MST RFP motivated additional study to determine if this behavior generalized to other fusion confinement configurations, or was merely an artifact of the RFP. To this end, a dedicated run campaign was performed on the DIII-D tokamak to determine how microturbulence varies with the application of a Resonant Magnetic Perturbation (RMP). RMPs, which are typically used in ELM suppression, serve an analogous role to tearing modes in the RFP as a source of large-scale magnetic fluctuations. Beam Emission Spectroscopy observes density fluctuations at microturbulent frequencies that increased directly with RMP amplitude, agreeing with expectations set by the RFP work. Gyrokinetic simulations find comparable scaling with microturbulent density fluctuations, and identify a corresponding zonal flow erosion with application of an RMP, further confirming the presence of a common underlying physics mechanism governing these seemingly very different fusion plasmas.

To further study this underlying physics mechanism and work towards a more physically accurate model of current-gradient-driven tearing fluctuations, the GENE code is modified by including in the governing equations an equilibrium current gradient. The tearing mode driven by this current gradient is seen in benchmarks to agree very well with analytic theory. A simple slab system unstable to tearing modes and slab ITG is studied gyrokinetically. Nonlinear simulations of this system are characterized by distinct separation of scales, both spatially and temporally, with ITG effects dominating in early times, and tearing mode dynamics dominating later on. Signatures of zonal flow degradation due to tearing effects and their subsequent effect on microturbulence are also present.

While the bulk of this thesis studies magnetic effects at large scales, electromagnetic instabilities can also occur at micro-scales; one important example of this relevant to fusion plasmas is the microtearing mode. While traditionally assumed to require finite collisionality for instability, recent work has demonstrated that finite growth rate microtearing persists even in the collisionless limit, and can be driven by magnetic curvature drifts. The final portion of this thesis presents an analytic calculation examining how magnetic curvature might modify microtearing growth rates.

1 INTRODUCTION

1.1 Plasma Physics: Working Towards An Energy Solution

As technology continues to advance and becomes more and more integrated into everyday life, humankind's energy consumption needs will only continue to grow commensurately. As this demand for energy increases, the finite nature of the current dominant source of energy, fossil fuels, becomes more apparent. Current estimates based on 2017 production and consumption rates predict oil and natural gas reserves to be depleted in 50 years time, and coal reserves depleted in just over a century (BP Statistical Review of World Energy, 2018) . The issue of the limited supply of fossil fuels needs addressing in the immediate future, rather than waiting until the supply runs out. Additionally, the use of fossil fuels damages the environment in soon-to-be permanent ways through the emission of greenhouse gases (Edenhofer et al., 2012), thus presenting a danger to humankind. These reasons motivate the pursuit of an alternative source of energy, one that is abundantly occurring in nature and does not present a danger through its consumption. While there is an increased usage with alternative clean energy sources such as wind, solar, and hydro, these run into issues of being unable to keep up with energy demands and are dependent upon environmental variables such as sunlight or the presence of significant winds.

Finding an energy source that is not subject to any of these described shortcomings is a challenging yet vitally important task. Nuclear fusion, in which a small amount of matter is converted into energy, presents itself as an attractive option that seems to check all of these boxes. Naturally occurring in the core of our sun and all stars, nuclear fusion takes place when nuclei have sufficiently large energy to overcome Coulomb repulsion and combine to produce a larger nucleus. While in principle possible for any given nuclei in the right conditions, this reaction results in a release of energy only for lighter nuclei. In the context of fusion energy, the most attainable reaction is that of deutrium and tritium, which results in an α particle and an energetic neutron, described below in Eq. (1.1). The 17.6 MeV of energy arises from the slight difference in mass between the products and reactants, which is converted to a large amount of energy as described by Einstein's famous relation $E = mc^2$.

$$ {}^{2}_{1}\mathrm{H} + {}^{3}_{1}\,\mathrm{H} \rightarrow \underbrace{{}^{4}_{2}\mathrm{He} + 3.5\ \mathrm{MeV}}_{\alpha\ \text{particle}} + \underbrace{{}^{1}_{0}\mathrm{n} + 14.1\ \mathrm{MeV}}_{\text{energetic neutron}} \tag{1.1} $$

Nuclear fusion very readily addresses many of the shortcomings present in other energy sources. As a fuel source, deuterium is incredibly abundant, naturally occurring to one part in ≈ 6500 in ocean water. Tritium is not naturally abundant, but can be bred from lithium. With regards to environmental safety, nuclear fusion will have a significantly smaller carbon footprint. While tritium is a radioactive material, its half-life is significantly shorter ($\approx$ 12 years) than any of the radioactive waste products involved in nuclear fission, fusion's nuclear energy competitor. This makes fusion a much safer and more sustainable option. Achieving nuclear fusion is independent of environmental factors, so an ideal fusion reactor could operate continuously and produce energy uninhibited by external conditions. Currently, fusion technology is not yet anywhere near the stage of reactor-like energy production. Reaching this point is a primary motivator behind the field of plasma physics.

In order for the reaction described in Eq. (1.1) to occur, the hydrogen nuclei must have sufficiently large kinetic energy to overcome the electrostatic repulsion. This required energy is significantly greater than the 13.6 eV binding energy of an electron in a hydrogen atom, meaning that the electrons previously bound to the hydrogen nuclei are now decoupled. The resultant substance is a fluid of positively charged ions and negatively charged electrons, which characterizes the fourth state of matter referred to as *plasma*. In light of this, a pursuit of nuclear fusion is intimately connected to an understanding of plasma physics.

Plasmas, as previously mentioned, consist of matter in which constituent atoms have broken apart into ions and electrons. Beyond this, a specific defining attribute of plasmas is that of collective behavior, meaning that the plasma system size and density are such that individual particle effects are shielded out over a small scale, allowing collective effects to dominate. This small scale can be more quantitatively described as the length over which the potential generated by an individual charge is shielded to $1/e$ of it's original value, and is referred to as the *Debye Length* (commonly denoted as λ_{D}). To consider a plasma a collective medium, it must have a characteristic size L much larger than the debye length, or $L/\lambda_{\mathrm{D}} \gg 1$. A similar way to state this condition of collective behavior dominating individual effects is to require a density n of particles within a sphere with a debye-length radius such that $n\lambda_D^3 \gg 1$ (this ratio sometimes is referred to as the "plasma parameter"). Standard fusion plasma experiments have a Debye length on the order of $\lambda_{\mathrm{D}} \sim 10^{-4}$ meters, are themselves on the order of $L \sim 1$ meter in size, and have densities around $n \sim 10^{-19} m^{-3}$, and as such fall well within these defining limits[1].

---

[1] Other limits, such as relativistic or quantum, are of relevance to some astrophysical plasma scenarios but will not arise in this work

1.2 Basic Principles of Magnetic Plasma Confinement

Fusion reactors will require working with matter in the plasma state, so designing reactors capable of confining plasmas is of great importance. There are two primary approaches to plasma confinement: 1) using intense lasers to apply large amounts of pressure on deuterium pellets, which is referred to as inertial confinement, and 2) using magnetic fields to confine charged particles to circular orbits around field lines, which is called magnetic confinement. This theses focuses only on the latter, and this section will explore the basics of how plasmas behave in magnetically confined systems.

Single Particle Motion

Magnetic fields exert a force on moving charged particles, given by $q\mathbf{v}\times\mathbf{B}$ (where boldface will denote vector quantities throughout this text), which results in circular orbits perpendicular to field lines (without having any effect on the motion parallel to the field). This gyration occurs at a frequency of $\omega_c = q_j B/m_j$, called the *cyclotron frequency*, where q_j and m_j refer to the charge and mass of the particle with species index j, and B is the magnetic field strength. Because of this, charged particle motion in a strong magnetic guide field can be broken into two parts: the fast gyromotion around the field line, and the remaining particle motion that is independent of the former, which will be referred to as the *guiding center motion*. In addition to streaming freely along magnetic field lines, the guiding center also undergoes additional motion that can be caused by a number of different forces; these are referred to as drifts and will be briefly discussed.

As a first, important example of guiding center drift motion, consider a charged particle subject to both electric and magnetic fields. The equation of motion for such a particle is given by:

$$\frac{d\mathbf{v}}{dt} = \frac{q}{m}(\mathbf{E} + \mathbf{v}\times\mathbf{B}) \tag{1.2}$$

Define orthogonal coordinates (x, y, z) such that $\hat{\mathbf{z}}$ aligns with the background magnetic field line, $\hat{\mathbf{y}}$ follows the component of the electric field line perpendicular to the magnetic field, and $\hat{\mathbf{x}}$ and $\hat{\mathbf{y}}$ are perpendicular to both the field line and one another such that $\hat{\mathbf{x}}\times\hat{\mathbf{y}} = \hat{\mathbf{z}}$ (a common convention that will be used throughout this thesis). The motion of the particle parallel to the magnetic field line will only be affected by an electric field component that aligns with that motion, resulting in simple acceleration in the field line direction. The equations describing motion perpendicular to the field line (in the **x** and **y** directions) then appear as:

$$\frac{dv_x}{dt} = \omega_c v_y \qquad \frac{dv_y}{dt} = \frac{q}{m}E - \omega_c v_x. \tag{1.3}$$

Upon solving, one finds

$$v_x = v_\perp \sin(\omega_c t + \theta) + \frac{E}{B} \qquad v_y = v_\perp \cos(\omega_c + \theta), \tag{1.4}$$

where $v_\perp$ and θ are the magnitude of the gyration velocity and the gyrophase angle, respectively, and depend upon initial conditions. In addition to the oscillatory behavior of the gyromotion, there is another drifting motion of the guiding center caused by the electric field in the x direction, referred to as the $\mathbf{E} \times \mathbf{B}$ drift, named so due to its vector equation definition:

$$\mathbf{v}_{E\times B} \equiv \frac{\mathbf{E} \times \mathbf{B}}{B^2}. \tag{1.5}$$

This approach to calculating drifts generalizes to any force $\mathbf{F}$ perpendicular to the magnetic field acting on a charged particle, by replacing $\mathbf{E}$ in the above equations with $\mathbf{F}/q$. A few such drifts include the ∇B drift, arising from variation in a particle's gyro-radius as it samples regions of different magnetic field strength over one gyro-orbit in a non-uniform magnetic field:

$$\mathbf{v}_{\nabla B} = \frac{v_\perp^2}{2\omega_c B^2}\mathbf{B} \times \nabla B, \tag{1.6}$$

or the curvature drift, which is produced by centrifugal forces felt by guiding centers traveling along curved magnetic field lines:

$$\mathbf{v}_c = \frac{v_\parallel^2}{\omega_c B}\mathbf{B} \times \hat{\mathbf{b}} \cdot \nabla \hat{\mathbf{b}}, \tag{1.7}$$

where $\hat{\mathbf{b}}$ is the unit vector pointing along the magnetic field (a generalization of the aforementioned $\hat{\mathbf{z}}$ direction to curved field lines). One important distinction between the equation for $v_{\mathbf{E}\times\mathbf{B}}$ and the equations for the other drifts is the absence of the charge (which is present in the other equations through the gyrofrequency). This means that $\mathbf{E} \times \mathbf{B}$ drifts occur in the same direction for both ions and electrons in a plasma, and thus characterize bulk plasma

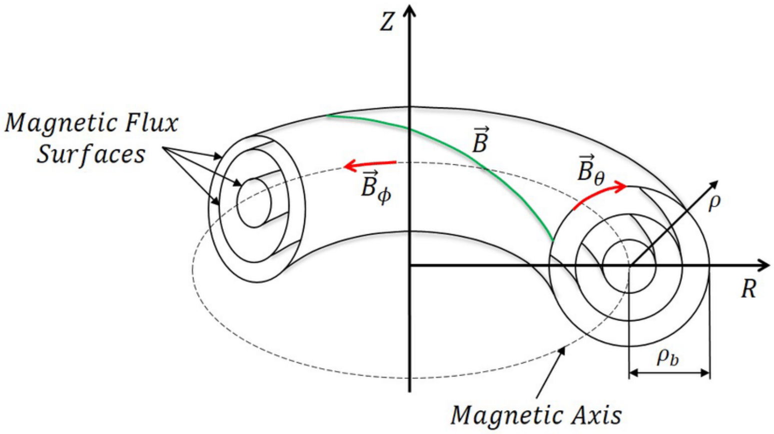

Figure 1.1: A schematic drawing of a toroidal configuration with well-defined nested flux surfaces. B_θ points in the poloidal direction (the short way around), B_ϕ points in the toroidal direction (long way around), and the green line represents the complete helical magnetic field. Taken from (Barton et al., 2015).

flows. Equipped with some basic concepts behind how particle motions behave in magnetic confinement configurations, one can now consider the design of fusion devices.

Toroidal Fusion Device Configurations

Given that charged particles are confined to zeroth order in directions perpendicular to magnetic field lines, a reasonable approach to designing a magnetic fusion reactor is to create a straight-line cylindrical device that generates magnetic fields along its length. However, particles heated to the kinetic energies required for fusion move with very high thermal velocity (for example, a 1 keV hydrogen ion will travel at a speed of 438 km/s), and will thus stream uninhibited along field lines out of the ends of the linear device on very fast time scales, resulting in poor confinement. One can either design unrealistically long fusion devices ($\sim$ 500 km long to confine an ion for one second), or mitigate end losses by "closing" field lines off and bending the device into a donut-like shape called a *torus*. The torus is characterized by three directions: a radial direction (analogous to how one would define it for a cylinder), a poloidal direction (the "short way" around), and a toroidal direction (the "long way" around), denoted commonly by (ρ, θ, ϕ) respectively; see Figure 1.1 for a visual representation.

While effectively addressing the issue of end losses through the creation of a torus, this configuration is not without its own inherent confinement issues. One prominent issue is the existence of the previously-discussed magnetic drifts. In a device with purely toroidally directed magnetic field, both curvature and grad-B drifts are present which result in vertical motion of particles, by which a fraction of the previously-confined particles are lost. Ions and electrons drift in opposite directions under these curvature and grad-B effects. This charge separation produces a large electric field which in turn produces an $E \times B$ drift that can lead to substantial losses. These harmful drifts can be mitigated to a large extent by introducing a poloidally-directed component to the field also shown in Fig. 1.1, so that the total magnetic field winds helically around the torus. A measure of the pitch of this helical magnetic field line is given by the *safety factor*, which is defined as

$$q \equiv \frac{rB_\phi}{RB_\theta}, \tag{1.8}$$

where r and R are major and minor radius, respectively, as depicted in Fig. 1.1, B_ϕ and B_θ refer to toroidal and poloidal field strength, respectively, and the magnetic field is assumed to lie in toroidal surfaces (refer back to Fig. 1.1). This quantity is of great importance for assessing stability conditions in toroidal fusion devices, and is referenced in many places throughout this thesis. For most toroidal configurations, such as the tokamak, $B_\phi \gg B_\theta$. One prominent exception is in the reversed-field pinch (RFP), where $B_\theta \gtrsim B_\phi$, resulting in a significantly different safety factor and consequently different physics governing the plasma state. Both the reversed-field pinch and the tokamak are studied in this work, and will be discussed in Chapters 3 and 4, respectively.

The Issue of Confinement – Magnetic Equilibrium and Stability

Now equipped with a device configuration in which one can confine a plasma for fusion, it is vital to find ways to describe what plasma confinement looks like functionally, and what issues arise with confinement. This is by no means a comprehensive discussion of magnetically confined equilibrium stability (of which there exists a large body of literature, see (Freidberg, 2014) for an in-depth review) but rather a brief survey of central topics to provide context and a conceptual framework for the rest of the thesis.

In toroidal devices, a helical magnetic field configuration as discussed in the previous section can result in the formation of nested *flux surfaces*. A flux surface corresponds to a smooth two-dimensional surface mapped out by a magnetic field line $\mathbf{B}$ such that for a vector $\hat{\mathbf{n}}$ normal to the surface, it holds that

$$\mathbf{B} \cdot \hat{\mathbf{n}} = 0. \tag{1.9}$$

An example of well-defined nested flux surfaces is shown in Fig. 1.1; note that in general flux surfaces need not have a circular cross section. A toroidal plasma consisting of well-defined magnetic flux surfaces forms a good starting point from which to define an equilibrium. One very effective way of describing fusion plasma equilibria is to use the equations of MagnetoHydroDyanmics (MHD), which models plasmas as a continuous charged fluid that interacts with and generates magnetic and electric fields. There are many distinct regimes for MHD equations; for the sake of a conceptual sketch, only the simple ideal MHD equations are shown here:

$$\partial_t \rho + \nabla \cdot (\rho \mathbf{v}) = 0, \tag{1.10}$$

$$\rho \left(\partial_t \mathbf{v} + \mathbf{v} \cdot \nabla \mathbf{v} \right) = -\nabla p + \mathbf{J} \times \mathbf{B}, \tag{1.11}$$

$$\partial_t p + \mathbf{v} \cdot \nabla p + \gamma p \nabla \cdot \mathbf{v} = 0, \tag{1.12}$$

$$\partial_t B - \nabla \times \left(\mathbf{v} \times \mathbf{B} \right) = 0. \tag{1.13}$$

where ρ, $\mathbf{v}$, p, and $\mathbf{J}$ refer to fluid density, velocity, pressure, and current density, respectively. A representation of an equilibrium plasma state is arrived at by taking $\partial_t \to 0$ and $\mathbf{v} = 0$, one arrives at the condition of $\mathbf{J} \times \mathbf{B} = \vec{\nabla} p$, which upon comparison to equation (1.9) shows that equilibrium flux surfaces are surfaces of constant plasma pressure.

To assess confinement properties, one can introduce a small perturbation to the equilibrium equations and calculate how the plasma will respond. These perturbations generally propagate as waves in the plasma, and either grow, decay, or stay the same with time evolution. A perturbation that grows with time is called an *instability*; the characterization of plasma instabilities is the subject of significant study in the context of of fusion plasmas and will come up frequently throughout this work. In an equilibrium state, there is no appreciable loss of particles or energy. However, a perfect equilibrium state is not achievable in experiment, and fusion plasmas will always be subject to small perturbations that will result in instabilities, which subsequently generate turbulence that drives particles and energy out of the confining device, discussed more in depth in Section 1.3.

Name	Free Energy Source	Spatial Scale
ITG Mode	∇T_{i}	$k_y\rho_{\mathrm{i}} \sim 0.1 - 1$
ETG Mode	∇T_{e}	$k_y\rho_{\mathrm{i}} > 1$
TEM	∇T_{e}, ∇n	$k_y\rho_{\mathrm{i}} \sim 0.1 - 1$
MTM	∇T_{e}	$k_y\rho_{\mathrm{i}} \sim 0.1 - 1$

Table 1.1: Common drift-wave instabilities in fusion plasmas. The acronyms stand for Ion Temperature Gradient, Electron Temperature Gradient, Trapped Electron Mode, and Microtearing Mode, respectively. ITG and TEM instabilities will feature prominently throughout this work. MTMs, while always depending on ∇T_{e}, can vary significantly with collisionality, as explored in Chapter 6.

Drift Wave Instabilities

Before a discussion of turbulence in fusion devices and its effect on confinement, it is instructive to briefly survey a class of instabilities called drift-wave instabilities that commonly arise in fusion plasmas and will be referred to throughout the thesis. As mentioned previously, instabilities are perturbations from equilibrium that grow under certain plasma conditions; the energy for instabilities generally comes from gradients in certain quantities that exist as part of the plasma equilibrium. One such class of instabilities is driven by pressure gradients and referred to as *drift-wave* instabilities. Since a fusion reactor requires high temperatures and densities in the core but tends towards room temperature at the wall, pressure gradients are unavoidable and thus drift waves are also commonly referred to as *universal instabilities*. See Table 1.1 for a list of common drift-wave instabilities.

Many of the common drift waves occur at ion-gyroradius scales, denoted by $k_y\rho_{\mathrm{i}} \sim 0.1 - 1$ (where $\rho_{\mathrm{i}} \equiv v_t/\omega_{\mathrm{c}}$ is the ion gyroradius at a thermal velocity v_t). ITG and TEM are two prominent microinstabilites that occur at these scales in a large range of fusion devices, including tokamaks (Ernst et al., 2004; Told et al., 2013), stellarators (Faber et al., 2015; Helander et al., 2015; Watanabe et al., 2008), and RFPs (Carmody et al., 2013, 2015; Tangri et al., 2011; Predebon and Sattin, 2013; Predebon and Xanthopoulos, 2015). Though these instabilities are primarily localized to ion-scale dynamics, their effects need not be constrained only to those spatial scales, as will be discussed later.

1.3 Transport and Turbulence in Fusion Plasmas

Establishing an economical fusion reactor requires containing a plasma of a sufficient temperature and density for long enough that the energy required to heat the plasma is exceeded by the output from the nuclear fusion process. Beyond that, a desirable reactor will reach the point of *ignition*, in which after an initial input of energy, the energy from the α particles generated in the fusion reaction is sufficient to self-sustain the reaction. The required combination of density n, temperature T, and confinement time τ for plasma ignition is referred to as the "fusion triple product" or the *Lawson Criterion* (Lawson, 1957), and is given by

$$nT\tau \geq 3 \times 10^{21} \text{ keV s/m}^3 \tag{1.14}$$

for deuterium-tritium fusion. In light of this, the efforts of fusion plasma physics can be loosely categorized into 1) achieving as large of a plasma pressure as possible (maximize n and T), and 2) confining the plasma for as long as possible (maximize τ). While both are of great importance, this thesis focuses in on the second category, through the pursuit of a deeper understanding of plasma *transport*.

Formally speaking, transport can refer to the bulk motion of particles or energy in any arbitrary direction; however, this work will examine transport to specifically describe radial motion, as that is most relevant for confinement. The earliest estimates of fusion transport depicted particle loss as a random-walk process, in which the characteristic step size was a gyroradius, $\Delta x = \rho_{\text{i}}$, and the diffusive time scale was attributed to collisionality of the plasma $\Delta\tau_{\text{diff}}^{-1} \sim \nu_{\text{c}}$. As random-walk diffusivity scales as (characteristic step)^2/(characteristic time), this model predicted diffusivity (a measure of transport rates) to scale as $\rho^2\nu_c \propto B^{-2}$, in which diffusive losses would decrease rapidly as magnetic field strength was increased. This prediction bodes well for large confinement times, as very low diffusion could be achieved at reasonable magnetic field strengths. However, observed transport scaling did not match these expectations at all. Instead, it has been noted that a significant portion of transport in fusion devices is attributable to what was called "anomalous transport", (Liewer, 1985). This deviation from classical diffusion that contributes so significantly to transport levels comes from plasma *turbulence*.

Turbulence

A complete mathematical description (and the full understanding that accompanies it) of turbulence is one of the most important remaining open questions in the field of classical physics. While there is not a universally agreed-upon definition, turbulence can loosely be defined as the dynamic nonlinear behavior of a fluid that couples a wide range of distinct spatial scales and distributes energy across those scales. In an attempt to elucidate this idea of turbulence, consider a dynamical variable $f(x, y, z, t)$ described by the following schematic evolution equation:

$$\partial_t f(\mathbf{x}, t) = \mathcal{L} f(\mathbf{x}, t) + \partial_x f(\mathbf{x}, t) \partial_y f(\mathbf{x}, t). \tag{1.15}$$

The variable f could describe a variation in a plasma flow from the MHD equations, or a perturbed plasma distribution function from kinetic theory (in which case it would also have velocity-space dependence; see chapter 2 for more detail). This equation for the quantity f has two terms on the right-hand side, one which is linear in f and another which is *nonlinear*. The importance of this distinction becomes more evident when examining the equation in Fourier space:

$$\partial_t f(\mathbf{k}, t) = \underbrace{\mathcal{L}_k f(\mathbf{k}, t)}_{\text{linear}} + \underbrace{\sum_{\mathbf{k}'} C_{k,k'} f(\mathbf{k}', t) f(\mathbf{k} - \mathbf{k}', t)}_{\text{nonlinear}} . \tag{1.16}$$

Suppose the quantity f is initially small (as in the case of describing a small perturbation from an equilibrium). In this case the second term in Eq. (1.16) can be neglected, and what remains is a linear differential equation whose solution is just the exponential function, noting that $\mathcal{L}_k$ can result in a frequency that is complex and thus solutions can grow or decay in time. Importantly, in this state, the solution at a given spatial scale $\mathbf{k}$ depends only on the dynamics of that spatial scale, i.e., there is no interaction of dynamics at different scales. In the case of an exponentially growing solution, one is in a state of linear instability, for example a drift-wave instability. Once f grows sufficiently large, the second term in Eq. (1.16) is no longer negligible. At this point, the system changes into the nonlinear state, and subsequently the dynamics at a given spatial scale $\mathbf{k}$ are, in general, dependent on every other spatial scale $\mathbf{k}'$ through the convolution. This state in which the dynamics at every spatial scale is dependent upon the dynamics at every other spatial scale is generally referred to as turbulence.

Because the linear instability is driven through some free energy (a density or temperature gradient in the drift-wave case), as long as the free energy source persists, the linear term will attempt to add energy at the scale $\mathbf{k}$, while the nonlinear term will distribute energy away from the spatial scale $\mathbf{k}$ and into other scales. When these two terms balance, one

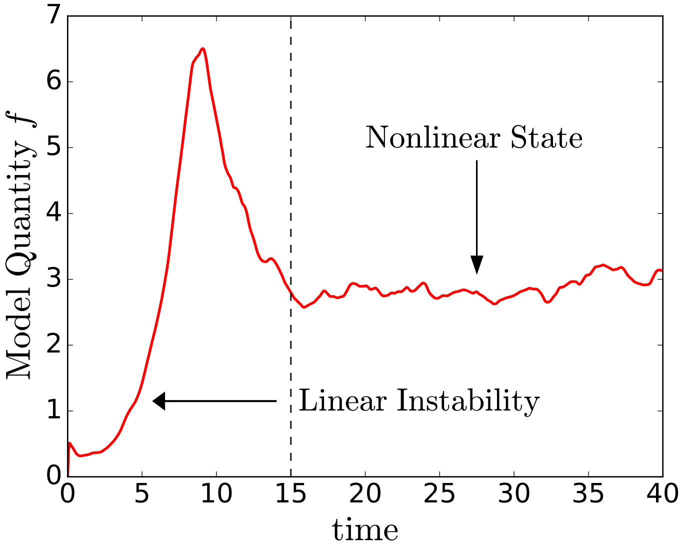

Figure 1.2: A time trace of the solution from the a computational gyrokinetics model, showing distinct states of linear instability and saturated turbulence. The quasi-stationary state is defined here from time = 15 to the end, and used to determine time-averaged transport quantities.

arrives at a state where $\partial_t f \approx 0$ on time average; this is referred to as a *quasi-stationary state*. This process is depicted in Fig. 1.2. This quasi-stationary state allows transport levels to be quantified.

Transport

As mentioned in the beginning of this section, an important goal of magnetic confinement fusion is achieving long confinement times; this is synonymous with minimizing the amount of transport that occurs in the plasma. Fluctuations caused by turbulence contribute significantly to plasma transport; quantifying turbulent transport in certain plasma regimes will be a central focus of this thesis. Transport can be quantified with the following definitions for particle and heat (radial) *flux*:

$$\Gamma \equiv - \langle v_r n \rangle \ , \tag{1.17}$$

$$Q \equiv - n_0 \langle v_r T \rangle \ , \tag{1.18}$$

where Γ and Q are particle and heat flux, respectively, v_r, n, T refer to turbulent fluctuations in radial flow, density, and temperature, n_0 is the equilibrium density, and the angle brackets refer to ensemble averaging. The radial flow v_r can be broken into two components: electrostatic flow $v_r^{\mathrm{ES}} \propto \partial_y \Phi$ and electromagnetic flow $v_r^{\mathrm{EM}} \propto \partial_y A_\parallel \propto B_x$. The electrostatic component is radial $E \times B$ flow driven by fluctuations in Φ, and the electromagnetic component is due to parallel streaming of particles along radially perturbed magnetic field lines. Net transport from these different parts of the radial flow define electrostatic vs. electromagnetic flux, a convention used throughout this thesis. Using the above relation, the fluctuating radial velocity in Eqs. (1.17) and (1.18) can be replaced by fluctuations in $\partial_y \Phi$ and $\partial_t A_y$ for electrostatic and electromagnetic components. As an example, the electrostatic particle and heat flux can be written (in Fourier space) as:

$$\Gamma = \sum_k \Gamma_k = \sum_k \langle i k_y \Phi n \rangle \tag{1.19}$$

$$Q = \sum_k Q_k = \sum_k \langle i k_y \Phi T \rangle \tag{1.20}$$

In this form, it is apparent that quantifying fluxes is equivalent to quantifying turbulent fluctuations in electromagnetic fields, density, and temperature. The value for transport in a given calculation is determined from the time-averaged fluxes over a quasi-stationary state (refer back to Fig. 1.2). When the state has fully transitioned from the linear growth phase into a sufficiently long quasi-stationary state, the turbulence is described as being *saturated.* Determining the mechanisms by which turbulence saturates, as well as predicting the transport levels of a saturated turbulent state, are essential to the study of transport.

The Significance of Multi-scale Interactions in Turbulence and Transport

As transport is produced by turbulent fluctuations, it is reasonable to expect that cross-scale dynamics, which are fundamental to turbulence, play a significant role in setting transport levels. In magnetically confined plasmas, ions and electrons differ in gyroradius by a factor of $\sqrt{m_{\mathrm{i}}/m_{\mathrm{e}}}$, and thus their corresponding spatial scales of dynamical relevance are separate by a factor of 60, due to their difference in gyroradii. Historically, analytic and numerical methods for studying plasma transport were limited in the range over which scales were studied, describing ion transport by only looking at the dynamics of the plasma at ion scales ($k_y \rho_{\mathrm{i}} \sim 0.1 - 1$, where y corresponds to binormal direction), and electron transport much the same way. However, more recent work (Holland and Diamond, 2004; Maeyama et al., 2015; Howard et al., 2016) has demonstrated that despite significant separation in spatial scales, there are nontrivial physical effects present in the interaction between these disparate scales that is necessary to include in models to accurately predict turbulence and transport levels.

In addition to the existence of disparate ion and electron scales, larger-than-ion-scale dynamics can also be of great importance in fusion plasmas. Consequently, when considering the relevance of multi-scale interactions for accurately modeling fusion plasma turbulence, additional cross-scale interactions that take place between ion scales and larger scales characteristic of MHD fluctuations should also be considered. Recent work (Williams et al., 2017) has demonstrated the significance of the interactions between magnetic fluctuations occurring at large scales, turbulent fluctuations at ion scales, and zonal flows, which are electrostatic potential structures constrained to flux surfaces that play an essential role in transport regulation, to be discussed more thoroughly in Chapter 2. The physics involved in this interaction, how it affects turbulence and transport levels, and how it manifests in a variety of different plasma configurations, is the underlying theme for the rest of this work.

1.4 Thesis Outline

The rest of the thesis will proceed as follows: Chapter 2 will provide a survey and discussion of plasma physics topics of relevance to the rest of the thesis, including tearing modes, zonal flows, and gyrokinetics. Chapter 3 presents gyrokinetic modeling results of the interaction of magnetic fluctuations, microturbulence, and zonal flows as they manifest in the Madison Symmetric Torus Reversed-Field Pinch through tearing modes and ∇n-TEM instability. In Ch. 4, drift wave fluctuations in the DIII-D tokamak are modeled with gyrokinetic simulations studied to better understand the underlying physics of the interactions of Resonant Magnetic Perturbations and ITG microturbulence. A simplified slab system is examined in Ch. 5, which is attained by the introduction of a current gradient into the gyrokinetics code GENE, allowing for the self-consistent development of tearing modes from a plasma equilibrium, as well as more completely capturing how tearing modes and microturbulence act on and react to one another. Chapter 6 develops an analytic theory for a curvature-driven microtearing mode in the collisionless limit as seen in gyrokinetic simulations. The contents of this thesis are is then summarized in Ch. 7.

2 BACKGROUND AND THEORY CONCEPTS

Before investigating the interaction between large-scale magnetics and microturbulence in later chapters, this chapter surveys a few important underlying concepts that drive the discussion for the rest of the thesis. Within the context of multi-scale interactions, one physics phenomenon is of central importance to this work: magnetic-flutter-induced zonal flow erosion. To understand this phenomenon, it is instructive to first briefly review the core concepts of zonal flows, their connection to microturbulence, and tearing modes. These concepts are then combined to describe the aforementioned zonal flow erosion mechanism. Additionally, the vast majority of the results presented in this thesis arise from computations based on the gyrokinetics. As such, the chapter includes a summary of the gyrokinetic framework and an overview of the GENE code.

2.1 Zonal Flows and Tearing Modes

Zonal Flows

Zonal flows[1] are large-scale $m = n = 0$ (where m and n are poloidal and toroidal mode numbers, respectively) structures in electrostatic potential Φ. These structure are constant within flux surfaces, but the variation of Φ across different flux surfaces produces an electric field, which in turn generates $E \times B$ flows in the plasma (hence the term zonal 'flow', although commonly the term is used to refer to the potential). The uniform structure of the electrostatic potential on a flux surface prohibits it from accessing free energy in equilibrium gradients, as advection of gradients requires a finite radial $E \times B$ flow $v_{E\times B,x} \propto \partial_y \Phi$ ($\propto n\Phi = 0$). Consequently, zonal flows do not result from linear instability physics, but are driven inherently via nonlinear dynamics. Linear instabilities (such as ITG) form from perturbations on an equilibrium, and the nonlinearity produces an inverse cascade that sends energy from these instabilities to large scales, fueling the zonal flow.

These flows can play a key role in the suppression of transport and the regulation of turbulence, either via the shearing of turbulent eddies (Biglari et al., 1990; Burrell, 1997; Terry, 2000) or the catalyzation of energy transfer out of unstable modes and into stable modes(Hatch et al., 2012; Makwana et al., 2014). For this reason, they are of central importance in ongoing research both in theoretical and experimental fields (see (Nishizawa et al., 2019)

---

[1] This section is only a very brief summary, refer to (Galperin and Read, 2019) for an in-depth review.

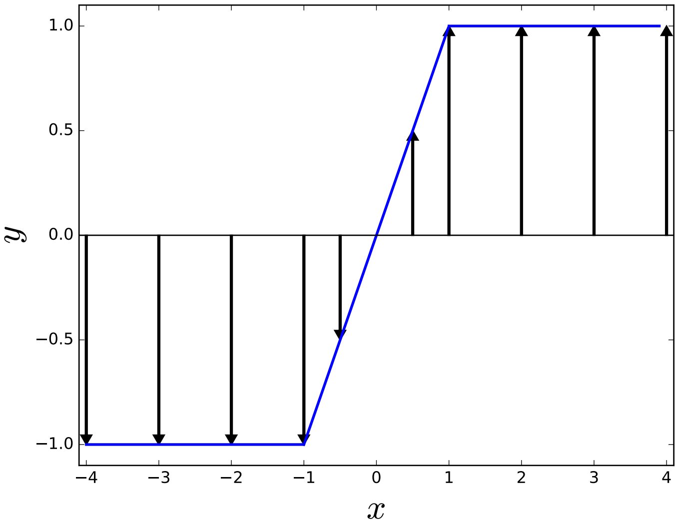

Figure 2.1: Example B_{y0} configuration for a slab magnetic equilibrium configuration unstable to tearing modes. The variation of B_{y0} occurs within the region of $x \in [-1, 1]$, called the resistive layer; non-ideal effects allow for finite B_x perturbations throughout this region.

for an example). The extent to which zonal flows regulate instability and turbulence varies significantly with the type of linear instability in question. Of the microinstabilities listed in Table 1.1, it is known that zonal flows have a substantial role in the turbulent dynamics of toroidal ITG (Dimits et al., 1996) and ∇n-TEM (Terry et al., 2002; Ernst et al., 2009). In contrast, ∇T-TEM and ETG turbulence (Jenko et al., 2000) do not rely on zonal flows for suppression. For instabilities that do depend on zonal flows for saturation, one would naturally expect that any mechanism by which these zonal structures are degraded would lead to an enhancement in turbulence.

Tearing Modes

Zonal flows can be eroded by the reconfiguration of magnetic field line topology arising from toroidally nested, closed flux surfaces. This phenomenon plays a central role in much of this thesis. Such reconfiguration of magnetic fields can be brought about by *tearing modes*, which are large-scale instabilities that occur in a number of plasma configurations, both in fusion devices (Hastie et al., 1977; Miller, 1989) and astrophysical contexts (Petschek, 1964; Walker et al., 2018) . How these tearing modes occur and result in a change in magnetic topology is briefly reviewed here; for more thorough discussions see (Furth et al., 1963; Biskamp, 2003).

Consider a slab magnetic field configuration in which the equilibrium magnetic field line component B_{y0} changes orientation very rapidly over a small spatial region, see Fig. 2.1. For ideal plasmas that have negligible resistivity, the magnetic field can be described using Eq. (1.13). Consider a resonant, normal mode perturbation of the form $\exp[ik_y y - i\omega t]$. *Resonant* refers to a perturbation for which $\mathbf{k} \cdot \mathbf{B} = 0$; in this case that occurs at $x = 0$ (referred to as the *resonant surface*). Inserting this perturbation into Eq. (1.13) gives the relation $\omega B_x = -k_y B_{y0} v_x$. This requires B_x to be zero at $x = 0$, where $B_{y0} = 0$. However, the addition of a resistive term into the MHD equations relaxes this requirement. When including the resistive term $(\eta/\mu_0)\nabla^2\mathbf{B}$ on the right-hand side of Eq. (1.13) and applying normal mode analysis, one arrives at

$$\omega B_x = -k_y B_{y0} v_x + \frac{i\eta}{\mu_0}\frac{\partial^2 B_x}{\partial x^2} \ , \tag{2.1}$$

assuming that $\nabla^2 \approx \partial_x^2$. This equation shows that the presence of resistivity (or more generally speaking, any non-ideal MHD effect) allows for finite B_x across the entire small spatial region over which B_{y0} varies; this subsequently allows for the connection of field lines across $x = 0$. When far removed from $x = 0$, the variation of the field line with x is considerably weaker and thus $\partial^2/\partial x^2 \to 0$, meaning that the region outside of the resistive layer can still be treated as ideal. In a thin region around $x = 0$ (referred to as the *resistive layer*), the resistivity becomes important. First posited in (Furth et al., 1963) as the 'constant-ψ approximation', B_x is assumed continuous across this resistive layer. B_y (a perturbation amplitude, distinct from B_{y0}), in contrast, has a discontinuity at $x = 0$ due to a surface current density over a very narrow layer in x (as can be seen from integrating Ampére's Law over the thin layer in x). From the divergence-free condition on magnetic fields:

$$\nabla \cdot \mathbf{B} = \partial_x B_x + ik_y B_y = 0 \ , \tag{2.2}$$

it is evident that the derivative of B_x also has a discontinuity across the current layer. This discontinuity is an important quantity for characterizing tearing modes called the *tearing stability index*, defined as

$$\Delta' \equiv \frac{1}{B_x}\left(\left.\frac{\partial B_x}{\partial x}\right|_{x=0+} - \left.\frac{\partial B_x}{\partial x}\right|_{x=0-}\right) \ . \tag{2.3}$$

This quantity is completely determined by magnetic field geometry outside of the resistive layer. For positive values of Δ', the tearing mode is unstable (Furth et al., 1963). Equation

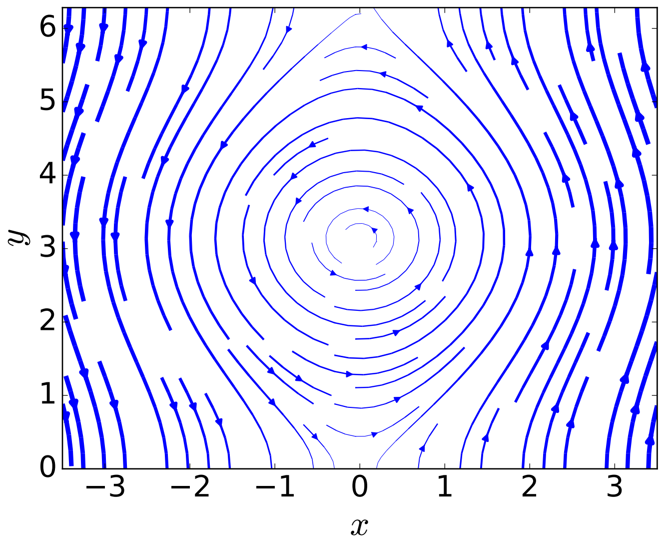

Figure 2.2: Field lines produced from sample tearing configuration given by $B_y = x$, $B_x = \sin y$. The resultant island is characterized by the O-point at $y = \pi$ and X-points at $y = 0, 2\pi$.

(2.1) can be solved to determine the instability growth rate γ, assuming that $B_{y0} \approx B_y' x$ within the layer, with B_y' constant. The details of the calculation can be found in (Goldston and Rutherford, 1995), and are not directly relevant to the discussion here. Given the normal mode description of $B_x = |B_x| e^{\gamma t} \sin{(k_y y)}$ (choosing the phase such that the complex exponential is precisely a sine wave for convenience) and the assumed form of $B_y \approx B_y' x$, the shape of the field lines can be calculated by solving the standard equation for field lines $dx/dy = B_x/B_y$. Fig. 2.2 shows a sample field configuration for the specified B_x and B_y.

From the figure, it is clear that the original topology of the magnetic field lines has been disrupted by the B_x of the tearing instability, and a *magnetic island* has formed[2]. The island can be characterized by the O-point, the y coordinate at which the island is at its widest, and the X-point, which corresponds to y coordinate at which the island field lines terminate. The outermost island field line that separates the island from the rest of the plasma is called the *separatrix*. Magnetic islands are of particular relevance to fusion plasmas; one can picture schematically that the x direction in the above figure corresponds to a radial coordinate in a fusion device and the y coordinate to a poloidal one. Particles can stream very quickly along field lines, or, referring to Fig. 2.2, particles move quickly along the direction the vector

---

[2] While tearing modes feature prominently through this thesis, islands can also be formed via external magnetic fields, see Chapter 4.

field points. For this reason, particles within islands can traverse the island very rapidly. In certain cases, the traversing particle can be lost from the island (either via collisions or other mechanisms), meaning that islands can greatly increase transport. Additionally, if multiple islands exist in close radial proximity, they can overlap, which produces a significant stochasticization of the magnetic field lines and loss of flux surfaces, which further increases transport losses (Rechester and Rosenbluth, 1978). This capacity for radial wandering due to islands plays a significant role in zonal flow erosion.

Magnetic-Flutter-Induced Zonal-Flow Erosion

Equipped with the concepts of zonal flows and tearing modes, one can now examine how these two interact. This section is a brief summary of the detailed theory presented in (Terry et al., 2013). Consider a zonal flow on a flux surface inside a toroidal confinement device, after the point at which any transient oscillations in amplitude (such as GAMS, (Winsor et al., 1968) for example) have decayed away. The electrostatic potential Φ, whose gradient generates $E \times B$ flows, is constant on a well-defined flux surface. The introduction of a resonant radial magnetic field (e.g. through a tearing mode) serves to break the well-defined flux surface, as previously discussed. Particles[3] following these field lines begin to wander radially (referred to as *magnetic flutter*) off of their original flux surfaces, to the effect that the electrostatic potential differences between flux surfaces (and subsequently the $E \times B$ flow) are reduced. Analytic theory predicts the short-time behavior of this reduction in Φ via the following equation from (Terry et al., 2013):

$$\Phi(t) \approx \Phi_{\mathrm{R}} - S_{\alpha}^{2} t^{2} \ , \tag{2.4}$$

where Φ_{R} is the residual value of the zonal flow at the point that the radial magnetic field is introduced, and S_{α}^{2} characterizes an electron source term. Note that the decrease in zonal flow is not exponential in time but quadratic, which matches well with simulations (Pueschel et al., 2013c,b).

This effect requires the loss of particles from one flux surface to another; for well-defined islands (as depicted in Fig. 2.2), streaming particles will on average remain on their original flux surface. Thus, this effect requires either 1) a stochasticization of the magnetic field lines through island overlap, or 2) a decorrelation of the radial magnetic field line upon

---

[3] This phenomenological picture concerns only electrons, as they stream along field lines much faster than ions for comparable temperatures

which a particle travels (see (Pueschel et al., 2013b) for details). As will be demonstrated throughout this thesis, this erosion of zonal flow activity due to large-scale radial magnetic field fluctuations can play a significant role in determining transport at small scales, as zonal flows are rendered less capable of suppressing microturbulence.

2.2 Gyrokinetic Theory

Results presented in this thesis come primarily from simulations performed within the framework of gyrokinetics, the salient features of which are summarized in this section. There is a large body of existing work that provides a much more in-depth discussion than what will follow; cf. (Littlejohn, 1981; Hahm, 1988; Brizard and Hahm, 2007).

The Gyrokinetic Equations

There are two primary approaches to theoretical modeling in plasma physics. One path is to model the plasma as a fluid, solving governing equations like those of MHD to determine quantities like plasma flow and magnetic field as a function of spatial variables (discussed briefly in Chapter 1). The other approach is kinetic in nature, in which one, for instance, solves a Boltzmann-like equation for a distribution function F that depends on three spatial variables and three velocity space variables. The latter approach provides information about individual particle effects that are not accounted for in a fluid framework, but is also much more expensive from the standpoint of computational resources. In the regime of strong guide magnetic fields (common in fusion contexts), the kinetic approach becomes especially expensive when attempting to resolve both the fast gyromotion timescales and the slower turbulence and transport timescales. To mitigate this expense, the gyrophase velocity coordinate can be removed via an averaging procedure; this approximation of kinetic theory is called *gyrokinetics*

A brief sketch of the derivation of the gyrokinetic equation is presented here, see the above references for more details. One begins with the governing equation for the full distribution function F_j for species j:

$$\partial_t F_j + \mathbf{v} \cdot \nabla F_j + \mathbf{a} \cdot \nabla_{\mathbf{v}} F_j = \mathcal{C}[F_j] \ , \tag{2.5}$$

where $\mathbf{v}$ is particle velocity, $\mathbf{a} = (q_j/m_j)(\mathbf{E} + \mathbf{v} \times \mathbf{B})$ is the acceleration due to electric ($\mathbf{E}$) and magnetic ($\mathbf{B}$) fields, and $\mathcal{C}[F_j]$ is a collision operator. The accelerating fields are determined from Maxwell's Equations (expressed here in cgs units, ignoring displacement current):

$$\nabla \cdot \mathbf{E} = 4\pi\rho \qquad\qquad \nabla \cdot \mathbf{B} = 0 \tag{2.6}$$

$$\nabla \times \mathbf{B} = \frac{4\pi}{c}\mathbf{J} \qquad\qquad \nabla \times \mathbf{E} = -\frac{1}{c}\frac{\partial \mathbf{B}}{\partial t} \ . \tag{2.7}$$

The plasma charge density ρ and current density $\mathbf{J}$ can be evaluated via the zeroth and first order moments of the distribution F_j, respectively, producing a closed system of equations.

The variables on which Eq. (2.5) depends correspond to the coordinates of a particle trajectory (x, y, z, v_x, v_y, v_z). As mentioned above, gyrokinetics averages over the gyrophase velocity space variable. To do so, it is useful first to transform from particle coordinates into *guiding center coordinates*, where the guiding center motion corresponds to the component of particle motion independent of its gyration around a field line, as discussed in Chapter 1. Written explicitly, transforming from the particle trajectory coordinates $\mathbf{x}$ to the guiding center coordinates $\mathbf{X}$ for species j occurs via:

$$\mathbf{x_j} = \mathbf{X_j} + \boldsymbol{\rho_j} \ , \tag{2.8}$$

where $\boldsymbol{\rho}_j \equiv \rho_j \cos\theta\,\hat{\mathbf{x}} + \rho_j \sin\theta\,\hat{\mathbf{y}}$ is the gyroradius vector of species j at the gyrophase θ, and the gyroradius of species j is given by $\rho_j \equiv v_\perp/|\omega_{jc}|$. The guiding center is expressed using field-aligned coordinates, such that the Z direction is parallel to the strong background magnetic field, X is a flux-surface (radial-like) coordinate, and Y coordinate (sometimes referred to as the binormal, but is not necessary orthogonal to Z) labels field lines on a flux surface; for more details on field-aligned coordinate systems, see (D'Haeseleer et al., 1991).

For velocity space, the transformation $(v_x, v_y, v_z) \to (v_\parallel, \mu, \theta)$ is made, where $v_\parallel = v_z$ is the velocity along the magnetic field B_0, $\mu = m_j(v_x^2 + v_y^2)/2B_0$ is the magnetic moment, and θ is the gyrophase angle. It is this gyrophase dependence that can be removed by averaging if the magnetic guide field is sufficiently strong that the gyrofrequency ω_c is much larger than frequencies of interest for turbulence ω, as is standard for fusion plasmas (e.g., a hydrogen ion in a 1 Tesla magnetic field has $\omega_\mathrm{c} \approx 100$ MHz, while microturbulence frequencies of interest in this work are on the order of $\omega \sim 100$ kHz). The process of gyroaveraging the kinetic equation can employ varying approaches (refer to (Littlejohn, 1981) or (Frieman and Chen, 1982) for details), and is not reproduced here. Taking the gyrokinetic equation for the gyrocenter distribution function $F_j(\mathbf{X}, v_\parallel, \mu)$, including particle drifts, from (Dannert, 2005):

$$\partial_t F_j + \left(v_\parallel \mathbf{b} + \frac{B_0}{B_{0\parallel}^*} \left(\mathbf{v}_{E\times B} + \mathbf{v}_{\nabla B_0} + \mathbf{v}_\mathrm{c} \right) \right) \cdot \left(\nabla F_j + \frac{1}{m_j v_\parallel} \left(q_j \bar{\mathbf{E}} - \mu \nabla \left(B_0 + \bar{B}_\parallel \right) \right) \right) = \bar{\mathcal{C}}[F_j] \ , \quad (2.9)$$

where overbars represent gyroaveraged quantities, $B_{0\parallel}^* = \mathbf{b} \cdot (\nabla \times (\mathbf{A}_0 + (m_j c)/(q_j) v_\parallel \mathbf{b}))$, with $\mathbf{b}$ the unit vector along the magnetic field, and $\mathbf{v}_{E\times B}, \mathbf{v}_{\nabla B_0}$, and $\mathbf{v}_\mathrm{c}$ correspond to $E \times B$, ∇-B, and curvature drifts as defined in Chapter 1, respectively.

Equation (2.9), coupled with the gyroaveraged Maxwell's Equations, provides a complete gyrokinetic description. However, further simplifications and manipulations are performed on this equation to arrive at the form that is used in this thesis. Importantly, the full gyrokinetic distribution function F_j is not directly calculated. Instead, it is expanded as $F_j = F_{0j} + f_j$, where F_{0j} refers to an equilibrium Maxwellian distribution function and f_j is the perturbed distribution function. This expansion derives from the assumption that $f_j/F_{0j} \sim \rho_\mathrm{ref}/L_\mathrm{ref} \equiv \delta \ll 1$ (referred to often as a "δf" approach). This form of F_j can be inserted into Eq. (2.9), which can then be separated by orders in δ. The $\mathcal{O}(\delta)$ equation is expressed as follows:

$$\partial_t g_j + \frac{B_0}{B_{0\parallel}^*} \left(\mathbf{v}_{E\times B} + \mathbf{v}_{\nabla B_0} + \mathbf{v}_\mathrm{c} \right) \cdot \left(\nabla F_{0j} - \frac{\mu}{m_j v_\parallel} \frac{\partial F_{0j}}{\partial v_\parallel} \nabla B_0 \right) + v_\parallel \mathbf{b} \cdot \mathbf{\Gamma}_j + \frac{B_0}{B_{0\parallel}^*} \left(\mathbf{v}_{E\times B} + \mathbf{v}_{\nabla B_0} + \mathbf{v}_\mathrm{c} \right) \cdot \mathbf{\Gamma}_j - \frac{\mu}{m_j} \mathbf{b} \cdot \nabla B_0 \frac{\partial f_j}{\partial v_\parallel} = \bar{\mathcal{C}}[f_j] \ , \quad (2.10)$$

where the following definitions are applied:

$$g_j = f_j - \frac{q_j}{m_j c} \frac{\partial F_{0j}}{\partial v_\parallel} \bar{A}_\parallel \quad (2.11)$$

$$\mathbf{\Gamma}_j = \nabla g_j - \frac{q_j}{m_j v_\parallel} \frac{\partial F_{0j}}{\partial v_\parallel} \nabla \chi_j + \frac{q_j}{m_j c} \bar{A}_\parallel \nabla \frac{\partial F_{0j}}{\partial v_\parallel} \quad (2.12)$$

$$\chi_j = \bar{\Phi} - \frac{v_\parallel}{c} \bar{A}_\parallel + \frac{\mu}{q_j} \bar{B}_\parallel \ . \quad (2.13)$$

It should be noted that Eq. (2.10) does contain one term that is $\mathcal{O}(\delta^2)$, the $E \times B$ nonlinearity. The electric and magnetic fields have been expressed in terms of the electrostatic and electromagnetic potentials, which are combined into the generalized potential χ_j. The remaining tasks in bringing Eq. (2.10) to its final form involve: 1) inserting the explicit form of the Maxwellian F_{0j}, from which the equilibrium gradient drive terms arise, 2) expanding the vector expressions, 3) suitably normalizing the equation, and 4) taking the Fourier transform. The details of these steps are carried out in (Merz, 2008) but do not elucidate any additional physics; as such, the final form of the gyrokinetic equation for g_j as used in this thesis is presented here:

$$\begin{aligned}
\partial_t g_j = & \underbrace{-\left(\omega_n + \left(v_\parallel^2 + \mu B_0 - \frac{3}{2}\right)\omega_{Tj}\right) F_{0j} i k_y \chi_j}_{\text{Linear Drive}} + \underbrace{\frac{\beta T_{0j}}{q_j B_0^2} v_\parallel^2 \omega_p \Gamma_{jy}}_{\text{Pressure Effects}} \\
& - \underbrace{\frac{v_{Tj}}{J B_0} v_\parallel \Gamma_{jz}}_{\text{Parallel Dynamics}} \underbrace{- \frac{T_{0j}\left(2v_\parallel^2 + \mu B_0\right)}{q_j B_0}\left(K_y \Gamma_{jy} + K_x \Gamma_{jx}\right)}_{\text{Curvature Effects}} \\
& + \underbrace{\frac{v_{Tj}}{2 J B_0} \mu \partial_z B_0 \frac{\partial f_j}{\partial v_\parallel}}_{\text{Particle Trapping}} + \underbrace{\sum_{\mathbf{k}'_\perp}\left(k'_x k_y - k_x k'_y\right)\chi(\mathbf{k}'_\perp) g(\mathbf{k}_\perp - \mathbf{k}'_\perp)}_{E\times B\ \text{Nonlinearity}} + \underbrace{\bar{\mathcal{C}}[f_j]}_{\text{Collisions}} \quad . \qquad (2.14)
\end{aligned}$$

The quantities $\omega_{n,Tj,p}$ correspond to the normalized density, temperature, and pressure gradients of species j, curvature terms K_x and K_y include details of the magnetic geometry, J is the Jacobian that arises from expansion of the vector quantities, and β is the ratio of electron kinetic pressure to magnetic pressure. The physical interpretation for each term is provided in the underbraces. Of special note is the nonlinearity, which is a convolution under Fourier transform and results in the coupling of distinct spatial scales and consequent turbulent dynamics. To model linear instability, this term can be removed and the resulting linear equation $\partial_t g_j = \mathcal{L}_j g_j$ solved.

The electric and magnetic fields are expressed in terms of gyroaveraged electrostatic and electromagnetic potentials, which are evaluated from moments of the perturbed distribution function given (in the limit of $B_\parallel = 0$) below:

$$\Phi = \frac{\sum_j n_{0j}\pi q_j B_0 \int J_0(\lambda_j) g_j dv_\parallel d\mu}{k_\perp^2 \lambda_D^2 + \sum_j \frac{q_j^2}{T_{0j}} n_{0j}(1-\Gamma_0(b_j))} \tag{2.15}$$

$$A_\parallel = \frac{\sum_j \frac{\beta}{2} q_j n_{j0} v_{Tj} \pi B_0 \int v_\parallel J_0(\lambda_j) g_j dv_\parallel d\mu}{k_\perp^2 + \sum_j \frac{\beta q_j^2}{m_j} n_{0j} \pi B_0 \int v_\parallel^2 J_0^2(\lambda_j) F_{0j} dv_\parallel d\mu}\ , \tag{2.16}$$

where $J(\lambda_j)$ is the Bessel function of argument $\lambda_j = k_\perp \rho_j$ that arises from gyroaveraging sinuosoidally fluctuating fields, and $\Gamma_0(b_j) = I_j(b_j)e^{-b_j}$ where I_j is a modified Bessel function of argument $b_j = v_{Tj}^2 k_\perp^2 / 2\omega_{cj}^2$. For finite $B_\parallel$, the potentials Φ and $B_\parallel$ form a coupled system of equations that can be solved at additional computational expense; $A_\parallel$ remains decoupled provided the spatial scales of interest obey $k_\parallel \ll k_\perp$. Equations (2.14),(2.15), and (2.16) are the governing equations used throughout this thesis.

The GENE Code

The subsequent chapters of this thesis solve these governing equations using the gyrokinetics code Gene, originally published in (Jenko et al., 2000); for thorough documentation refer to www.genecode.org. Gene is an Eulerian code that solves the gyrokinetic equation on a 5+1-dimensional (x,y,z,$v_\parallel$,μ,t) space for the non-adiabatic part of the perturbed distribution function g_j defined in Eq. (2.11), where j can correspond to electron, majority ion, or impurity ion species. The code can be operated either in the global (radially global or full-flux-surface) or local limit; within this thesis all results are calculated in the local limit, referred to as 'flux-tube' calculations (Beer, 1995). As concepts that arise from utilizing this flux-tube limit appear throughout this thesis, it shall be discussed briefly here.

For flux-tube simulations, the domain of calculation is limited to both a radially- and binormally-localized (corresponding to x and y directions, respectively) slice of the full system being simulated. Generally speaking, the extent of the domain in each direction is on the order of 10s−100s of gyroradii. Periodicity is assumed for both the x and y directions, and thus a physical interpretation of the radial extent of structures seen in flux-tube simulations only applies to a small region near the field line around which the simulation domain is centered. Within these localized radial simulation boxes, the flux-tube approximation assumes that both equilibrium quantities and their gradients are constant over the x-extent of the domain. Additionally, the assumption of radial periodicity requires the size of turbulent structures to be smaller than the x-box length to avoid nonphysical self-connections. Provided sufficient convergence checks in box sizes and resolutions are performed, the assumption of periodicity allows for a reliable description of turbulence within a small radial domain in Fourier space. As such, flux-tube Gene simulations are spectral in x and y, while evaluating the z dimension in real space using finite-difference methods.

The z direction corresponds to the field-line-following (poloidal-like) angle, and for axisymmetric (toroidally symmetric) simulations covers the extent of a single poloidal turn $[-\pi, \pi]$ (where $z = 0$ corresponds to outboard midplane, $z = \pm\pi$ to the inboard). This coordinate is quasi-periodic for toroidal devices; generally speaking, field lines will not close after a single poloidal transit. In other words, though the field line returns to the same poloidal point after traversing from $-\pi$ to π, it will not be at the same toroidal point; this is a consequence of the helical structure of the fields. Enforcing quasi-periodicity in z produces an additional constraint, referred to as the *parallel boundary condition* (Merz, 2008) for a function F:

$$F(k_x, k_y, \pi) = (-1)^{nN} F(k_{x,\min}(m + nN), k_y, -\pi) \ , \tag{2.17}$$

where m,n, and N are integers such that $k_x = mk_{x,\min}$, $k_y = nk_{y,\min}$, and $N = 2\pi\hat{s}k_{y,\min}/k_{x,\min}$, with the normalized magnetic shear defined as $\hat{s} = (r/q)(dq/dr)$. An important consequence of Eq. (2.17) is the coupling of modes at different k_x. Whereas linear simulations otherwise do not allow any interactions between different Fourier modes, the presence of magnetic shear serves to connect every (nN)-th k_x mode at a given k_y through this parallel boundary condition. This must be taken into account when analyzing linear mode structures to ensure that appropriate resolutions are used to capture these connections.

Concerning the use of appropriate resolutions for gyrokinetic simulations, convergence checks are performed in all results presented in this thesis. For linear convergence checks, resolutions in $x, y, z, v_\parallel$, and μ are doubled independently until the calculated linear growth rate varies by less than 5%. For nonlinear simulations, convergence is verified through the examination of flux spectra, mode structures, and transport amplitudes. To be considered converged, the peak in flux spectra should not occur at the smallest k_y, and the tail of both the k_x and k_y spectra should fall off to less than 10% of the peak flux value. For mode structures, the time-averaged z-structure is examined to ensure that it is sufficiently smooth. Moreover, the calculated amplitude of heat and particle fluxes must vary less than 20% upon the doubling of $k_{x,\min/\max}$ and $k_{y,\min/\max}$ to be considered satisfactorily converged. The resolutions quoted in all results hereafter arise from these convergence methods.

Gene has a variety of options by which collisions can be modeled, including (but not limited to) collisionless, Krook-like, and Lorentz (stationary ions) collisions. All collisional simulations reported in this thesis utilize a full Landau-Boltzmann collision operator for both electron and majority ion species. Time dependence in Gene can be evaluated in two primary approaches: initial value and eigenvalue solutions. For linear simulations, instabilities can be characterized either via time evolution of a seeded initial condition, or via inversion of the linear matrix to calculate the eigenvalues (with certain additional packages (Hernandez et al., 2005), fast iterative approaches can find maximal eigenvalues without matrix inversion). While initial value simulations are the primary method utilized in this thesis, the eigenvalue solver is employed at various times to describe relevant subdominant modes. Nonlinear simulations require the initial value calculation approach.

2.3 Chapter Summary

Topics in plasma physics relevant to the core themes explored in the rest of the thesis were discussed in this chapter. Zonal flows were introduced as an important mechanism for microturbulence suppression and regulation. These flows can be reduced by the introduction of radial magnetic field perturbations, which in fusion devices such as the RFP are often produced by tearing modes or Resonant Magnetic Perturbations. It is by this magnetic-flutter-induced reduction of zonal flows that large- scale magnetic fluctuations can affect microturbulence, as will be demonstrated in later chapters. The gyrokinetic framework was discussed, including the governing equations that are solved using the Gene code. With this foundation, the following Chapters explore the interaction of tearing modes, microturbulence, and zonal flows in a variety of plasma systems.

3 TRANSPORT, TURBULENCE, AND ZONAL FLOWS IN THE MADISON SYMMETRIC TORUS REVERSED-FIELD PINCH

Having established the motivation and needed theoretical groundwork, the core concept of multi-scale interactions between magnetic fluctuations, microturbulence, and zonal flows is examined in the Reversed-Field Pinch (RFP). As mentioned in Chapter 1, the RFP is a toroidal fusion device characterized specifically by its unique magnetic geometry, which differs from the tokamak by having a significantly smaller toroidal field B_ϕ. This smaller B_ϕ results in $B_\theta \geq B_\phi$ for a large radial extent of the device, and a much lower safety factor q (defined in Eq. (1.8)) and larger normalized magnetic shear compared to the tokamak. In the core of the RFP, the safety factor is at its largest value, generally $q \approx 0.2$, which means RFP equilibria are subject to large-scale tearing modes (discussed in more detail in Chapter 2). These tearing modes lead to substantial transport and result in very short confinement times for standard RFP plasmas.

This deleterious effect of tearing modes on plasma confinement in the RFP can be mitigated to a significant degree by operating in a regime with current profile control using Pulsed Poloidal Current Drive (PPCD), originally demonstrated experimentally in (Sarff et al., 1994). In this regime, poloidal currents are induced in the edge of the plasma, which serve to flatten the current profile and consequently lower tearing mode drive. PPCD plasmas thus exhibit much lower stochastic transport losses, as well as confinement times comparable to tokamaks (Chapman et al., 2010). A result of this improved confinement is an increase in core pressure values, and a resultant increase in temperature and density gradients towards the edge. As seen experimentally in (Duff et al., 2018), these increased gradients can drive microturbulence. Additionally, work detailed in (Nishizawa et al., 2019) demonstrates the presence of zonal flows in PPCD plasma via direct experimental measurements, which can play a role in instability saturation.

This chapter demonstrates a link between the microturbulence and zonal flows observed in MST, centering around microturbulence and transport driven by the enhanced gradients in PPCD, as well addressing the role that suppressed tearing modes have on the transport via interactions with zonal flows. Per the mechanism described in Chapter 2, it is seen here that zonal flows are degraded by radial magnetic perturbations introduced by tearing mode fluctuations. Two different discharges are examined, one dominantly ∇n-TEM unstable and the other ITG unstable. Specifically, this chapter discusses how the turbulence generated by each differs in response to zonal flow erosion. The behavior of these two discharges in the complete absence of tearing mode fluctuations is also presented, revealing properties of strong zonal flow formation in the RFP.

3.1 Microturbulent Fluctuations in MST

Prior gyrokinetic modeling of MST microinstability properties, detailed in (Carmody et al., 2015), focused on two different PPCD discharges, with different values of the toroidal current induced in the plasma. That work examined discharges with toroidal plasma currents of 200 and 500 kA, which exhibited dominant instabilities of ITG and density-gradient-driven TEM, respectively. Recent work of (Duff et al., 2018) using an updated FIR system has produced measurements for new 200 kA PPCD discharges of deuterium plasmas. The FIR diagnostic was used to measure density fluctuations during PPCD discharges, shown in Fig. 3.1. The measurements show that as the induced poloidal current grows in PPCD (beginning at 10 ms), the large-scale tearing mode amplitudes decay until reaching some small, quasi-stationary value around 18 ms. In the PPCD 'flat top', where tearing modes are maximally (but not fully) suppressed, a steepening of the density gradient is observed, accompanied by higher-frequency density fluctuations. This steepening of the density profile occurs primarily outside the reversal surface (the flux surface where $B_\phi = 0$ and thus $q = 0$, $r/a \approx 0.7$ for these discharges). Inside the reversal surface, the density profile remains relatively flat. Consequently, the high-frequency density fluctuations are observed almost entirely in this outer region.

Experimental scans show a strong dependence of these fluctuations on the density gradient, with a critical gradient $R_0/L_n \approx 18$ (see Fig. 3.2), where R_0 is the major radius on axis ($R = R_0 + r\cos\theta$, where θ is the poloidal angle), $L_n^{-1} \equiv -(1/n_0)dn_0/dr$ is the equilibrium density gradient scale length, and n_0 is the background electron density. The fluctuations are observed to propagate in the electron diamagnetic direction in the perpendicular wavenumber range $k_\perp \rho_\mathrm{s} \lesssim 0.2$. Measurements of carbon impurity density fluctuations in PPCD using ion Doppler spectroscopy (IDS), performed in parallel with FIR, also observed fluctuations in the $50 - 100$ kHz frequency range outside the reversal surface (Nishizawa et al., 2016), providing evidence that the fluctuations are due to TEM turbulence. These experimental findings motivate the work discussed in the rest of this chapter.

To understand the underlying nature of these fluctuations, gyrokinetic simulations based on the experimental profile data from the new 200 kA PPCD discharges discussed above are

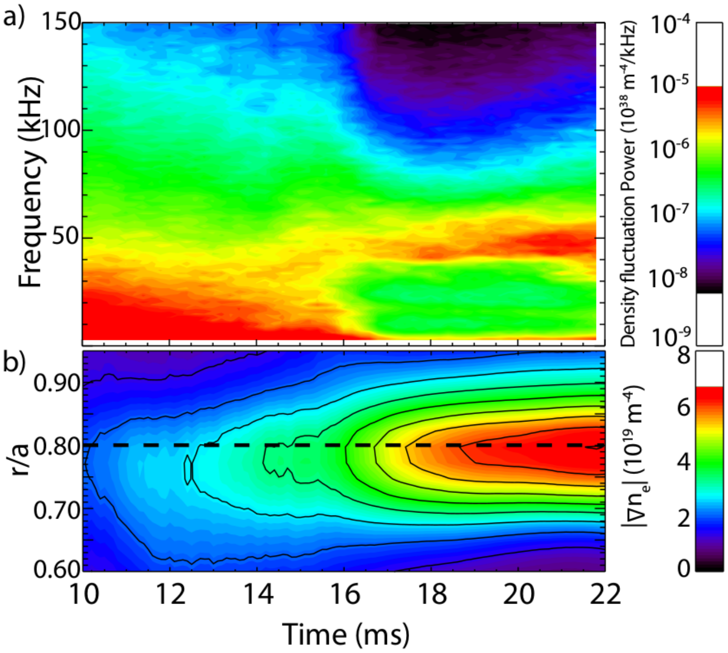

Figure 3.1: Time evolution of (a) density fluctuation spectra at $r/a = 0.8$ and (b) density gradient as a function of radius. At the beginning of PPCD, tearing mode fluctuations dominate the spectrum at low frequency, and are gradually reduced until the PPCD 'flat top' which occurs at $t \approx 18$ ms. This decrease in tearing activity produces an increase in density gradient as shown in (b), which drives microturbulence that produces the higher-frequency fluctuations shown in (a). Taken from (Duff et al., 2018).

.

performed at four different radial locations in the range $0.55 < r/a < 0.85$, focusing primarily outside of the reversal surface (located at $r/a \approx 0.7$) where the high-frequency density fluctuations were observed. As mentioned previously, all simulation results presented are local flux-tube calculations performed using the GENE code, with RFP-specific equilibrium modifications implemented via the Adjusted Circular Model (ACM) in (Carmody et al., 2015). The latter expands upon the standard Circular model of circular concentric flux surfaces of (Lapillonne et al., 2009) to account for the magnetic field variation with minor radius intrinsic to the RFP.

Nominal resolutions for these simulations were 16 grid points in the direction parallel to the magnetic guide field (z), 32 parallel velocity ($v_\parallel$) grid points, and 8 magnetic moment (μ) grid points; linear simulations required 15 k_x modes (where k_x refers to the radial wavenumber). Profiles used as input for the code were obtained from an MSTFit equilibrium reconstruction

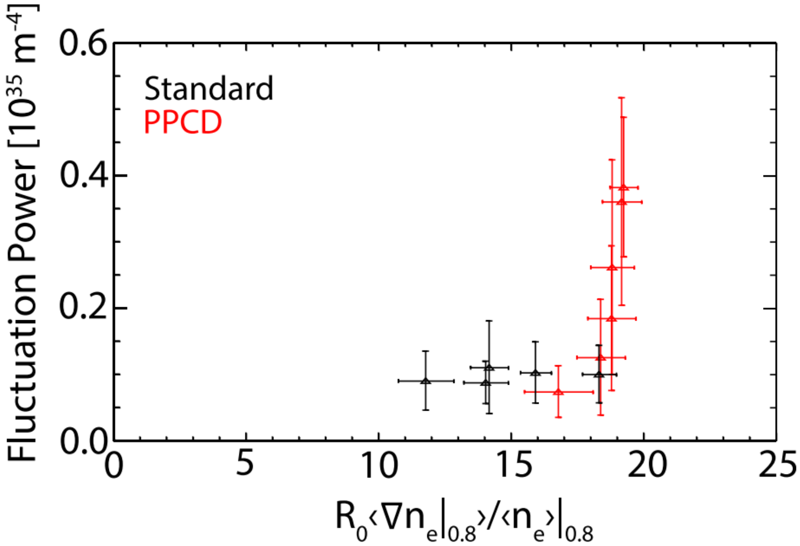

Figure 3.2: Density fluctuation power as a function of normalized density gradient for standard and PPCD plasmas. The improved-confinement PPCD regime exhibits a critical gradient of $R/L_n \approx 18$. Taken from (Duff et al., 2018).

(Anderson et al., 2004). Specific input parameters used in this chapter for two distinct PPCD discharges (labeled by their respective dominant linear instabilities, to be discussed) are listed in Table 3.1. As discussed in (Carmody et al., 2015), radial locations near the reversal surface are numerically more challenging, because the parameter $\hat{s} \equiv (r/q)dq/dr$, which represents shear in a tokamak, diverges at the $q = 0$ surface. In the RFP, the magnetic shear remains well-behaved throughout the plasma volume, and the physics of the simulations is unaffected by the behavior of $\hat{s}$ near $q = 0$. However, $\hat{s}$ is used in GENE for the flux-tube boundary conditions and as a metric for dq/dr. The microturbulent fluctuations detected in the experiment were localized sufficiently far from the reversal surface to support the assumption that exclusion of the region near the reversal surface in this chapter does not significantly alter its relevance.

During PPCD, the equilibrium profiles are mostly flat inside the reversal surface, and thus the plasma is stable to microinstability throughout almost the entire region. There is a strong linear destabilization outside the reversal surface ($r/a \gtrsim 0.7$). This radial localization of instability matches the FIR measurements, which detected high-frequency density fluctuations primarily outside the reversal surface. Such strong destabilization is attributed to the large background density and temperature gradients which form in that region during PPCD.

Instability	r/a	q	$\hat{s}$	β	ν_c	R_0/L_T	R_0/L_n
TEM	0.565	0.0528	-6.05	0.11	0.0029	9.67	4.79
	0.748	-0.0690	8.16	0.028	0.0088	23.6	23.0
	0.791	-0.103	6.18	0.014	0.013	28.9	28.5
	0.836	-0.141	5.00	0.0053	0.020	37.1	34.2
ITG	0.807	-0.1103	5.08	0.0063	0.27	30.0	19.1

Table 3.1: Physical parameters taken from MSTFit equilibrium reconstructions of two distinct 200 kA PPCD discharges, one dominated by ∇n-TEM instability and the other by ITG instability. For the TEM-dominated discharge, analyses were performed at four different radial locations; only one radial location was studied in the ITG-dominated discharge. These parameters are used as input for GENE simulations. $\nu_{\mathrm{c}} \equiv R_0/(4v_{T\mathrm{e}})\nu_{\mathrm{ei}}$, $R_0/L_T = R_0/L_{T\mathrm{e}} = R_0/L_{T\mathrm{i}}$ and $T_{\mathrm{i}0} = 0.4T_{\mathrm{e}0}$.

Precise data on ion temperature profiles $T_{\mathrm{i}0}(r)$ is lacking for these discharges, so it is assumed that $T_{\mathrm{i}0} \approx 0.4T_{\mathrm{e}0}$ at all radii, and the normalized temperature gradients of both species are the same; density gradients are equal for ions and electrons due to quasineutrality. A consequence of these assumptions is that $\eta_{\mathrm{i}} = \eta_{\mathrm{e}} = \eta$, where $\eta_j \equiv (d\ln T_{j0}/dr)/(d\ln n_{j0}/dr)$. For this discharge, $\eta \approx 1.0$ outside the reversal surface. A common empirical rule, developed in (Rewoldt and Tang, 1990) from tokamak gyrokinetic simulations, which has also been found to apply to the RFP (Carmody et al., 2015), states that $\eta \approx 1.3$ defines a boundary between ITG- and TEM-dominated regimes, with $\eta \lesssim 1.3$ being TEM-dominated.

As seen in Fig. 3.3, the dominant instability propagates, at toroidal wavenumbers $0.1 \lesssim k_y\rho_{\mathrm{s}} \lesssim 1$, in the electron diamagnetic direction (denoted by negative frequencies). The transition to positive frequencies at higher k_y is a feature of the so-called ubiquitous TEM, originally introduced in (Coppi and Pegoraro, 1977). Scans were performed separately for density, ion temperature, and electron temperature gradient at $k_y\rho_{\mathrm{s}} = 0.5$, where the linear growth rate peaks. Each quantity was scanned over a range of values while all other parameters were held fixed at their experimental values. As shown in Fig. 3.3, at experimental parameters the linear growth rate varies most strongly with density gradient, agreeing with the expectation of a density-gradient-driven trapped-electron mode. To provide further support of this assessment, the linear analysis was repeated, separating the contributions of trapped and passing particles. The cross phases are calculated separately for trapped and passing particles from the linear eigenmodes, where the cross phase α is defined for two fluctuation quantities A and B as $\langle AB\rangle = |A||B|\sin\alpha$. As seen in Fig. 3.4, the phase difference between electrostatic potential and electron density fluctuations is $\approx +\pi/2$, consistent with instability, while the corresponding passing-electron fluctuations are primarily in phase.

As a point of comparison with the TEM characterization, linear analysis was performed on another recent 200 kA PPCD discharge in which background temperature gradients are $\approx 50\%$ larger than background density gradients. The increased temperature gradients result in $\eta \approx 1.5$, characteristic of an ITG-dominated regime. As expected, the dominant instability in this case propagates in the ion diamagnetic direction at wavenumbers of $k_y \rho_\mathrm{s} \sim 0.1 - 1$. Figure 3.5 shows the instability being driven strongly by the ion temperature gradient, and stabilized by both electron temperature gradient and density gradient. These qualities are consistent with the ITG instability, as expected for $\eta > 1.3$. In what follows, the nonlinear behavior of these two instabilities in the RFP are compared.

3.2 Gyrokinetic Turbulence in PPCD

Turbulence and transport in PPCD discharges are modeled using nonlinear flux-tube simulations. The RFP has large magnetic shear, varying on the minor-radius scale, which can result in significant nonlinear simulation costs, as modes with very different radial scales (very different k_x) become coupled through the flux-tube parallel boundary condition. The highest-magnitude normalized shear value considered in the nonlinear simulations is $\hat{s} = 6.18$, for which numerical convergence requires a total of 192 (positive and negative) k_x Fourier modes when resolving the k_y spectrum with 12 modes. The perpendicular box has an extent of 16 ρ_s in the radial x direction, and 31.4 ρ_s in the y (toroidal-like) direction, which is sufficient to encompass turbulent structures and prevent self-connection. The following discussion focuses on results from nonlinear simulations at $r/a = 0.8$.

Nonlinear calculations based on the TEM-dominated discharge produce negligible transport, with the electrostatic heat diffusivity of order $\chi_\mathrm{e} \sim 10^{-4}$ m^2/s. This is a consequence of very strong zonal flows seen in Fig. 3.6(a) that are generated nonlinearly, which greatly reduce transport associated with the instability. The fact that this diffusivity is several orders of magnitude smaller than in the experiment suggests that there is physics present in the experiment that these simulations do not capture. Indeed, the simulations do not take into account background current gradients, which drive tearing modes primarily in the core of the RFP. Though reduced in PPCD, (Carmody et al., 2015) demonstrated that these tearing fluctuations play an important role in setting microturbulent transport levels. To self-consistently model the tearing mode effects, current gradients need to be included in

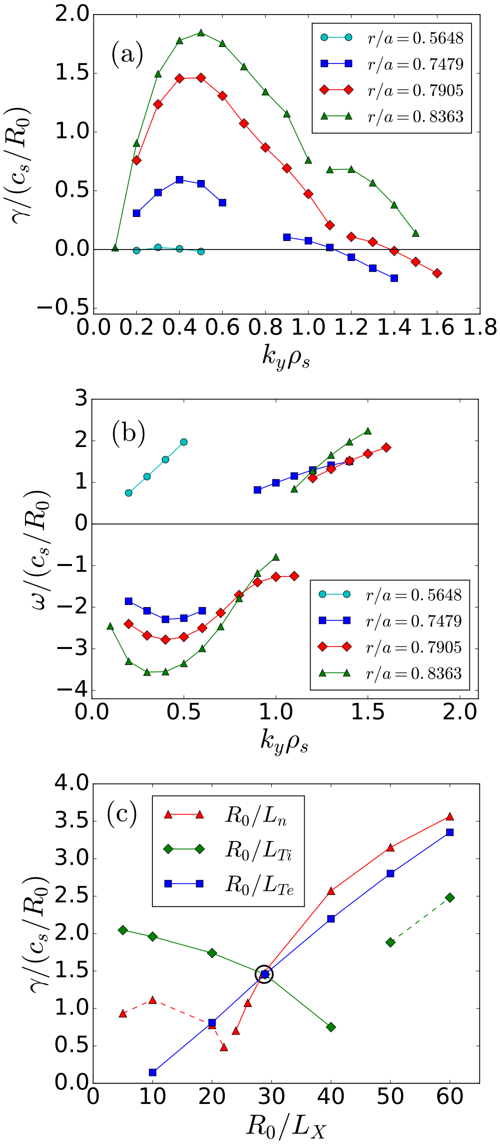

Figure 3.3: Linear instability analysis for the low-η, 200 kA PPCD discharge. In (a), growth rates are strongest in the $k_y \sim 0.1 - 1$ range. In (b), dominant frequencies show drifts in the electron diamagnetic direction, with positive-frequency branches arising from the ubiquitous TEM. In (c), gradient scans at $k_y\rho_s = 0.5$ and $r/a = 0.7905$ are shown, with experimental values circled. The three solid-line curves correspond to variation of the density gradient (triangles), ion temperature gradient (diamonds), and electron temperature gradient (squares), with other gradients held fixed. The density-gradient drive is the strongest for nominal parameters. Dashed lines correspond to a separate, ion-direction unstable mode branch.

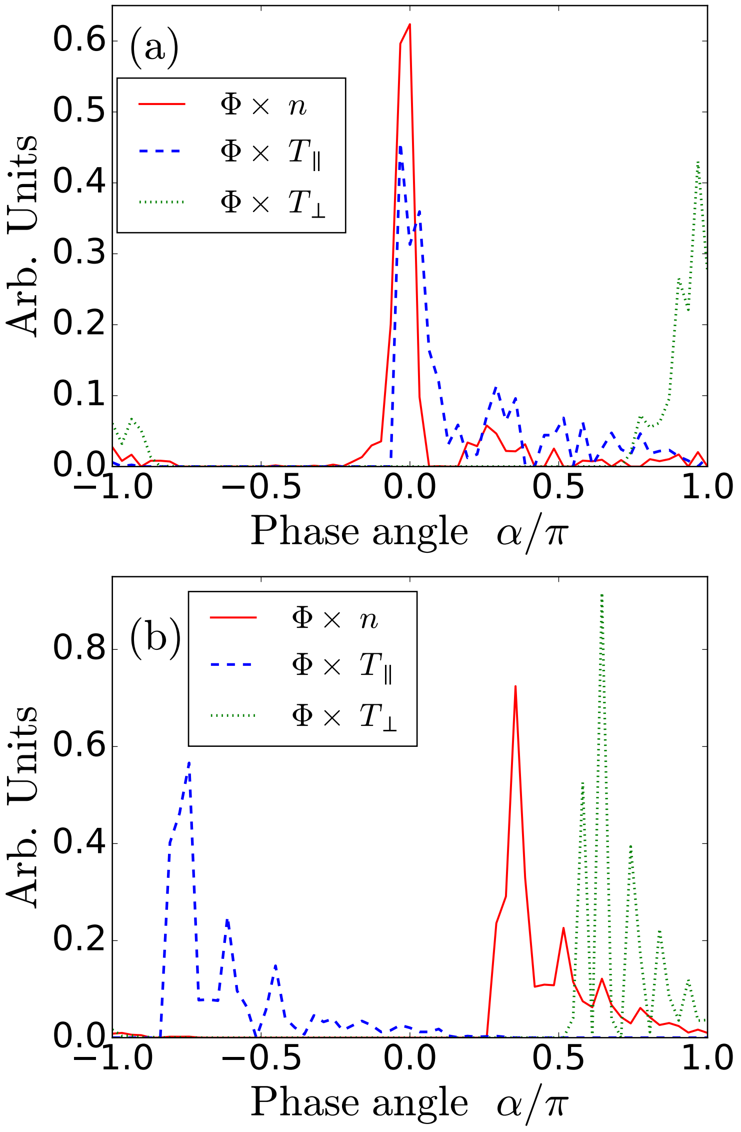

Figure 3.4: Cross phases constructed from fluctuating quantities (Φ, n, $T_\parallel$, and $T_\perp$) for passing electrons in (a) and trapped electrons in (b). The phase difference $\alpha \approx +\pi/2$ between Φ and n corresponds to a ∇n-driven instability, and only arises from the trapped-particle distribution.

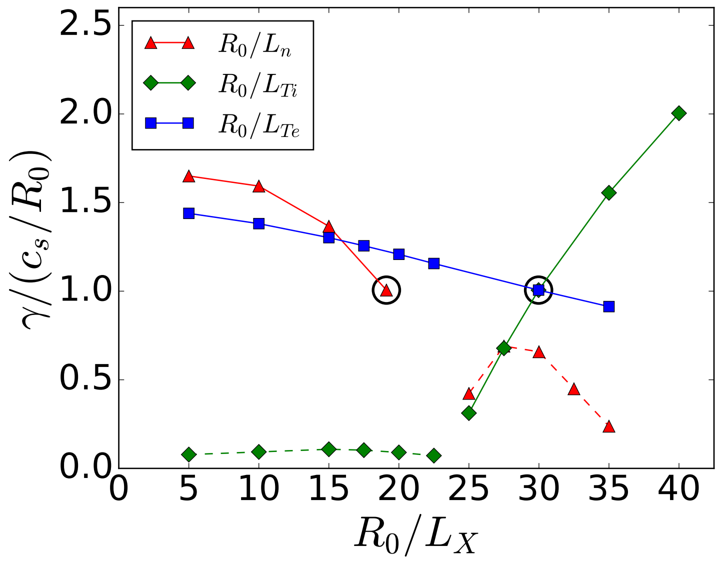

Figure 3.5: Gradient scans at $k_y\rho_\mathrm{s} = 0.5$ and $r/a = 0.807$ for the $\eta \approx 1.5$ PPCD discharge, with experimental values circled. The three solid-line curves correspond to variation of the density gradient (triangles), ion temperature gradient (diamonds), and electron temperature gradient (squares), with the respective other gradients held fixed. Consistent with ITG modes, the ion temperature gradient $R/L_{T\mathrm{i}}$ strongly destabilizes the mode, while the electron temperature and density gradients have a stabilizing effect. Dashed lines correspond to a separate, electron-direction mode branch, which is stable at the default experimental parameters.

a global simulation combining core and edge regions. In lieu of the challenging problem of using global simulations to model these residual tearing fluctuations, an ad-hoc tearing-parity, constant-in-time $A_\|$ perturbation is implemented in the code. For details on the perturbation, which has been modified from that used in (Carmody et al., 2015), see Appendix A.

The inclusion of this perturbation degrades the previously very strong zonal flows, visible in the electrostatic potential contours in Fig. 3.6(b). As discussed in Chapter 2, the radial magnetic field perturbation allows electron streaming along field lines to travel to different flux surfaces, effectively shorting out the electrostatic potential differences and thus eroding the zonal flows. The impact of this process can be described quantitatively by determining the difference in linear and nonlinear critical gradients, as shown in Fig. 3.7. This upshift in critical gradient when comparing the linear stability threshold with the nonlinear transport threshold is referred to as the *Dimits shift*, from (Dimits et al., 2000). While the case without tearing fluctuations experiences a factor of four upshift in critical density gradient, including

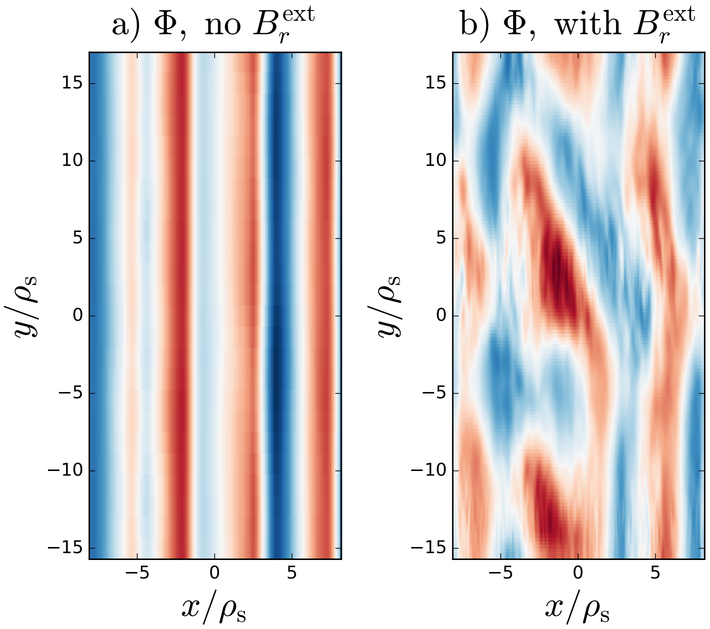

Figure 3.6: Electrostatic potential contours Φ (in units of $\rho_{\mathrm{s}}e/(R_0T_{\mathrm{e}0})$) in TEM turbulence for simulations with zero (a) and finite (b) residual magnetic tearing fluctuations. In the absence of magnetic activity associated with tearing modes, TEM instability leads to very strong zonal flow formation and the complete suppression of heat and particle transport.

the fluctuation removes the upshift almost entirely.

This zonal flow reduction results in increased transport. Setting the strength of the perturbation extrapolated from magnetic field measurements taken at the wall, the calculated heat diffusivity ($\chi_{\mathrm{e}} \approx 10$ m^2/s) comes to within 30% agreement with that expected from experimental data[1]. It is important to note that transport, both here and throughout this chapter, refers only to the electrostatic transport resulting from radial $E \times B$ flows. There is also magnetic flutter transport that increases with the tearing perturbation as one would expect, which is observed in simulations to be of the same order as electromagnetic transport for experimentally relevant parameters. The method by which the tearing fluctuations are accounted for is not self-consistent, thus conclusions concerning the physics of electromagnetic transport cannot be drawn from this chapter; as such, only transport through the electrostatic channel is examined.

It is interesting to note that while both the ITG- and TEM-dominated discharges generate

---

[1] from private communication with James Duff

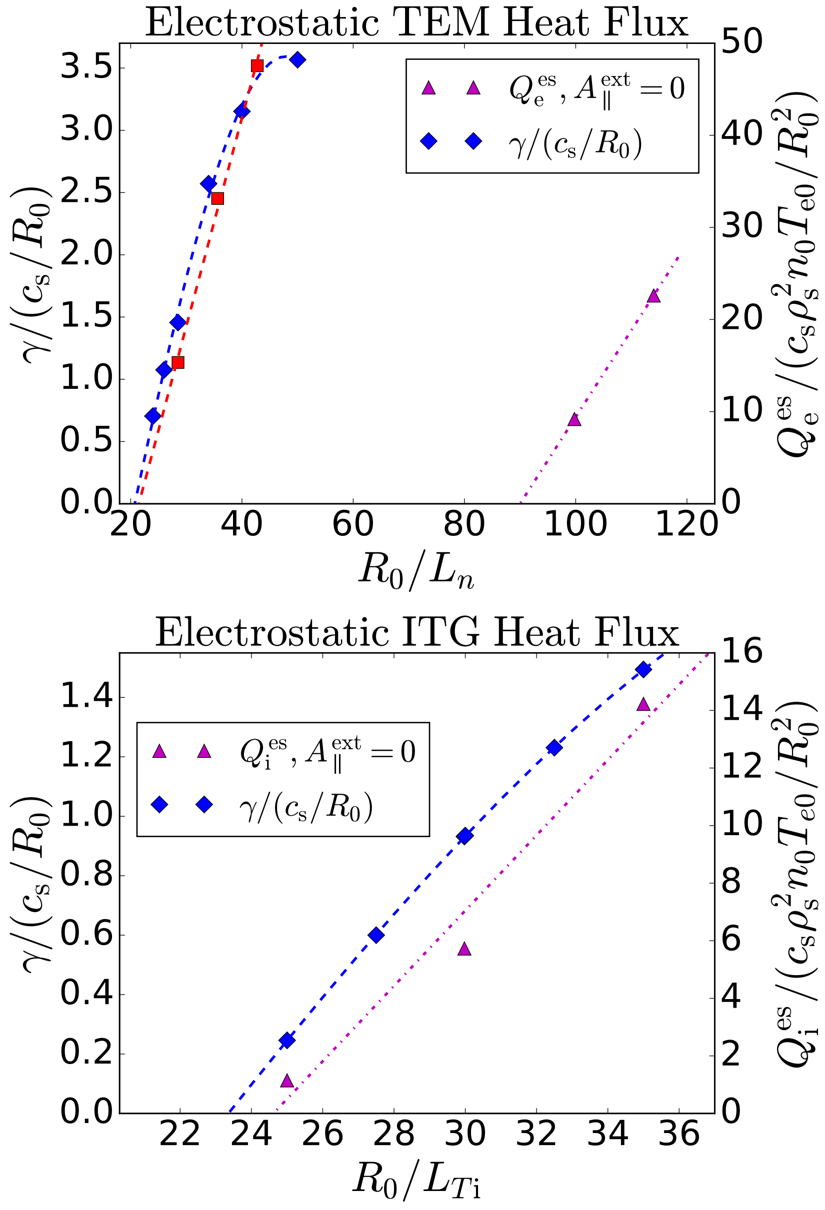

Figure 3.7: Linear growth rates and heat fluxes (in units of $c_{\mathrm{s}}\rho_{\mathrm{e}}^2 n_0 T_{\mathrm{e}0}/R_0^2$) vs. driving gradients. Diamonds correspond to linear growth rates, triangles to heat fluxes without the tearing perturbation imposed, and squares to heat fluxes with the imposed tearing perturbation. Top: For TEM without magnetic perturbations modeling tearing mode effects, the linear (blue diamonds) and nonlinear (magenta triangles) critical gradients differ by a factor of four. With tearing (red squares), they nearly coincide. Bottom: even without tearing activity, there is almost no difference between linear and nonlinear critical gradients in the ITG case.

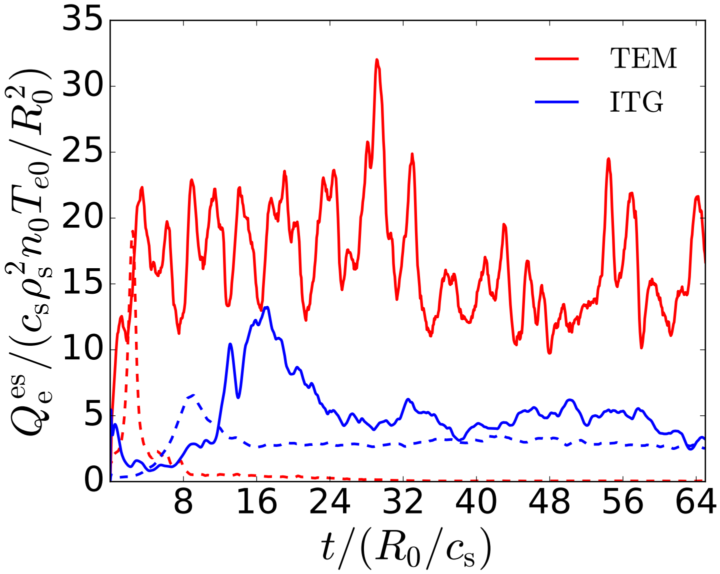

Figure 3.8: Electrostatic heat flux time traces, with (solid) and without (dashed) a magnetic perturbation modeling tearing modes. TEM transport (red lines) is increased by orders of magnitude, while time-averaged ITG transport (blue lines) exhibits only a small change, despite imposing an identical tearing perturbation.

zonal flows, only in the TEM case is transport affected so severely. In the absence of tearing fluctuations, the ITG-dominated simulation at experimental gradients still exhibits finite transport, despite also establishing prominent zonal flows. Including the tearing perturbation results in only a slight increase in fluxes for ITG, depicted in Fig. 3.8. It should be noted that zonal flows are still eroded by the tearing perturbation in the ITG case, exhibiting a change in zonal flow structure comparable to that seen in Fig. 3.6 for the TEM case. Additionally, the Dimits shift in the ITG case is very small compared to the TEM case as well as standard tokamak cases (e.g. order 50% that (Dimits et al., 2000) reports), even in the absence of tearing fluctuations.

In an ITG simulation which removes contributions from zonal flows (zeroing out the flux-surface-averaged electrostatic potential Φ at every time step), the increase in flux is of the same order as that seen in the case in which tearing fluctuations reduce the zonal flow (factor of 2 increase in flux when tearing perturbation is applied vs. factor of 3 increase when zonal Φ contributions are removed). This suggests that in this ITG-dominated discharge, zonal flows do not regulate transport nearly as much as they do in the TEM case (in which both the tearing perturbation and the removal of zonal Φ result in orders of magnitude transport increase).

There is evidence that this behavior is rooted in the branch of unstable ITG mode favored by the equilibrium and the corresponding type of mode coupling interaction that dominates saturation. In the tokamak, ITG instability comes in two varieties, a so-called slab ITG branch with a mode structure that is flute-like and governed by magnetic shear, and a toroidal branch with a ballooning mode structure governed by magnetic curvature (Horton et al., 1981). The choice of which branch is favored depends on the relative magnitudes of the parallel and curvature drift frequencies. In the slab ITG branch, mode coupling between the unstable ITG mode and a conjugate stable mode that dominates saturation is mediated by a marginally stable eigenmode (Terry et al., 2009). In the toroidal branch, a balance of parallel flow with shear, the poloidal variation, and radial wave propagation removes the marginal mode from the linear eigenmode spectrum as described in (Horton et al., 1981). Mode coupling then favors a saturation channel that uses the zonal flow, thereby introducing zonal-flow regulation (Holland et al., 2003; Makwana et al., 2012, 2014). Gyrokinetic simulations of ITG turbulence in a stellarator support this picture of mode coupling. Zonal flows have a significant impact on saturation when the toroidal branch dominates. When the shear is strengthened only enough to bring the parallel and curvature drift frequencies to comparable values, the zonal flow no longer dominates saturation (Faber et al., 2018; Hegna et al., 2018). Instead, removing zonal flows results in only a slight increase in saturation level for this stellarator case, much like the situation described here for ITG turbulence in the RFP. Moreover, analysis of wavenumber triplet interactions further confirms that non-zonal couplings become dominant in the regime of comparable drifts.

The parameter that delineates the two branches of ITG instability is the ratio of scale lengths of magnetic shear to magnetic curvature L_s/κ^{-1}, where $\kappa \approx \nabla_\perp B/B$ in a low-β plasma. For $L_s/\kappa^{-1} < 0.5$ the mode is slab-like, while in the opposite limit, it is a curvature dominated mode.

For tokamaks, L_s is given by the formula $L_s = Rq/\hat{s}$, where $\hat{s} = (r/q)dq/dr$. In the RFP, the comparable magnitudes of toroidal and poloidal fields invalidate the tokamak expression for shear in the outer half of the plasma, and instead $L_s = r/(Rdq/dr)$. It should also be noted that the magnetic field curvature that dominates in most of the plasma volume of the RFP is the poloidal-field curvature.

For the ITG-dominated discharge, the shear and curvature scale lengths were $L_s = 0.21\,\mathrm{m}$ and $\kappa^{-1} = 0.47\,\mathrm{m}$, making $L_s/\kappa^{-1} = 0.45$. This places the plasma at the cross-over between the two ITG branches, and critically, from the arguments given above indicates that zonal flows do not play a dominant role in saturation.

These results are also consistent with an analysis of parallel mode structure as quantified by $c_{\mathrm{s}}k_{\|}/\omega$, where $c_{\mathrm{s}} = (T_{\mathrm{e}}/m_{\mathrm{i}})^{1/2}$ is a characteristic sound speed, $k_{\|}$ is a parallel wavenumber (normalized to R_0) calculated from the width of the mode along the field, and ω is the linear frequency of the mode. For ITG modes dominated by curvature, one expects localized mode structures with large $k_{\|}$, or $c_{\mathrm{s}}k_{\|}/\omega > 1$, while for modes dominated by shear one expects a more extended structure with $c_{\mathrm{s}}k_{\|}/\omega < 1$. For the ITG instability discussed in this chapter, $c_{\mathrm{s}}k_{\|}/\omega \approx 0.3$, while $c_{\mathrm{s}}k_{\|}/\omega \approx 1.1$ for the Cyclone Base Case parameters of (Dimits et al., 2000), which represents a typical tokamak core plasma scenario.

3.3 Zonal Flow Characterization

To model the MST experiment, it is necessary for microturbulence models to incorporate tearing perturbations. Because tearing mode suppression is a goal of current profile control in the RFP, the behavior of zonal flows and turbulence observed in the absence of tearing modes is a key subject of investigation. In particular, if the RFP could operate with full tearing suppression, it would likely be able to sustain much steeper gradient profiles then tokamaks, thus enhancing its performance, as predicted in (Terry et al., 2015). In light of the preceding discussion, there are two properties of these RFP discharges that merit investigation: (1) the ability (in the absence of tearing modes) to support very strong zonal flows, and (2) the fact that zonal flows play very different roles in saturation for the ITG and TEM discharges. The first point is addressed by examining the Rosenbluth-Hinton zonal-flow residual for RFP geometries. The second point is addressed through examining collisional effects and secondary instability drive.

Rosenbluth-Hinton Residual

One aspect of zonal flow behavior is the residual, described in (Rosenbluth and Hinton, 1998). An impulsive electrostatic potential is applied to a flux surface and the plasma responds through a shielding process in which the system arrives at a new constant amplitude Φ_{res}, called the *zonal flow residual* (Sugama and Watanabe, 2006). Transient geodesic acoustic modes (GAMs) are also observed in the evolution towards the residual. The amplitude of this residual is

$$\frac{\Phi_{\rm res}}{\Phi_0} = \frac{1}{1 + 1.6q^2/\epsilon_{\rm t}^{1/2}} \quad , \tag{3.1}$$

where Φ_0 is the initial amplitude of the electrostatic potential, and $\epsilon_{\rm t} \equiv r/R_0$. This equation can be thought of as a measure of the ability of the plasma to maintain a zonal flow amplitude set by an instantaneous perturbation. The associated physics has been characterized extensively through numerical simulation (see (Sugama and Watanabe, 2006) for example). To characterize the zonal flow residual behavior using gyrokinetics, a reduced system with only three modes (corresponding to $k_y = 0$, $k_x = -1, 0$ or 1 indices) is modeled nonlinearly from a GAM initial condition. These simulations include no information about pressure gradients or collisions, but all the information about the equilibrium magnetic field geometry that is used in the full nonlinear simulations. The initial GAM experiences Landau-damping, and what amplitude remains in Φ is the aforementioned zonal flow residual. For the magnetic geometry of the present discharges, Fig. 3.9 shows that the residual is measured to be considerably larger than what is seen in the Cyclone Base Case (CBC), a standard tokamak parameter set, and is still well predicted by Eq. (3.1). The RFP's low toroidal magnetic field leads to a safety factor q that is at least an order of magnitude smaller than that of the tokamak, resulting in the significantly larger residual. This behavior had been noted previously by (Predebon and Xanthopoulos, 2015) in the context of RFX-Mod RFP discharges.

In performing this calculation over a variety of q values, Fig. 3.10 shows that Eq. (3.1) it applies to both tokamak and RFP regimes. Large residuals of the RFP are a contributor to the strong zonal flows seen in the present simulations. It is important to note that the large zonal flow residuals discussed here apply to plasmas with perfectly axisymmetric flux surfaces; experimental reality is better described by including residual tearing fluctuations. As discussed in (Terry et al., 2013) and in Sec. III, the presence of resonant magnetic fluctuations, such as those arising in MST from residual tearing modes, serves to reduce zonal flow amplitudes. For more details on the deleterious impact of electromagnetic effects on zonal flow residuals, see (Pueschel et al., 2013b).

While large zonal flow residuals are consistent with the strong zonal flows seen for simulations unaffected by tearing modes, they fail to distinguish between turbulence regimes governed by different instabilities and thus provide no information concerning the difference between zonal flow activity in TEM and ITG turbulence regimes. Such differences are discussed in the following sections.

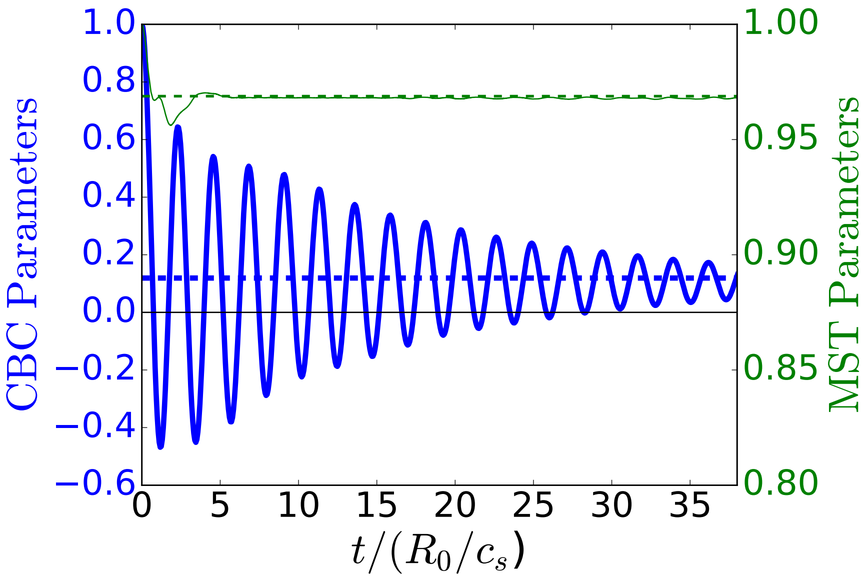

Figure 3.9: Electrostatic potential Φ/Φ_0 evolves toward the zonal flow residual (dashed lines), in good agreement with Eq. (3.1) for both MST parameters (thin green line, right axis) and CBC (thick blue line, left axis). The small q of the RFP results in a much larger residual value. This calculation was performed at zonal flow wavenumbers of $k_x\rho_\mathrm{s} = 0.05$ for the CBC and $k_x\rho_\mathrm{s} = 0.3881$ for MST; these wavenumbers correspond to the larger spatial scale permitted by the radial box size.

Collisionality

In tokamaks, TEM turbulent amplitudes have been observed to vary with collisionality (Ernst et al., 2006). In particular, higher electron-ion collisionality in a plasma will lead to an increase in electron detrapping, reducing TEM growth rates. Increased collisionality also erodes zonal flows. However, the zonal-flow erosion is less pronounced than the growth rate reduction. Consequently, the balance of the growth rate to the zonal flow level is affected, leading to proportionally stronger zonal-flow regulation as the fluctuations decrease. The effect of collisionality on TEM and ITG modes in the RFP is shown in Fig. 3.11, in which the electrostatic heat flux vs. driving gradient from nonlinear simulations is compared with the linear growth rate vs. driving gradient in linear simulations. The observed trends are similar to those in tokamaks for the TEM-dominated discharge. Figure 3.11(a) shows that when the collisionality is raised from half its nominal experimental value to the experimental value ν_c, the growth rate decreases by 50%. Note that $\nu_\mathrm{c} \equiv (R_0/4v_{T\mathrm{e}})\nu_\mathrm{ei}$ for the cases studied here, where $v_{T\mathrm{e}}$ is the electron thermal speed and ν_ei is the electron-ion collision frequency in

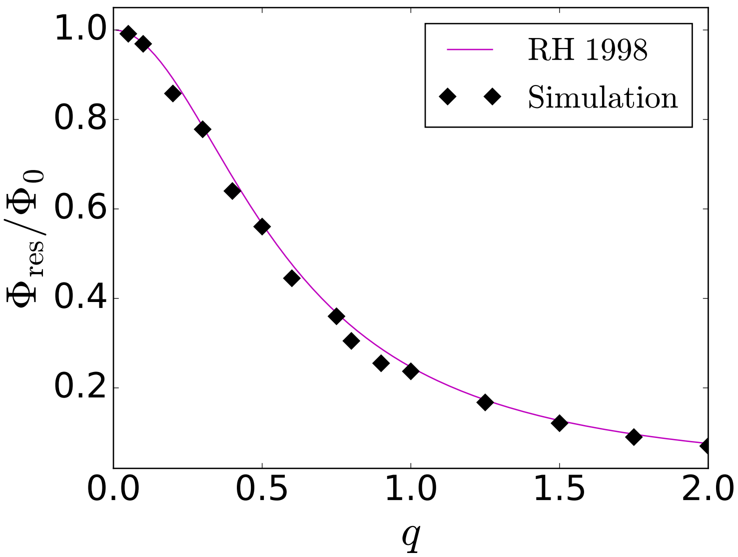

Figure 3.10: Scaling of zonal flow residual with safety factor q, showing applicability of Eq. (3.1) for both tokamak ($q \gtrsim 1$) and RFP ($q \ll 1$) regimes, performed at $k_x\rho_{\mathrm{s}} = 0.3881$ and $\epsilon_{\mathrm{t}} = 0.2741$.

units of Hz.

However, despite an increase in zonal flow damping, the Dimits shift increases (as made evident in Fig. 3.11(a) by the increased critical gradient for $Q_{\mathrm{e}}^{\mathrm{es}}$), suggesting that the effect of collisions on the zonal flow is weaker than their effect on the growth rate. This is confirmed by examining how zonal flow residuals and linear growth rates are affected by collisionality. For the TEM case, a factor of two increase in collisionality (from half the experimental value to its full value) results in a 40% reduction of linear growth rates, but only a 30% increase in the zonal flow decay rate, consistent with the results shown in Fig. 3.11. This indicates that transport regulation of TEM turbulence is increased in a more collisional plasma.

In contrast, Fig. 3.11(b) shows that collisionality has little effect on either the ITG growth rate or the heat flux. For this case, doubling collisionality causes the zonal flow decay rate to increase by 25% and the linear growth rate to decrease by 10%. The lack of change in ITG Dimits shift is consistent with previously discussed observations that zonal flows play a less important role in turbulence saturation for the ITG discharge, with collisions working analogously to the tearing fluctuation as a source of zonal flow degradation.

The specific MST data sets analyzed in this chapter have plasma densities comparable to typical tokamak discharges, but lower temperatures (core $T_{\mathrm{e0}} \approx 500 - 600$ eV), leading to a higher collisionality $\nu_\mathrm{c} \sim 10^{-1} - 10^{-2}$. For comparison, typical collisionalities in tokamak gyrokinetic simulations in the region of interest ($r/a \approx 0.8$) are at most $\nu_\mathrm{c} \sim 10^{-3}$, as described in (Told et al., 2013). This high-collisionality regime of operation thus contributes to the strong zonal-flow suppression of TEM turbulence observed in simulation by increasing the Dimits shift, while having little effect on ITG turbulence.

Secondary Instability

Secondary instability analysis, defined in (Cowley et al., 1991) and (Rogers et al., 2000), describes the process by which a linear instability (e.g. TEM or ITG) causes the excitation of a secondary instability in the zonal wavenumber $k_y = 0$ via nonlinear coupling. The secondary instability growth rate is a measure of nonlinear zonal flow excitation rate. Specific details on the procedure for secondary instability analysis are given in (Pueschel et al., 2013a). To summarize, a streamer ($k_x = 0, \text{finite } k_y$) representing the typically fastest-growing linear eigenmode is allowed to evolve through a linear calculation that includes a sideband (both k_x and k_y finite, not connected to the streamer via the parallel flux tube boundary condition) and a zonal flow, until the mode is converged. That state is then used as an initial condition in a subsequent simulation where the linear drive term is set to zero to disable linear sideband growth and the streamer is held fixed in time. The nonlinear interaction in the streamer-sideband-zonal-flow triplet results in exponential growth of the secondary mode, here the zonal flow. A secondary growth rate can then be calculated.

Parametric dependencies of the secondary growth rate are studied using scans over magnetic shear $\hat{s}$ and radial wavenumber k_x, shown in Fig. 3.12. For experimentally relevant parameters (denoted in the figure by circled points), the TEM secondary growth rate is more than twice that of the ITG secondary mode. This underscores that in the TEM case, zonal flow drive is too strong for turbulence to fully develop, while in the ITG case, the slower timescale of zonal flow development allows for more turbulent activity to arise. While Fig. 3.12(b) shows the TEM and ITG secondary growth rates peaking at the same radial wavenumber, in nonlinear simulations, TEM turbulence preferentially generates zonal flows at larger k_x than ITG turbulence. Figure 3.13 further illustrates this preference in TEM turbulence for smaller radial zonal structures, showing zonal flow spectra taken from nonlinear simulations. Higher-k_x zonal flows can result in a more effective regulation of turbulence, either through increased eddy shearing (Terry, 2000) or a larger rate of nonlinear energy transfer to damped modes (Makwana et al., 2012). The reason for the predilection for higher-wavenumber zonal flows in TEM turbulence remains an open question for further

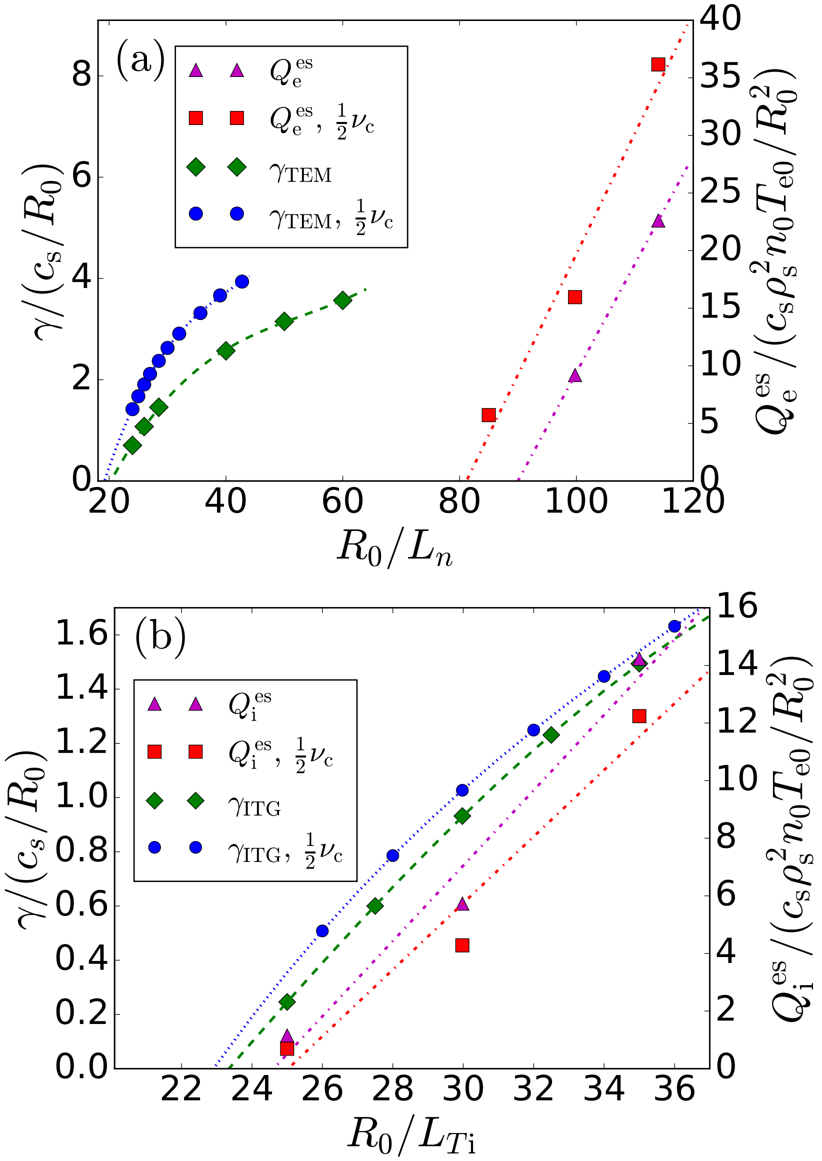

Figure 3.11: Linear growth rates and heat fluxes over a range of driving gradients at nominal(diamonds and triangles, respectively) and half nominal (circles and squares, respectively) ν_{c}. From this, one can measure the Dimits shift change with respect to collisionality for (a) TEM and (b) ITG. Increasing collisionality results in an increase of the Dimits shift in TEM but no significant change for ITG turbulence.

study.

3.4 Chapter Summary

Microturbulence in the MST reversed-field pinch has been studied through gyrokinetic simulations that model high-frequency fluctuations measured in improved-confinement PPCD discharges. Linear simulations from two separate data sets were analyzed, and the dominant instabilities were identified as density-gradient-driven TEM and ITG. Nonlinear simulations with no external magnetic field model for tearing mode fluctuations produced turbulence in both cases with very strong zonal flows, and transport levels were well below the experimentally observed levels. An external, constant-in-time magnetic tearing perturbation was then imposed in the simulations to model the effect of residual tearing modes in PPCD discharges. In both the TEM and ITG cases, this degraded the zonal structures, although with a different result in each case. For TEM, the transport was increased by orders of magnitude, reaching a value on the order of that expected from experiment. However, the ITG transport was affected far less, increasing only by approximately a factor of two. This is seen to be a consequence of the ITG exhibiting slab-like character, a mode branch which depends less on zonal flows for saturation. In the absence of the tearing fluctuation, it was observed that RFPs tend to form very strong zonal flows as a consequence of their unique magnetic geometry. A comparison of zonal flow formation in the TEM and ITG discharges through secondary instability analysis and an examination of collisionality effects were consistent with the zonal flows playing a more significant role in the ∇n-TEM discharge.

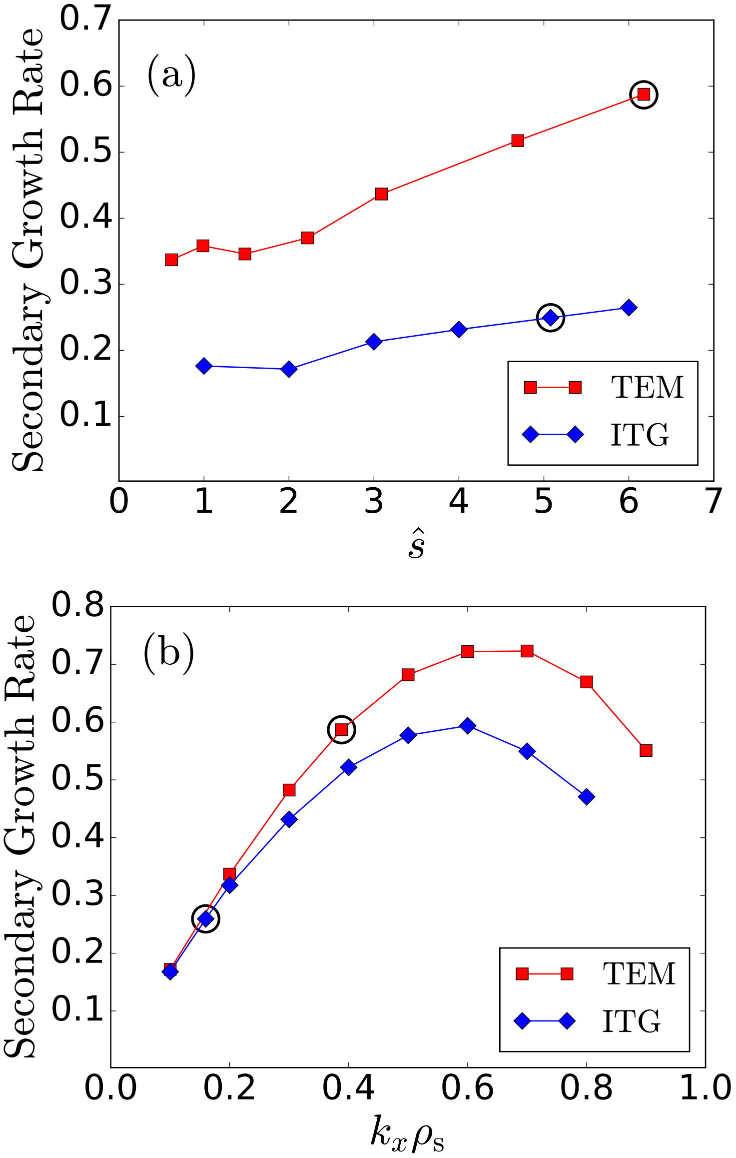

Figure 3.12: Secondary growth rate vs. (a) background magnetic shear and (b) radial wavenumber for the two discharges of interest. For default experimental parameters (circled points), the zonal flow secondary growth rate in the TEM case (red squares) is more than two times as large as in the ITG case (blue diamonds), in agreement with the observation of stronger zonal structures for the TEM discharge.

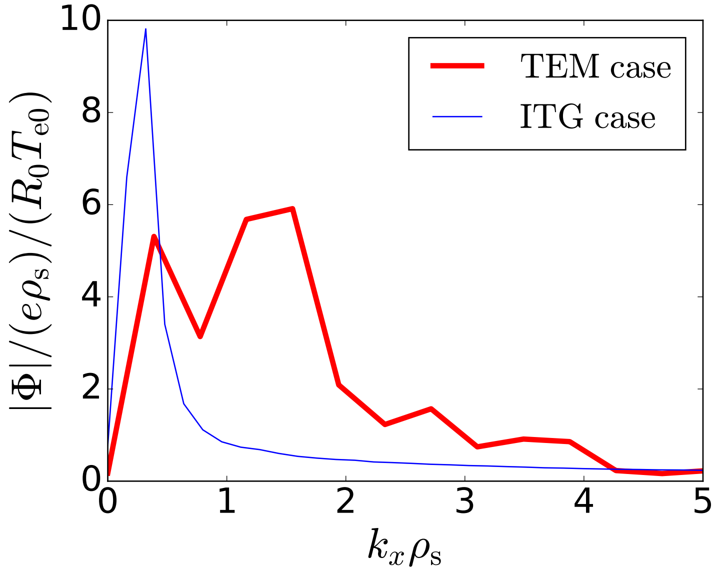

Figure 3.13: Zonal flow amplitude spectra from nonlinear simulations, time-averaged over the quasi-stationary state. The zonal flows in the TEM case (thick red line) manifest at higher radial wavenumber than those in the ITG case (thin blue line).

4 RESONANT MAGNETIC PERTURBATIONS, ZONAL FLOWS, AND MICROTURBULENCE IN THE DIII-D TOKAMAK

The results of Chapter 3 motivated a search to determine if the interaction among zonal flows, magnetic fluctuations, and microturbulence can occur in different fusion device contexts, using observations from both experimental measurements and theoretical predictions. In order to measure how turbulence and zonal flows vary with large-scale magnetic fluctuation activity, it is desirable to have direct control over the amplitude of the large-scale magnetic fluctuations in question. Precise control of tearing mode amplitudes is unfortunately untenable in the reversed-field pinch. However, there exists another context in which both microturbulence and large-scale magnetic fluctuations are present: resonant magnetic perturbations (RMPs) in tokamaks.

RMPs are large-scale magnetic fluctuations imposed on the plasma equilibrium through the use of currents driven in external coils. Importantly, they are used on tokamaks as a means of mitigating Edge-Localized Modes or ELMs (Evans et al., 2006), which otherwise release bursts of large amounts of energy that can damage divertors in fusion devices. While this presents a significant benefit in the efforts towards sustained confinement in tokamaks, there are still many aspects of RMP effects on plasma dynamics that are not fully understood. It has been observed that when using RMPs to remove ELMs, high-frequency fluctuations arise (McKee et al., 2013). As will be explored in this chapter, RMPs play a significant role in governing turbulence and transport at small scales.

The concurrent presence of RMPs and microturbulence in tokamaks is analogous to the tearing fluctuations and microturbulence discussed in Chapter 3, and provides an additional avenue for exploring interactions among zonal flows, microturbulence, and large-scale magnetic activity. For the purpose of investigating the physics in question via experimental means, tokamak RMPs have a distinct advantage over tearing modes in RFPs in that the amplitude can be set by user input to a desired level. Thus, measurements can be performed that map specific magnetic fluctuation amplitudes to corresponding microturbulence levels and inform computational studies.

This chapter will briefly summarize the results from an experimental campaign exploring RMP-microturbulence interactions on the DIII-D tokamak, in which small-scale density fluctuations are seen to scale directly with RMP amplitude. The rest of the chapter describes the results of computational investigations of these discharges in order to better understand the connection between RMPs and microturbulence fluctuation levels. Simulations show that the RMP does have a nontrivial effect on equilibrium temperature and density profiles, affecting the relative levels of ITG and ∇T-TEM fluctuations, both of which are present in numerically modeled discharges. While zonal flows are not directly measured in the experiment, a significant effect is seen in the nonlinear simulations, which clearly show signatures of RMP-induced zonal flow erosion and a resultant increase in density fluctuations that agree qualitatively with BES measurements for a range of RMP values. Some apparent discrepancies that contrast this physical picture are addressed.

4.1 Microturbulence in DIII-D L-Mode Plasmas

A run campaign on the DIII-D tokamak characterized the effect of RMPs on high-frequency density fluctuations through the use of Beam Emission Spectroscopy (BES). While the experimental results were not obtained by the author of this thesis, they are summarized here to provide context for the discussion that follows.[1] On DIII-D, RMPs can be applied using either a set of six coils located outside the vessel (C-coils) or a set of twelve coils located within the vessel (I-coils); for these studies the I-coils were used. The RMP coil current was varied in steps over the course of an L-mode discharge (or “low-confinement” mode, characterized by increased turbulent activity and poorer confinement properties than the H- or ”high-confinement” mode), while density fluctuation spectra were measured concurrently using the BES probes. Scans were conducted to see how both RMP magnitude and parity affect microturbulence levels for $n = 1$ and $n = 3$ RMPs. Note that here parity refers to being even or odd with respect to the coil configurations, and does not translate directly into even or odd mode parity with respect to the outboard midplane. The latter is a common characterization of fluctuation structure. Resolving the largest spatial scales of $n = 1$ concurrently with microturbulence adds additional expense, and the approximation $k_\parallel \ll k_\perp$ breaks down at this scale. As such, this chapter will focus only on results from the RMP amplitude scan for the odd-parity $n = 3$ perturbation.

As seen in Fig. 4.1, the RMP was activated at a small (relative to ELM-suppression RMPs) ($B_r/B_0 \approx 7.6 \times 10^{-5}$) amplitude, and incrementally lowered, establishing four distinct phases of the discharge. Figure 4.2 shows profiles of electron density and temperature over different stages in the scan; the RMP does not result in any significant changes to the

---

[1] Special thanks to Takashi Nishizawa, Matt Kriete, Mark Nornberg, John Sarff, George McKee, and the scientists at DIII-D for producing the experimental results.

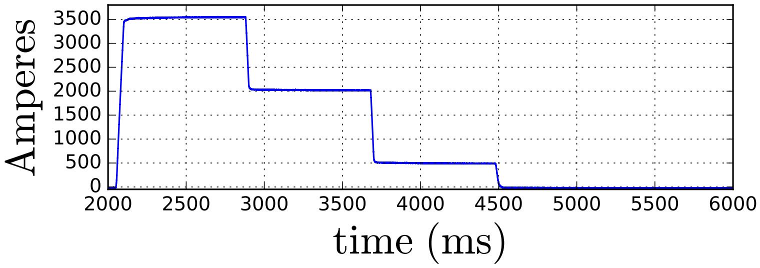

Figure 4.1: I-coil current as a function of time. The discharge is characterized by four distinct stages of RMP amplitude, with equilibrium quantities determined separately from time averages over each stage. Data courtesy of Matt Kriete.

radial profiles. This ramp-down scan in RMP amplitude was performed with the BES array centered at two different radial positions, measuring fluctuations spanning a total radial extent from $\psi_n = 0.67 - 1$, where ψ_n is the normalized poloidal flux coordinate such that $\psi_n = 1$ corresponds to the last closed flux surface. Figure 4.4 shows BES measurements of the time-averaged density fluctuation spectra at $\psi_n = 0.88$ (corresponding to the $q = 10/3$ rational surface, see Fig. 4.3) for each different phase of the RMP ramp-down. As the I-coil current is decreased, a corresponding decrease is observed in the density fluctuation levels in the $50 - 100$ kHz range, where one would expect ion-scale microturbulence. These measurements are suggestive of the same multi-scale physics previously discussed, wherein the RMP leads to zonal flow reduction which affects small-scale turbulence levels. Previous efforts have measured properties of zonal flows in DIII-D (McKee et al., 2006), but such measurements were not attempted during this campaign so it is not possible to directly attribute the observations to changes in zonal flow amplitudes from experimental data alone.

To more thoroughly understand the experimentally observed effect, these discharges are studied using the gyrokinetics code Gene. Linear simulations evaluate how much varying the RMP amplitude affects equilibrium stability properties. Analysis is performed separately for each phase of the ramp-down scan at the radial location of interest ($\psi_n = 0.88$), with input parameters taken from experimental profile data generated via time-averaging of each phase of the scan. The magnetic geometry was determined separately for each stage in the RMP amplitude ramp down via TRACER-EFIT (Xanthopoulos et al., 2009), which contains information about the equilibrium magnetic field configuration excluding RMP effects. Resolutions used for the linear calculations include 31 k_x modes, 16 z, 32 $v_{\parallel}$, and 8 μ grid points. Relevant physical input parameters at each point of the RMP amplitude

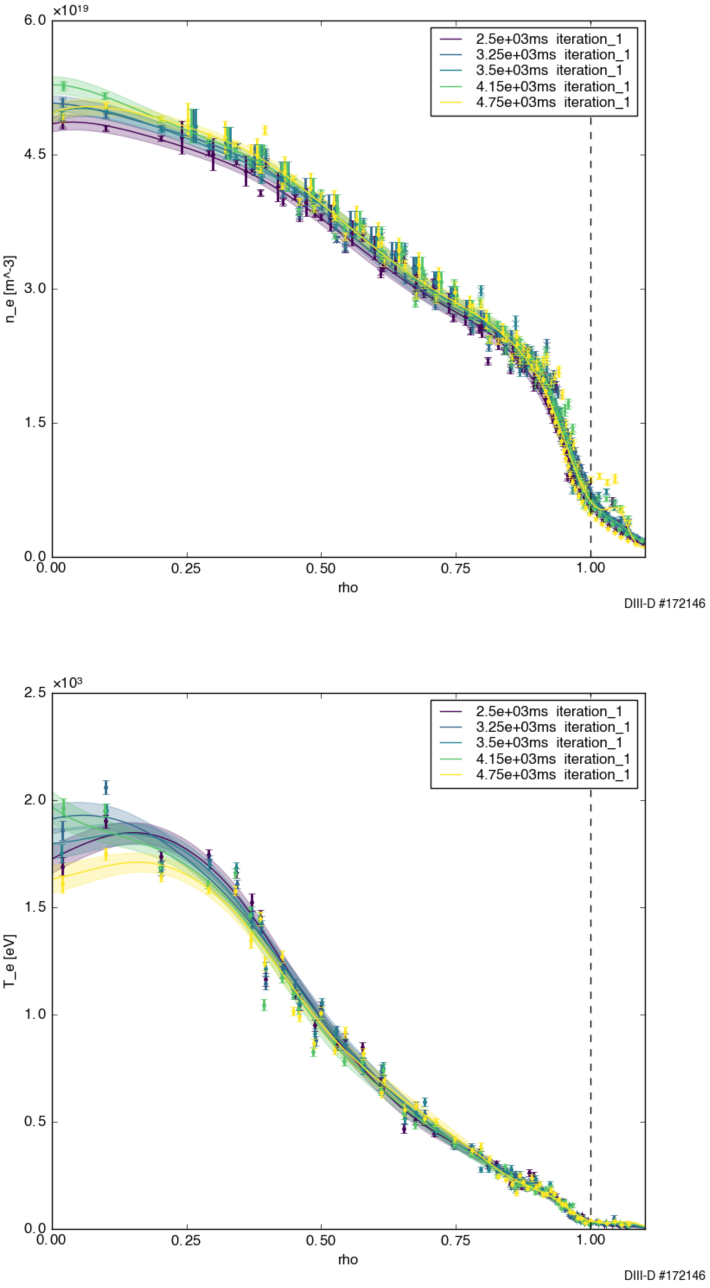

Figure 4.2: Radial profiles of electron density (top) and temperature (bottom) for different points in time during the RMP amplitude scan. The RMP produces no significant variation in radial profiles, though normalized gradients do vary nontrivially towards the edge of the device. Courtesy of Mark Nornberg and DIII-D Frontier Science.

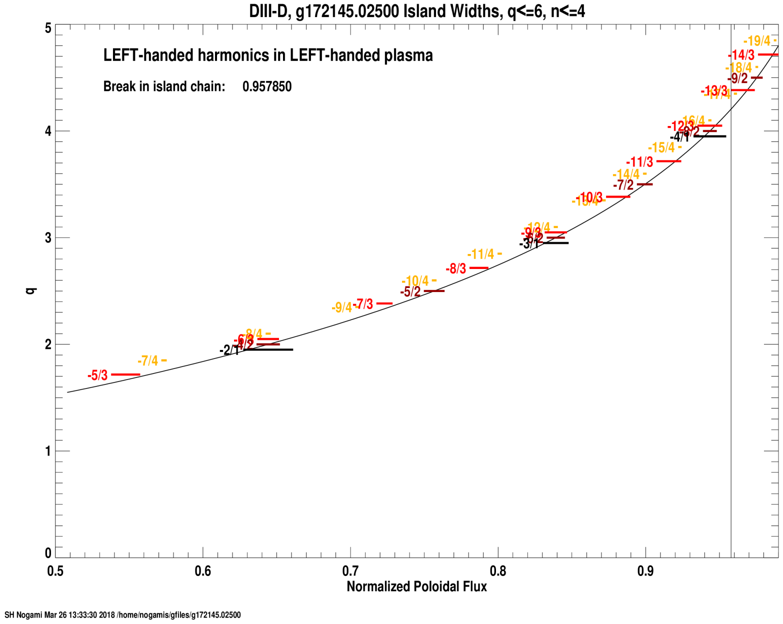

Figure 4.3: q profile during the largest-RMP portion of the amplitude scan as a functio of normalized poloidal flux. $n = 3$ island widths are increased with application of the RMP through the radial extent of the device. This work focuses on the $q = 10/3$ island located at $\psi_n = 0.88$. Generated using SURFmn, courtesy of Sam Nogami.

scan are given in Table 4.1. It is important to note that these simulations, and in all that follow, use an artificially lowered value for normalized plasma pressure of $\beta = 10^{-4}$, approximately a factor of four lower than the average experimental β at this radial location. At the nominal β, an anomalous linear instability appears at low wavenumbers and persists for $k_y \rho_\mathrm{s} < 0.005$, which corresponds to spatial scales exceeding the device size. This anomalous mode, which when included drives high levels of electromagnetic turbulence that never saturate, is likely attributable to the inaccuracies of the flux-tube prescription that arise at very low k_y. Specifically, the equations used in the GENE code assume negligible parallel derivatives which affect Ampère's Law, an assumption which does not hold at sufficiently large scale and thus can lead to nonphysical electromagnetic behavior. Reducing β serves to remove this large-scale instability without appreciable changes to the linear ion-scale physics (see Fig. 4.5).

When analyzing results using an initial value solver, the dominant instability varies

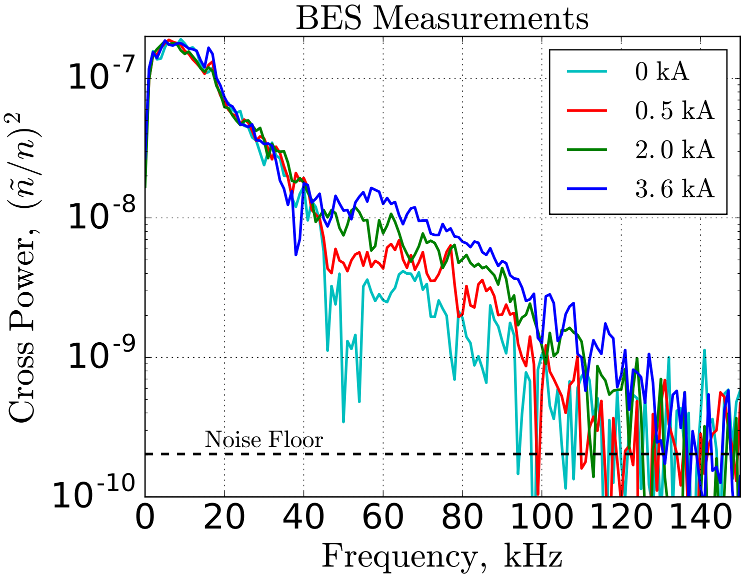

Figure 4.4: Experimental measurements of density fluctuation spectra taken with Beam Emission Spectroscopy at $\psi_n = 0.88$, averaged in time over each distinct phase of the I-coil current scan. There is a increase in density fluctuations at microturbulent frequencies with increasing RMP amplitude. Data courtesy of Matt Kriete.

I-coil Current	0 kA	0.5 kA	2.0 kA	3.6 kA
ω_n	2.903	2.198	2.396	3.142
$\omega_{T\mathrm{i}}$	3.663	4.066	3.155	3.343
$\omega_{T\mathrm{e}}$	5.708	5.016	5.958	5.797
$\hat{s}$	2.376	2.335	2.284	2.258
$\nu_\mathrm{c}[10^{-2}]$	1.143	1.234	1.086	1.076
T_i [keV]	0.393	0.370	0.385	0.406
T_e [keV]	0.219	0.222	0.233	0.235
$\rho^*[10^{-3}]$	1.29	1.27	1.31	1.29

Table 4.1: Physical parameters used for simulations performed at $\psi_n = 0.88$, the $q = 10/3$ flux surface. $\omega_X \equiv (a/X)(dX/dr)$ represents normalized gradients, where $X = (n, T_\mathrm{i}, T_\mathrm{e})$ for density, ion temperature, and electron temperature, respectively. $B_\mathrm{ref} = 2.1$ T, $L_\mathrm{ref} = 0.803$ m for all I-coil current values.

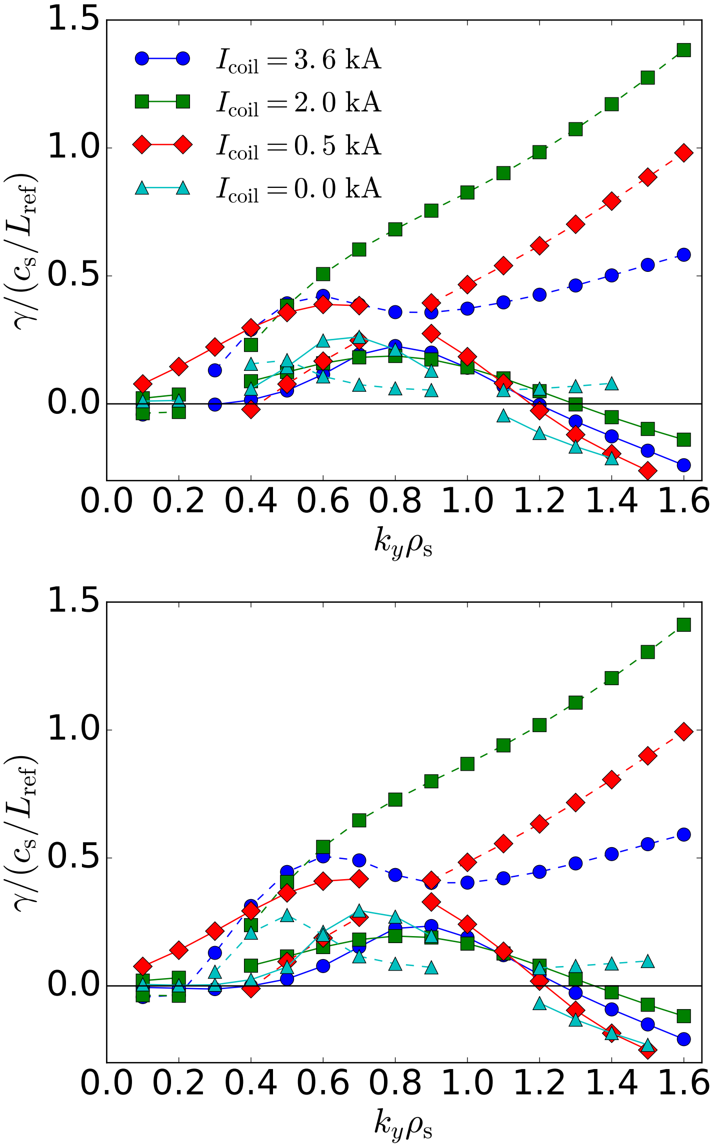

Figure 4.5: Variation in linear growth rate spectra with RMP amplitude at $\psi_n = 0.88$. Solid lines represent ion-direction modes (corresponding to ITG instability), dashed lines represent electron-direction modes (∇T-TEM). Simulations are compared at experimental β (top) and artificially lowered β (bottom); the physical modes are almost entirely unaffected by changes in β.

significantly with RMP amplitude, jumping back and forth between modes with electron- and ion-diamagnetic propagation directions. However, upon examining the stability of several eigenvalues, one finds that across all of the RMP amplitudes there exist a ∇T-driven trapped-electron mode (TEM) and an ion temperature gradient (ITG) mode with similar growth rates, such that slight variations in equilibrium gradient drives shift which instability is dominant, shown in Fig. 4.5. The variation in normalized gradients listed in Table 4.1 fall within error bars comparable to those expected for DIII-D L-mode discharges at this radial location, see Fig. 8 in (Holland, 2016). The ITG mode is localized to ion gyroradius scales as one would expect, while the TEM continues to grow beyond $k_y\rho_\mathrm{s} \approx 1$, likely transitioning into an Electron-Temperature-Gradient (ETG) mode. As the physics focus for this chapter concerns fluctuations at ion-scales and larger, calculating the growth rates for the high-k_y ETG is not necessary; nonlinear convergence testing shows negligible contributions to transport from electron scales. While both ITG and TEM linear instabilities persist across all RMP amplitudes, the variations in growth rates suggest that the RMP has a nontrivial effect on the equilibrium stability. It is, however, unlikely that the experimentally observed changes in density fluctuations with RMP amplitude can be attributed to changes in linear growth rates, as the linear changes vary non-monotonically with the RMP. This implies that the key experimental observations must be attributed to nonlinear physics.

4.2 Interaction of RMP and Microturbulence

Nonlinear simulations are used to further explore what effect connects microturbulence and RMP amplitudes. These simulations include two kinetic species (electrons and deuterium ions) and resolve dynamics of both the large-scale RMP physics and the ion-scale microturbulence, with a minimum $k_y\rho_\mathrm{s} = 0.015$ (corresponding to $n = 3$) and 128 $k_y\rho_\mathrm{s}$ modes. Additional resolutions include 192 k_x modes, 16 z, 32 $v_\parallel$, and 8 μ points. Resolving such a broad spectrum of k_y modes leads to significant numerical expense; the discussion that follows focuses on the $I_\mathrm{coil} = 0.5\,\mathrm{kA}$ equilibrium, which shows the least high-k_y ETG activity, reducing the number of k_y modes required for convergence. This equilibrium exhibits the strongest presence of ITG among the four linear instability spectra, for which the toroidal branch is regulated heavily by zonal flows, and thus serves at the best candidate for this investigation.

As previously mentioned, the magnetic geometry used for these calculations is generated from experimental data, but the magnetic structure does not include the RMP (even for the finite I-coil currents). Instead, magnetic fluctuations from the RMP are included using

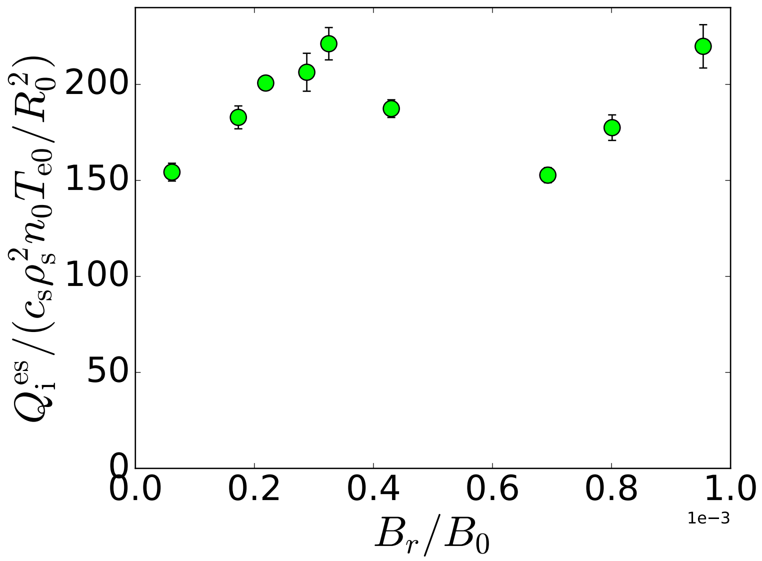

Figure 4.6: Electrostatic ion heat flux versus radial magnetic field strength, showing how RMP amplitude affects turbulence levels; error bars are a result of time averaging the flux over the quasi-stationary state. The non-monotonic behavior suggests the presence of physics beyond just zonal flow erosion.

the same procedure as discussed in the previous chapter and in Appendix A. An important distinction is that while in Chapter 3, the magnetic fluctuations were imposed at the lowest k_y values of the microturbulence, here the RMP is applied at the minimum $k_y\rho_{\rm s} = 0.015$ and is thus an order of magnitude removed in scale from the peak-growth-rate microinstabilities.

To establish a base scenario, a nonlinear simulation without the applied RMP is run and allowed to reach a quasi-stationary turbulent state. The $A_\parallel$ perturbation is then introduced in a continuation of the simulation, and the system is allowed to reach a new quasi-stationary state; this has been compared with simulations in which the perturbation was applied from the beginning, which results in the same saturated transport values. After application of the perturbation, B_r at the imposed k_y increases gradually due to the plasma response until it saturates; values quoted for B_r/B_0 in the following discussion refer to that saturated amplitude.

The variation in electrostatic heat flux with radial magnetic field amplitude is shown in Fig. 4.6 for a range of resultant B_r amplitudes. This figure contains two features that are seemingly at odds with expectations: 1) the B_r values are significantly (by approximately an order of magnitude) larger than those used in the experiment, and 2) the electrostatic transport scales non-monotonically with B_r. The first discrepancy is addressed via the artificially low β which is a factor of four lower in the simulation than in the experiment. As the resultant quoted B_r amplitudes are a consequence of the externally imposed perturbation combined with the plasma electromagnetic response, a lower β means that the B_r produced by plasma magnetic response is correspondingly reduced and thus a larger imposed B_r is needed. To examine the need for increased radial field strength more quantitatively, one can calculate the magnetic diffusivity resulting from both experiment and simulation. This calculation was performed as described in (Rechester and Rosenbluth, 1978) and (Nevins et al., 2011), with the average field line wandering being calculated from a Poincaré plot of 200 radially-equidistantly seeded lines over 60 poloidal turns. The data for the experimental magnetic diffusivity is determined from the equilibrium vacuum field at each different point in the RMP amplitude scan[2], while the simulation magnetic diffusivity is determined from the saturated state, which includes the plasma magnetic response. This difference means that the comparison is not direct, but still allows for a qualitative assessment and comparison of diffusivities. The comparison of these experimental and computational magnetic field diffusivities is presented in Fig. 4.7. As demonstrated in the figure, applying B_r values comparable to those used in the experiment would not produce any magnetic diffusion due to the lowered value of β. As β cannot be increased in simulation due to the previously discussed non-physical, large-scale mode that develops, B_r serves as the tuning parameter to increase plasma magnetic activity. Note that because of the small values for B_r used in the experiment, the order of magnitude increase places the B_r used in simulation in the same range as that normally used for ELM suppression (Evans et al., 2006), and thus are still physically relevant.

Using these necessarily larger B_r values, the non-monotonicity of flux scaling still needs to be understood. Informed via the perspective of magnetic-flutter-induced zonal flow erosion, one would reasonably expect the transport to increase monotonically with magnetic field perturbation, or perhaps level off at some point at which the zonal flows are entirely removed. A possible mechanism for the observed drop in transport over a range of B_r values relies on the concept of profile corrugations, from (Waltz et al., 2006). In flux-tube calculations, pressure gradients are assumed constant. However, time-averaged fluctuations in a saturated state, such as density or temperature perturbations, vary over the radial domain (but are constant within flux surfaces, $m = n = 0$). These fluctuating profiles have their own gradients (corrugations), which can serve as an additional drive on top of the equilibrium gradients to

---

[2] Credit to Dmitri Orlov

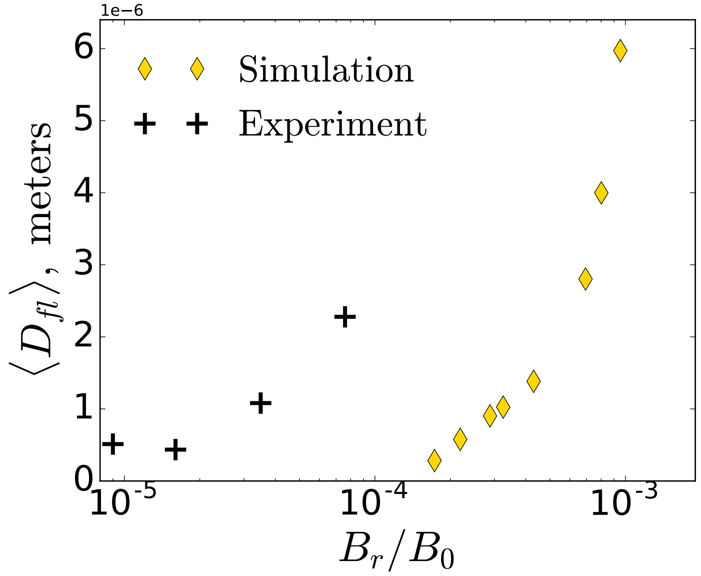

Figure 4.7: Magnetic field diffusivity versus radial magnetic field strength. The order-of-magnitude difference in B_r/B_0 between experiment and simulation needed to produce comparable magnetic diffusivity is attributed to the lower β used for simulation purposes. At the experimental β, the plasma accesses the regime for zonal-flow degrading magnetic flutter much more readily.

enhance turbulence citepWaltz10,Pueschel13Secondary. As seen in Fig. 4.8, which shows an example of a fluctuating temperature gradient, these enhancements to the turbulence are not spread over the entire simulation domain but are instead radially localized. The scale length to which this localization occurs is called a *corrugation length*; for example, in Fig. 4.8, this length is approximately 25 ρ_s.

Corrugations vary above and below equilibrium values (typically in a sinusoidal fashion for flux-tube simulations), so if a large enough radial region is sampled by a moving particle along its trajectory then the modifications introduced by these corrugations can average out. Generally, this occurs for radial regions $\gtrsim 1$ corrugation length. When an RMP is applied at a resonant surface, an island forms, allowing particles to move very rapidly radially by one island width. Consider island structures overlaid on temperature corrugation contours, as shown in Fig. 4.9. In this figure, a corrugation length corresponds to $\approx 30\rho_\mathrm{s}$. The edges of the islands produced by the RMPs are less well-defined, which makes identifying a precise island width challenging. For the purposes of this discussion, an island width refers to maximal radial excursion of a given field line, which extends beyond the clean island-like flux surfaces

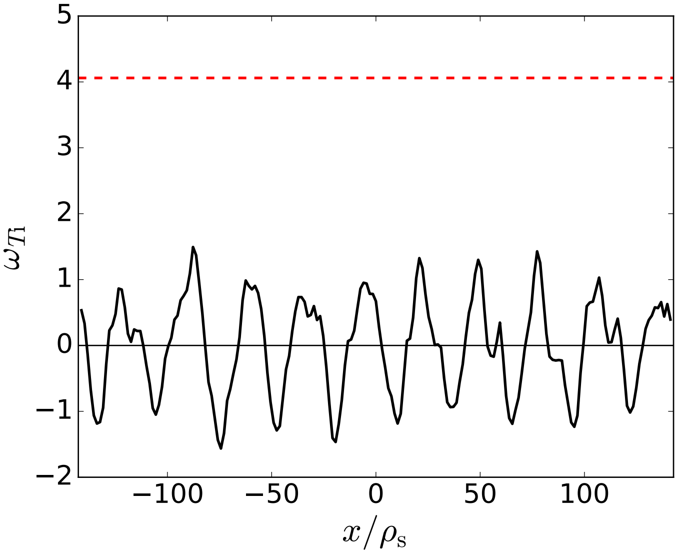

Figure 4.8: Example of a temperature profile corrugation take from a nonlinear DIII-D gyrokinetic simulation with an external $B_r/B_0 = 3.25 \times 10^{-4}$. Fluctuations in ion temperature gradient versus radial position exhibit periodic behavior (expected for flux tubes) and localization in the x direction. The dashed red line corresponds to equilibrium gradient, demonstrating that fluctuating gradients can be on the same order as the background.

but more accurately corresponds to the physically relevant scale length. When this island width is less than half a corrugation length, particles moving within that radial region will feel an increased turbulent drive due to the corrugation. However, once the island width exceeds approximately the half corrugation length, the average corrugation effect experienced by a particle moving within the island actually begins to decrease, until it vanishes entirely once the island width reaches a full corrugation length.

The non-monotonicity of the flux scaling with B_r (or island width) can plausibly be matched to this phenomenon. Figure 4.9 shows island structures overlaid on contours of turbulent temperature fluctuations for the RMP values that correspond to the first peak (left) and trough (right) in flux as shown in Fig. 4.6. Importantly, the corrugation length does not vary with RMP amplitude, but rather corresponds to the scale length set by the lowest finite k_x that is coupled to the $k_x = 0$ mode through the parallel boundary condition (see Chapter 2). The RMP island width corresponding to the first peak in transport is equal to approximately half the corrugation width, and thus the decrease in transport that comes with larger island widths is consistent with the above physical picture. Additionally, the island

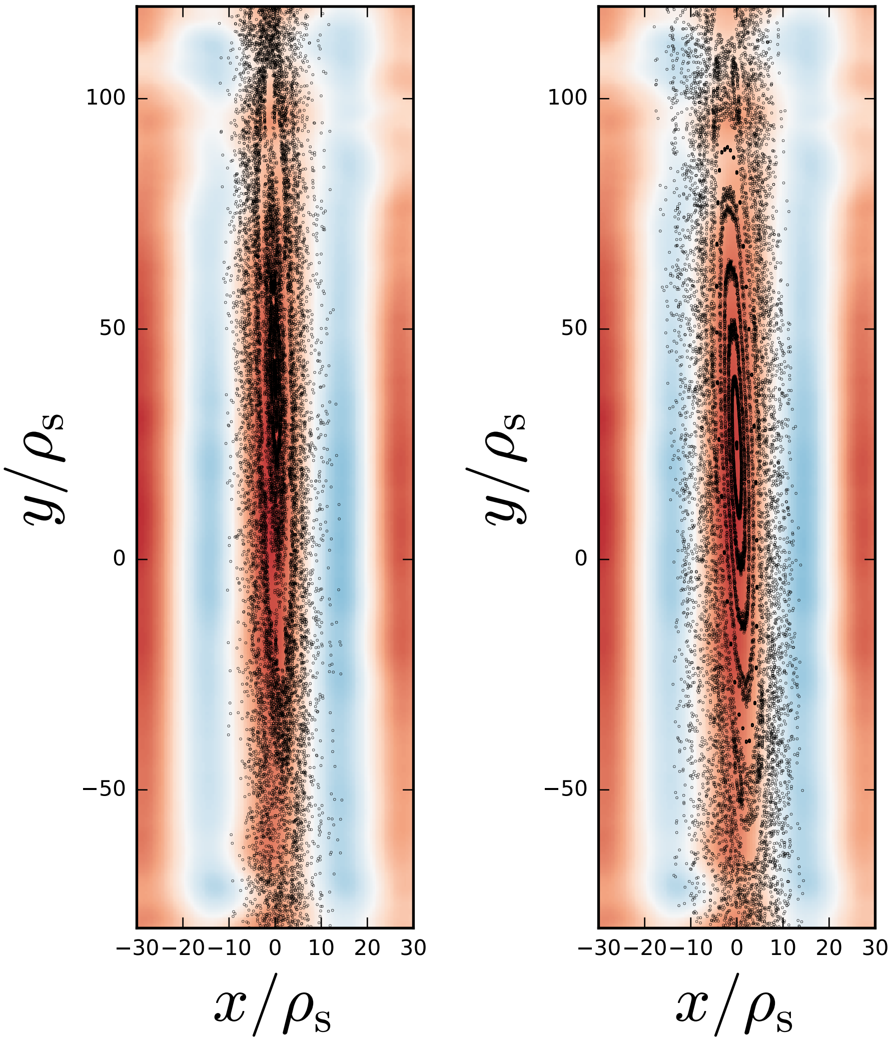

Figure 4.9: Poincaré plots of RMP island structure overlaid on contours of the time-averaged turbulent temperature gradient fluctuations for the RMP values corresponding to (left) the first peak in transport and (right) the trough. For the left, the RMP island width is approximately half a corrugation length, whereas on the right, the island width reaches a full corrugation length.

width corresponding to the trough in transport matches well with the full corrugation length. Beyond this point, island self-overlap begins to occur which greatly enhances the already present magnetic-flutter-induced zonal flow erosion, now much stronger than the effect of corrugations. It should be noted that this corrugation effect is clearly a consequence of using flux-tube simulations; one would not expect such behavior to be present in experimental observations, where profiles cannot be held constant.

With a better understanding of these phenomena in hand, the effect of the RMP on microturbulence levels is more directly examined. Fig. 4.10 plots density fluctuation spectra taken from simulations, focusing specifically on RMP strengths that result in magnetic diffusivity comparable to that seen in the experiment, see Fig. 4.7 for reference. In the experiment, even in the absence of an RMP, there still exists a small island at $\psi_n = 0.88$. As the existence of this island is suppressed by the artificially reduced β, the smallest imposed B_r/B_0 value in Fig. 4.10 serves as a proxy for this island, and the curves in the figure can be qualitatively matched to the curves of corresponding color in Fig. 4.4. Figure 4.10 shows the turbulence to increase with increasing RMP amplitude for a range of microinstability wavenumbers, qualitatively agreeing well with the BES measurements.

The density spectra exhibit interesting features outside of the microinstability wavenumber range for which fluctuations increase with RMP. Below $k_y = 0.1$, there are two peaks: one corresponding to the RMP applied at $k_y = 0.015$, and another peak at $k_y = 0.075$. The latter peak occurs at the largest scales for which ITG remains unstable (not shown in Fig. 4.5), and is nonlinearly suppressed by the RMP. At the high-k_y end of the spectrum, the increase in fluctuations with RMP is not observed. This is potentially attributed to a transition as seen in the linear instability spectrum from ITG to ∇T-TEM. It has been documented previously (Dannert and Jenko, 2005) that the dependence of ∇T-TEM turbulence on zonal flows is very weak. As such, one would not expect the fluctuations at wavenumbers for which ∇T-TEM dominates to change in response to zonal flow reduction, in contrast to fluctuations at ITG-dominanted wavenumbers (which depend strongly on zonal flows). It remains then to verify that the changes observed for the ITG-dominated wavenumber range correspond to zonal flow erosion in what follows.

These simulation results showing a range of microinstability fluctuations that vary directly with RMP amplitude, coupled with the BES observations, suggest strongly that RMPs have a significant effect on microturbulence. However, it is important to study what specific aspects of the RMP govern this effect, and whether or not it can be directly connected to the previously discussed zonal flow erosion mechanism, or if the RMPs are increasing turbulence

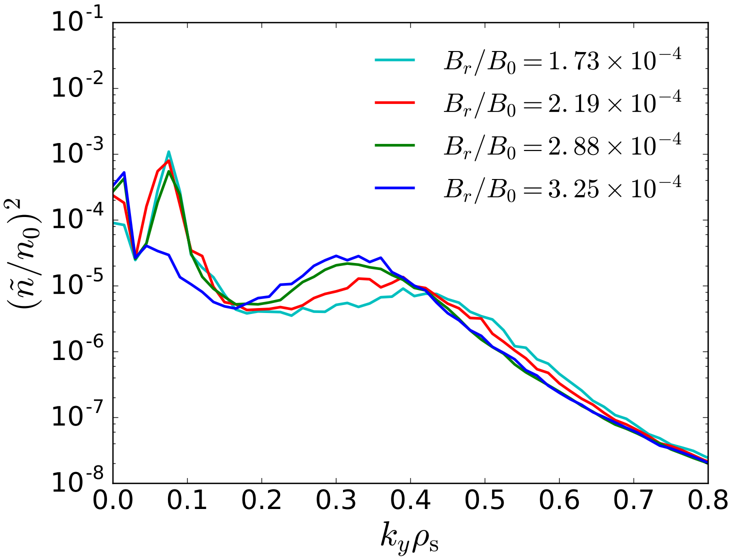

Figure 4.10: Density fluctuation amplitude vs. wavenumber. For a range of microinstability wavenumbers, the spectral amplitudes increase commensurately with RMP strength, in qualitative agreement with Fig. 4.4.

levels through a different process. The $k_y = 0$ Fourier component of the electrostatic potential (i.e., the zonal flow) is plotted versus time in Fig. 4.11. At $t = 1730a/c_s$, when the RMP is applied, there is a distinct drop in the zonal flow amplitude, and the zonal flow establishes a saturated value lower than before applying the RMP. Combined with the previous results of turbulence levels increasing with RMP strength, this points very strongly to DIII-D exemplifying another regime in which this multi-scale interaction between large-scale magnetics and zonal-flow-mediated microturbulence is significant.

Previous studies (Holod et al., 2017) examining the effect of RMPs on microturbulence in DIII-D noted that there was no discernible effect, seemingly in stark contrast to the results just presented. However, in that work, the RMP was applied in such a way that flux surfaces were shifted, but the RMP did not produce a change in the magnetic topology, referred to in that work as an ‘ideal MHD kink response’. To compare the results of that work to the physics discussion of this chapter, the identical procedure detailed above for studying RMP effects was performed, but changing the RMP structure such that it has odd parity in the field-line-following coordinate z instead of even. This is not to be confused with the RMP coil parity on the DIII-D experiment, for which the terms “odd” and “even” are used with a separate meaning. Physically, this corresponds to perturbations that break flux surfaces

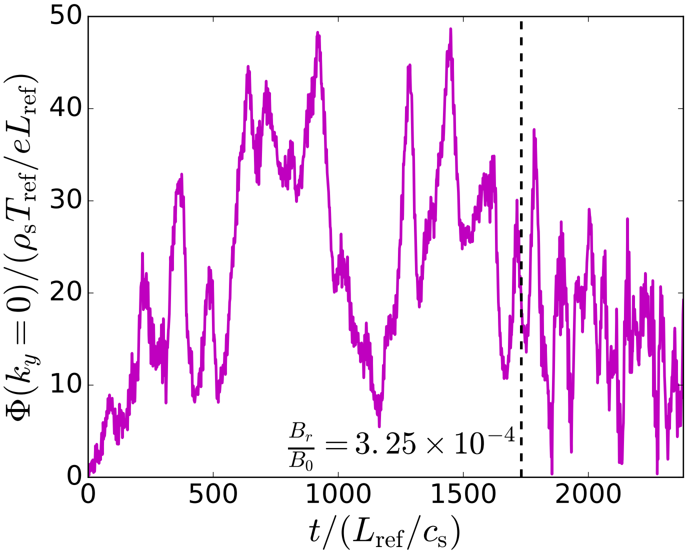

Figure 4.11: Time trace of the $k_y = 0$ electrostatic potential. At $t = 1730$, the RMP is turned on, at which time the zonal flow amplitude drops and establishes a lower saturated value. This is consistent with the physical picture of zonal flow reduction via magnetic flutter.

(even z parity, or tearing-like) versus those that simply shift the surface (odd z parity, or kink-like). This was implemented by applying an $A_\parallel \propto ze^{-z^2}$ (in contrast to the $A_\parallel \propto e^{-z^2}$) as a continuation to the simulation without an applied RMP. As demonstrated in Fig. 4.12, this odd parity RMP has no appreciable effect on the density fluctuation spectra (aside from a slight narrowing of the low-k_y ITG peak), though the B_r magnitude is comparable to largest B_r value in Fig. 4.10. As zonal flows follow flux surfaces, particles streaming along a perturbation that shifts flux surfaces rather than breaking them would not traverse regions of different electrostatic potential, so one does not expect the magnetic-flutter-induced "shorting out" of zonal flows (discussed in Chapter 2) to occur here. In light of this, the results of this chapter are not at odds with those presented in (Holod et al., 2017), but rather serve to further confirm the role of magnetic flutter in reducing zonal flows.

4.3 Chapter Summary

This chapter presented a combined experimental and computational study of the inherently multi-scale effect of RMPs on zonal flows and microturbulence levels in the DIII-D tokamak. In order to draw connections to tearing modes and microturbulence on the RFP from

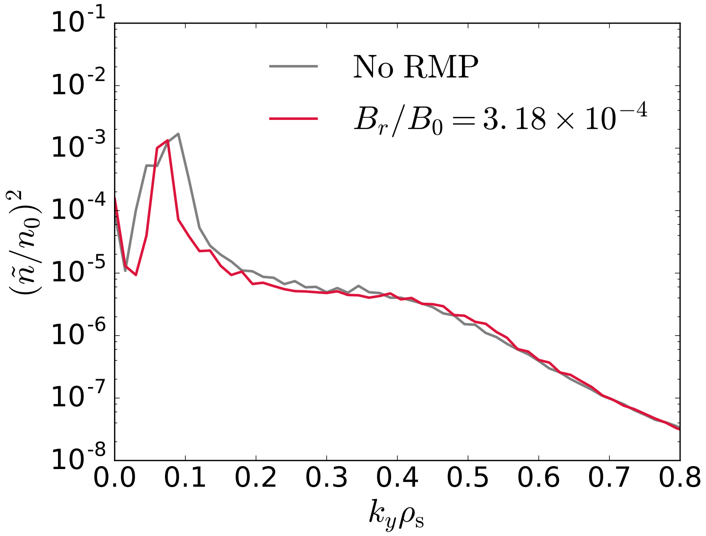

Figure 4.12: Density fluctuation amplitude vs. wavenumber, comparing spectra in the case with without any applied RMP (gray) with the case that has that has an odd-parity, kink-like RMP (crimson) of comparable B_r amplitude to the tearing-parity studies. The addition of the odd-parity RMP does not produce a significant difference in the density fluctuation.

Chapter 3, large-scale magnetic fluctuations were sourced via a tunable RMP amplitude. Experimental measurements of density fluctuations using BES reveal a direct increase in fluctuation signal at microturbulent frequencies with RMP amplitude, suggestive of this same magnetic fluctuation-zonal flow-microturbulence interplay. Gyrokinetic simulations were used to more thoroughly characterize the governing physics in this discharge. Non-monotonic scaling of turbulence levels were observed, at odds with expectations set by the previous work on MST; this apparent discrepancy was addressed and explained via profile corrugations. In the simulations, density fluctuation spectra were seen to increase with increasing RMP amplitude for a range of microinstability wavenumbers, in qualitative agreement with the experiment. This increase in microturbulent activity is concurrent with a marked drop in zonal flow levels, indicating the same sort of magnetic-flutter zonal flow erosion dynamics that were observed for MST simulations are present in DIII-D. As an additional confirmation of this, the structure of the RMP was also seen to play a significant role, such that flux-surface-breaking is required for an observable effect on transport. While RMPs will continue to be a vital part of tokamak confinement efforts through ELM suppression, the additional impacts that RMPs have on plasma dynamics, such as in this chapter with increasing microturbulence and transport, should be taken into consideration.

5 MULTI-SCALE INTERACTIONS OF TEARING MODES AND MICROTURBULENCE

The results discussed in Chapters 3 and 4 clearly demonstrate the importance of interactions between ion-scale and MHD-scale dynamics, specifically as they manifest in some toroidal fusion plasma configurations. As previously discussed, the large-scale magnetic fluctuation effects were modeled via the inclusion of a constant-in-time $A_\parallel$ perturbation implemented at the largest spatial scale of the simulation domain. While this implementation is an accurate reflection of how the RMP appears in DIII-D plasmas, this approach is somewhat limited in describing all of the physics present in the tearing-mode-microturbulence interactions present in the RFP. In Chapter 3, the simulation domain was limited to microturbulent scales, and thus was not representing truly multi-scale interaction physics but rather modeling how small scale magnetic fluctuations (that could in principle be driven by the large tearing modes) alter the microturbulence. Additionally, tearing mode magnetic fluctuations in the RFP are not driven by contant-in-time external sources, but are an unstable normal mode drive by current gradients of the plasma equilibrium state. A physically realistic description would thus account for current gradient-driven global instability within the model equations, allowing not only the tearing fluctuations to modify properties of microturbulence, but also for the microturbulence to modify the large-scale magnetic fluctuations. Experimental measurements of power fluctuations in standard MST plasmas (Thuecks et al., 2017) points to the coexistence of large-scale tearing modes and small-scale microturbulence. As evident in Fig. 5.1, the partition of energy between kinetic and magnetic channels shows an existence of high-frequency, non-Alfvénic modes, as Alfvénic modes distribute energy equally between kinetic and magnetic channels. These high-frequency, kinetically-dominated modes are concurrent with tearing modes at low frequencies.

A large body of theoretical work (Scott et al., 1985; Fitzpatrick, 1995; McDevitt and Diamond, 2006) has included current gradients in models to study multi-scale interactions between tearing modes/islands and microturbulence. As examples: (Hornsby et al., 2015) observe using the gyrokinetic code GKW that islands can drive microinstabilities near the separatrix, which in turn serve to stochasticize the island structure. (Ishizawa and Nakajima, 2007) observe that a turbulent state characterized by a balance between zonal flows and microturbulence can be destabilized by the formation of tearing mode. However, within these works there are not any discussions of the important magnetic-flutter-induced zonal flow

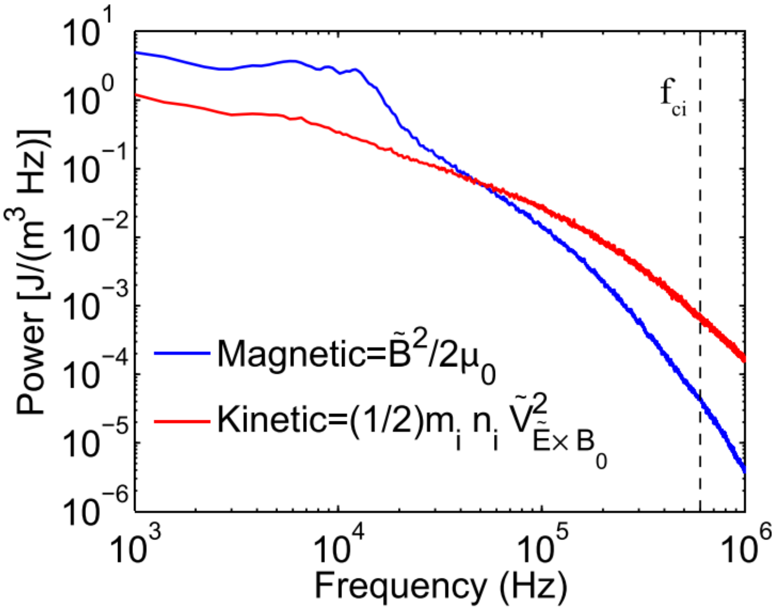

Figure 5.1: Experimental measurement of energy partition in standard MST plasmas. At low frequencies, tearing modes dominate the power spectrum. At high frequencies, a deviation from energy equipartition suggests the presence of high-frequency microinstabilities present concurrent with the tearing activity. Taken from (Thuecks et al., 2017).

erosion and its effect on transport levels. In the interest of studying that physics, as well as working towards a description that more accurately models RFP dynamics, the Gene equations are modified to include current gradient effects.

In this chapter, a modified gyrokinetic Vlasov equation is presented, and results thus obtained are benchmarked against existing analytic theory; importantly, all work in this chapter is based on a slab geometry and corresponds to the collisionless limit of tearing fluctuations, in which effects other than resistivity are responsible for the non-ideal physics associated with instability. The linear instability spectrum is then presented for the slab geometry with both a current gradient and a temperature gradient. Along with the expected tearing mode and a slab-ITG microinstability, an additional instability is observed in the system and characterized here. Nonlinear simulations are performed, defined by distinct separation in temporal and spatial dynamics between ITG and tearing modes, and by modifications to both regimes when compared to single-scale simulations.

5.1 Current Gradient Implementation

To model the effects of an equilibrium current gradient, the governing gyrokinetic equations employed in the Gene code as discussed in Chapter 2 are modified. The modifications take the following form:

$$\mathcal{L}_j \rightarrow \mathcal{L}_j + \partial_x G_{0j} \partial_y \chi_j - \partial_x \chi_0 \partial_y g_j \ , \tag{5.1}$$

where $\mathcal{L}_j$ is the unmodified linear gyrokinetic operator as defined in Chapter 2, G_{0j} is a modified shifted Maxwellian distribution function, and χ_0 is equilibrium vector potential that arises from the equilibrium current (see Appendix C). This approach is similar to the methods used in (Pueschel et al., 2011), which uses gyrokinetics to study reconnection. However, in that work the free energy for tearing modes is introduced via the initial condition (a current sheet) that evolves via the nonlinearity. As that free energy source is applied only at $t = 0$ and not sustained, any turbulence is inherently decaying. Additionally, that approach requires nonlinear simulations, and thus is unable to characterize the full spectrum of linear modes. Using the method described in this section results in a fixed source of free energy throughout the duration of simulation to drive turbulence, and allows for linear calculations of eigenmodes.

The quantities G_{0j} and χ_0 in Eq. 5.1 are defined as:

$$G_{0j} \equiv \frac{m_j}{2\pi T_{0j}} n_{0j} \mathrm{exp}\left[-\frac{(m_j/2)(v_\parallel - v_{\parallel,0}(x))^2 + \mu B_0)}{T_{0j}}\right] - \frac{q_j}{m_j c}\frac{\partial F_{0j}}{\partial v_\parallel} A_{\parallel,0} \tag{5.2}$$

$$\chi_0 \equiv -\frac{v_\parallel}{c} A_{\parallel,0} \ . \tag{5.3}$$

Note that G_{0j} is a modification of F_{0j} much in the same way that g_j is a modification of f_j (Eq. (2.11) in Chapter 2), and $A_{\parallel,0}$ is calculated from Ampére's law with current determined from the the $v_\parallel$ velocity space moment of the shifted Maxwellian distribution function. For all results discussed in this chapter, the radial variation of the velocity shift is sinusoidal, with $v_{\parallel,0} = v_0 \mathrm{cos}(k_{x,\mathrm{cs}} x)$, where $k_{x,\mathrm{cs}}$ is the wavenumber of the current sheet and the corresponding $B_{y,0}$ that it produces (see Fig. 5.2). From this radial velocity dependence comes the current gradient (the first new term in equation (5.1)), and necessarily a background current will produce a background vector potential (the second new term in equation (5.1)). These additions produce extra terms that are higher order in $\rho_{\mathrm{ref}}/L_{\mathrm{ref}}$ as well, which are neglected here to stay consistent with the orderings discussed in Chapter 2. While implemented in the

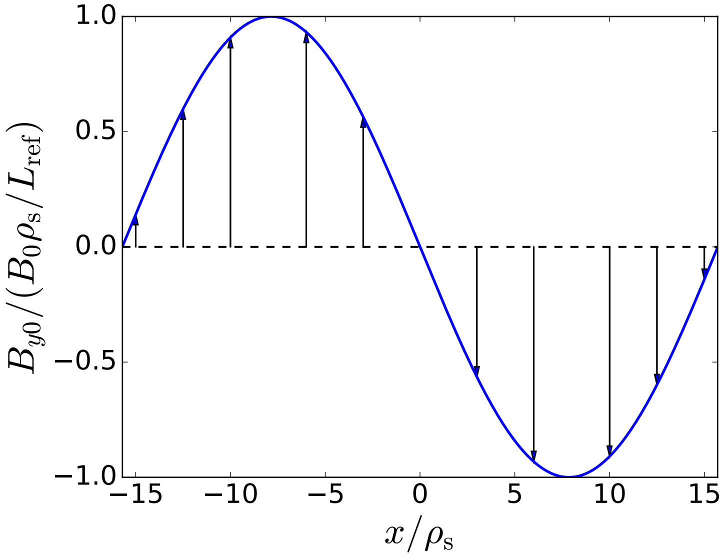

Figure 5.2: Radial variation of the added equilibrium $B_{y,0}$, which allows for tearing-unstable configurations. Note that the variation in $B_{y,0}$ (and thus the variation in the equilibrium current) is sinusoidal within the box, unlike other equilibrium gradients, which are taken as constant.

local flux-tube configuration, using this form means that the current gradient varies along x within the simulation domain, unlike the other equilibrium gradients, which are constant over the box length.

To test these modifications, benchmarking against an existing fluid model (Porcelli, 1991) was performed. As shown in Fig. 5.3, the modified linear operator in the GENE code agrees with existing analytic theory very well. For this benchmark, $k_{x,\mathrm{cs}} = 0.2$, $v_0 = 0.5c_\mathrm{s}$, $\beta = 0.3$, and $m_\mathrm{i}/m_\mathrm{e} = 25$; the scan over density gradient was performed at $k_y = 0.01$.

5.2 Instabilities of the New Linear Operator

Before running nonlinear simulations with the new current gradient, it is important to understand all of the linear instabilities present in the system that might contribute to the turbulent state. In order to investigate fundamental physics properties, the system studied for this chapter is a slab magnetic geometry. The inhomogeneities within the plasma consist only of a current gradient (to drive the tearing mode) and an ion temperature gradient (to drive slab-ITG microinstability). Relevant simulation parameters include: $\beta = 0.03$, $v_0/c_\mathrm{s} = 0.75$,

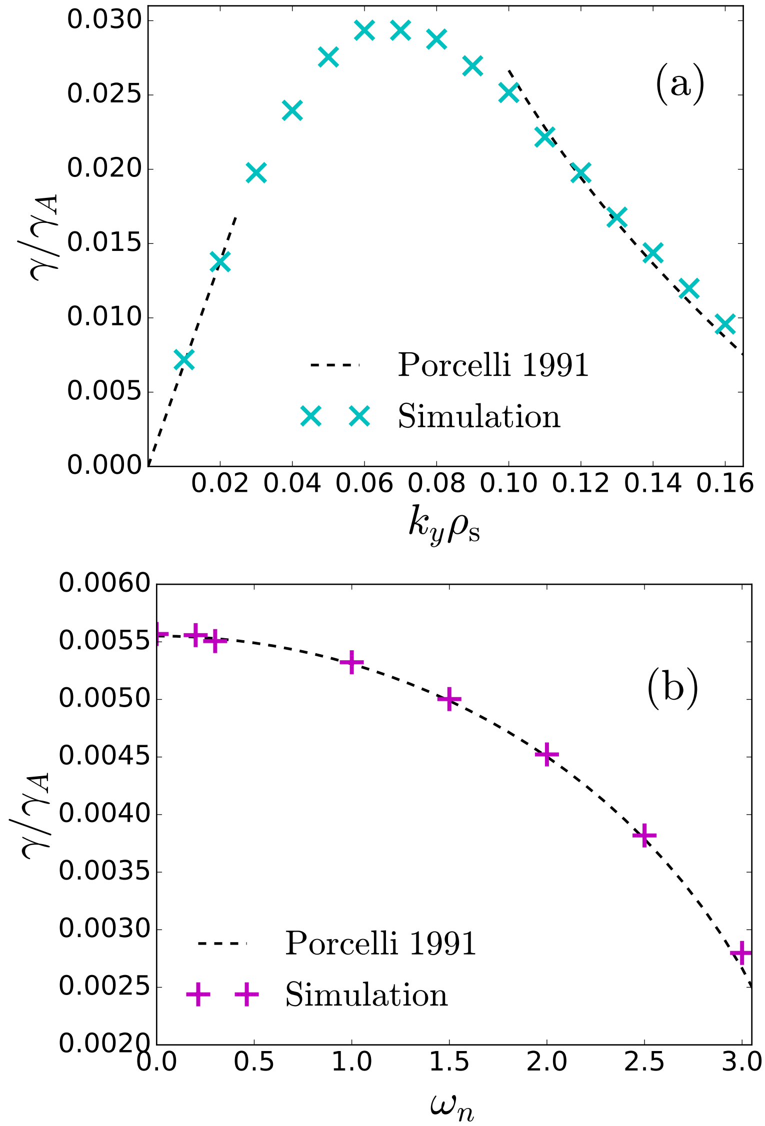

Figure 5.3: Benchmark of the current gradient implementation in the GENE code against a fluid theory for collisionless tearing modes; $\gamma_A \equiv \left(k_{x,\mathrm{cs}}B_{y0,\mathrm{max}}\sqrt{n_{e0}m_\mathrm{i}}\right)\left(\sqrt{2/\beta}\right)$. (a) Comparison of linear growth rates versus wavenumber; the analytic theory is plotted for the limits $k_y \to 0$ and $k_y \to k_{x,\mathrm{cs}}$. The code agrees very well with the theory in these limits. (b) Linear growth rate versus normalized density gradient; gyrokinetic simulations also match analytic theory very well in predicting diamagnetic stabilization of the tearing mode instability.

$k_{x,\mathrm{cs}} = 0.125$, $\omega_{T\mathrm{i}} = 10$, and $m_\mathrm{i}/m_\mathrm{e} = 100$ (reduced mass ratio used for more affordable computing costs).

As a prominent motivator behind this effort is to examine multi-scale interactions between tearing modes and microinstabilities, these parameters are chosen such that there is a distinct separation of spatial scales between the linear tearing mode activity and the ion-temperature-gradient mode activity. Shown in Fig. 5.4, using these parameters results in an instability spectrum across different scales, as desired. The black symbols correspond to simulations in which a single free-energy source is included and thus a single instability is present over a localized range of k_y. The circles at low $k_y\rho_\mathrm{s}$ correspond to purely growing tearing modes driven by a current gradient and temperature gradient; the squares at higher $k_y\rho_\mathrm{s}$ are a slab-ITG mode that is driven by an ion temperature gradient with no current gradient. The blue crosses and cyan triangles correspond to tearing modes and slab-ITG modes, respectively, for simulations in which both current gradient and ion temperature gradient are present. As expected, diamagnetic stabilization of the tearing modes is caused by the addition of the temperature gradient (evident by the slightly lower growth rates of the blue crosses compared to the black circles). In the higher-wavenumber end of the spectrum, a number of different k_z branches of the slab-ITG mode are excited in the case with the current gradient. The multiple peaks in the linear spectrum correspond to these different branches for which higher k_z modes appear at higher k_y, see Fig. 5.5. This is in contrast to the slab-ITG spectrum without the current gradient, in which a single k_z harmonic is dominant across all wavenumbers and the resultant spectrum varies smoothly. This difference is attributed to the small amount of magnetic shear introduced by the small $B_{y,0}$ produced by the current, as $k_z \propto \hat{s}k_y$.

Hybrid Drift-Tearing Mode

Along with the tearing and slab-ITG modes present at distinct spatial scales, the modified linear operator produces an additional instability that manifests at intermediate length scales and requires a finite gradient in both the current and ion temperature to exist. This mode is robust to convergence checks (including mass ratio in addition to the standard resolution checks) and thus not a numerical artifact. The instability has features that make it distinct from either the tearing mode or the slab-ITG mode, which are explored in this section; it will be hereafter referred to as the *hybrid drift-tearing mode*, not to be confused with the standard drift-tearing mode.

In examining linear instability from initial-value calculations, a smooth transition occurs in the dominant growth rates from the normal tearing instability to hybrid drift-tearing mode

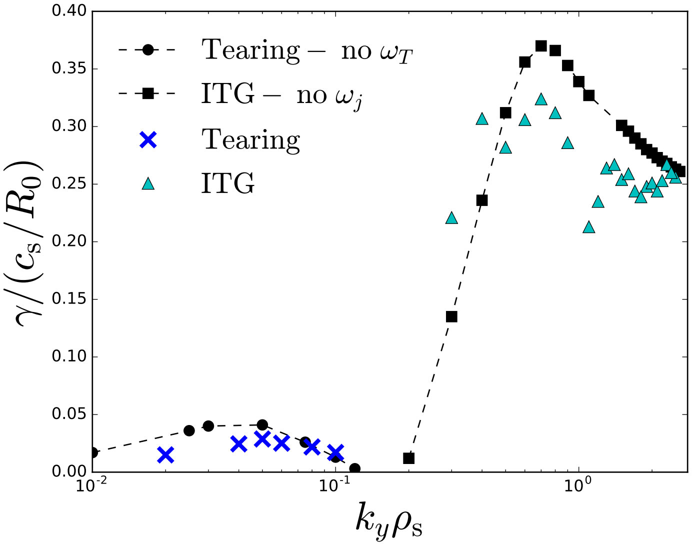

Figure 5.4: Linear growth rate versus wavenumber, comparing the instability spectrum in the case where there is only a current gradient (black circles), only an ion temperature gradient (black squares), and both current and temperature gradient (blue crosses and cyan triangles). Tearing modes and slab-ITG modes are present at separate scales. Tearing modes at low k_y are slightly stabilized by the temperature gradient, and the shear introduced by the current excites various k_z branches of the slab-ITG mode.

at $k_y = 0.06$, refer to Fig. 5.6 (the tearing mode growth rates for $k_y \geq 0.06$ were obtained using the GENE eigenvalue solver). Two key features differentiate this mode from the tearing mode at those low wavenumbers: 1) the instability continues to grow rather than decay as k_y approaches $k_{x,\mathrm{cs}}$, and 2) while the growth rate varies smoothly in transition from tearing mode into the hybrid drift-tearing mode, there is a marked increase in the real frequency over the transition. The current layer developed from the shifted-Maxwellian equilibrium appears to play an important role in the radial structure of this instability, similar to the tearing mode. Also, like the tearing mode, the hybrid drift-tearing mode is two-dimensional, not exhibiting any features in the z direction or showing any difference between 2D and 3D simulations. In that way, it differs importantly from the slab-ITG mode. The hybrid drift-tearing mode persists well into the microinstability wavenumber range, at which point there coexist a number of different modes, both the hybrid drift-tearing mode, which has two flavors as described below, and various k_z branches of the slab-ITG. While all of these modes are unstable they are subdominant to the slab-ITG and not plotted in Fig. 5.6 to maintain clarity.

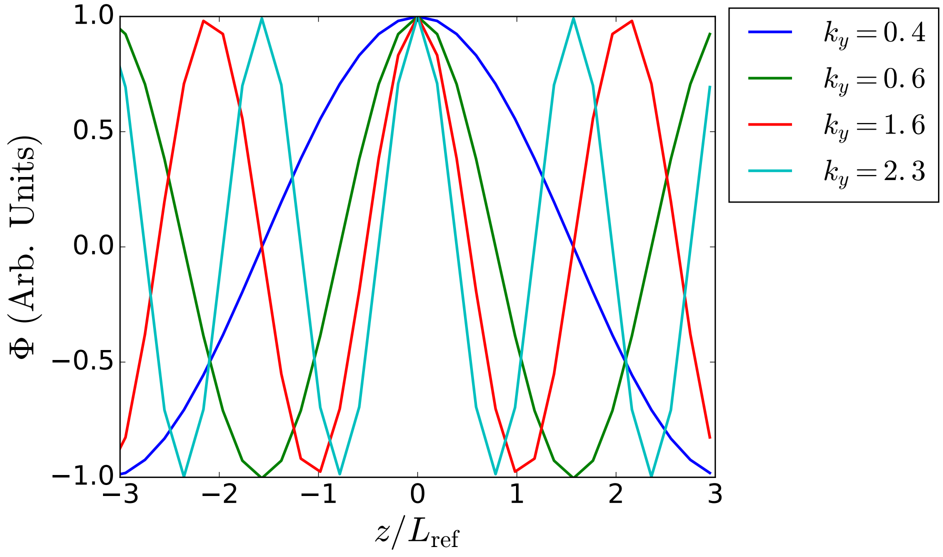

Figure 5.5: Electrostatic potential mode structure for the different k_z branches of the slab ITG mode present in the linear instability spectrum. As k_y increases, higher k_z harmonics take over as the most dominant instabilities, contrasting the case without a current gradient in which there is one dominant k_z branch across the whole spectrum.

The hybrid drift-tearing mode exists in two flavors of distinct x-parity, depending on whether the mode wavenumber k_y is greater or less than $k_{x,\mathrm{cs}}$. For $k_y < k_{x,\mathrm{cs}}$, the mode structure is tearing parity (where $A_\parallel$ is even, Φ is odd) in the x direction much like the tearing mode, whereas the parity switches to ballooning ($A_\parallel$ and Φ switch parity) for $k_y > k_{x,\mathrm{cs}}$. As evident in Fig. 5.7, both parity versions of this mode exhibit the same parametric dependencies. This, combined with the fact that growth rate and frequencies vary smoothly across the $k_y = k_{x,\mathrm{cs}}$ boundary, suggests that the two different parities are branches of the same mode. The extent to which those modes contribute to the turbulent state compared to the tearing and slab ITG modes will be discussed in the next section.

5.3 Turbulence in the Tearing-Slab-ITG System

Nonlinear simulations of this slab system with both ion temperature and current gradient are performed to analyze the how cross-scale interactions modify the turbulence when the magnetic fluctuations are driven self-consistently from the plasma equilibrium. These simulations use the same parameters as discussed in the previous section, with $k_{y,\mathrm{min}} = 0.025$ and 128 k_y

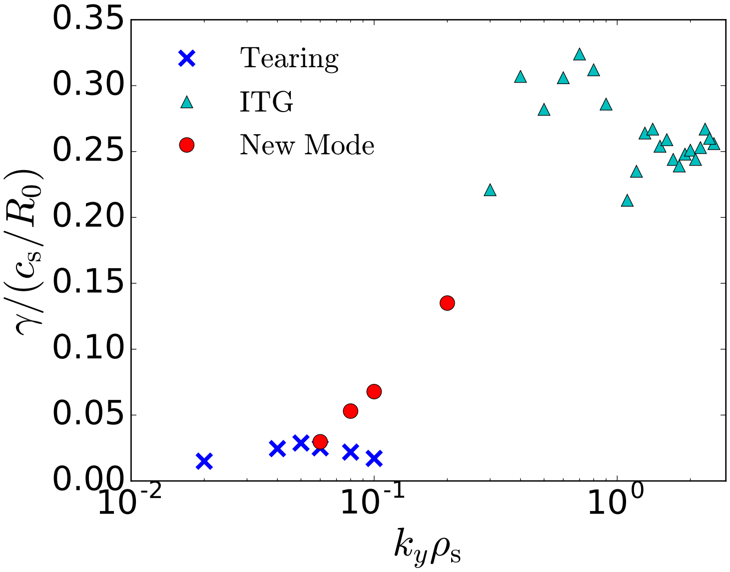

Figure 5.6: A more complete picture of the instability spectrum from Fig. 5.4 with a linear operator that contains both a current and temperature gradient, showing the presence of the hybrid drift-tearing mode arising at intermediate spatial scales. This instability continues into ion scales, at which there are a number of unstable modes. Only the most unstable slab-ITG is shown here in that wavenumber range.

modes utilized to resolve both tearing-mode and slab-ITG scales. Figure 5.8 depicts the time evolution of the electrostatic and electromagnetic components of the heat flux, from which direct consequences of the multi-scale turbulence are observed. The simulation exhibits three distinct states of “quasi-stationary” turbulence, defined here via the time intervals of $t = 35 - 50$, $t = 75 - 115$, and $t = 215 - 270$.

For the first interval, the transport is almost entirely electrostatic. In the second interval, the system is still primarily electrostatic, but there is a marked increase in electromagnetic activity. An examination of the zonal flow time trace in these first two intervals, shown as a dashed black line in the subfigure, reveals significant physics in response to this increased electromagnetic nature. During the first interval, the initial saturation of the turbulence occurs, during which zonal flows are growing further. However, as the turbulence increases and establishes a new, increased level in the second interval, the zonal flow then drops significantly, contrasting the previous interval in which it was driven. This drop coincides with more electromagnetic activity, which rises in the transition from the first to the second interval. This rise, occurring from $t \approx 40 - 60$, happens at a growth rate of approximately

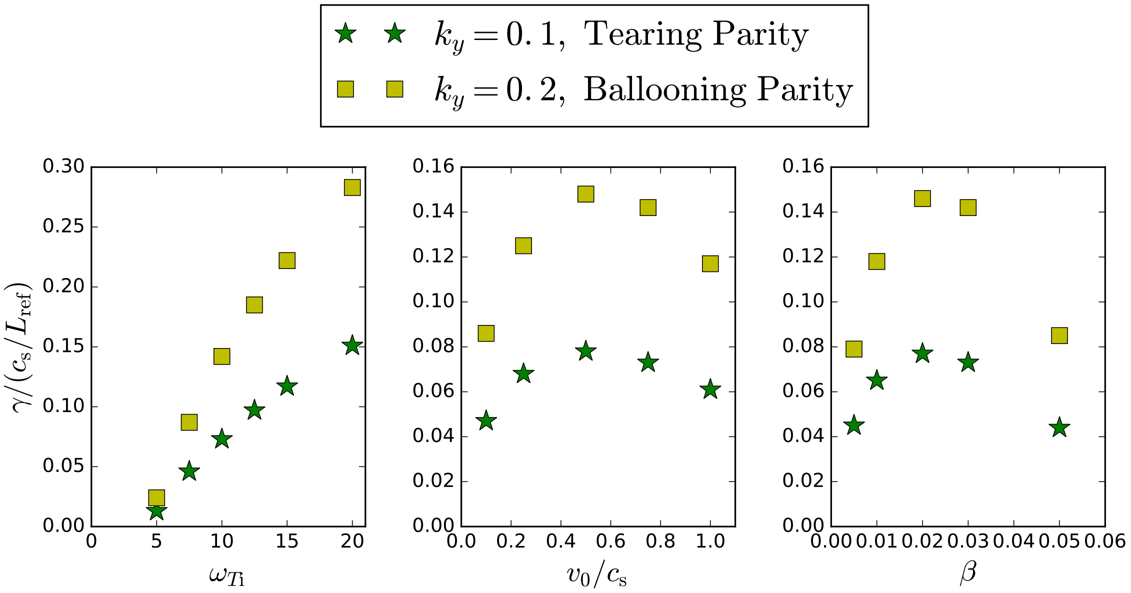

Figure 5.7: Growth rate dependence of the hybrid drift-tearing mode on ion temperature gradient, equilibrium velocity (current), and plasma pressure for both parities of the mode. The mode has the same dependencies on these parameters both in the tearing- and ballooning-parity flavors.

twice the maximum linear growth rate of the tearing mode. The phenomenon matches closely what one would expect from magnetic-flutter-induced zonal-flow decay, marking another system in which this effect comes into play. In contrast to other systems, however, the zonal flow reduction is not followed by increased transport levels. This is likely attributable to the driving instability for electrostatic turbulence in this system being slab-ITG. As discussed in Chapter 3, slab-ITG is less reliant upon zonal flows for saturation, which suggests that one could expect a similar lack in sensitivity to zonal flows from the slab-ITG in this interval. Beyond the second interval, the tearing instability begins to dominate the system and turns over around $t \approx 215$.

Figure 5.8 effectively shows a separation of temporal dynamics, in which early times have faster electrostatic modes dominating and later times have slower electromagnetic mode effects. In order to characterize the separation of spatial dynamics as well, heat flux spectra are calculated from time averages over each interval, see Fig. 5.9. Electrostatic and electromagnetic components of the ion heat flux spectra are plotted for each interval. For the first interval, the flux is localized to the spatial scales at which the slab-ITG is unstable.

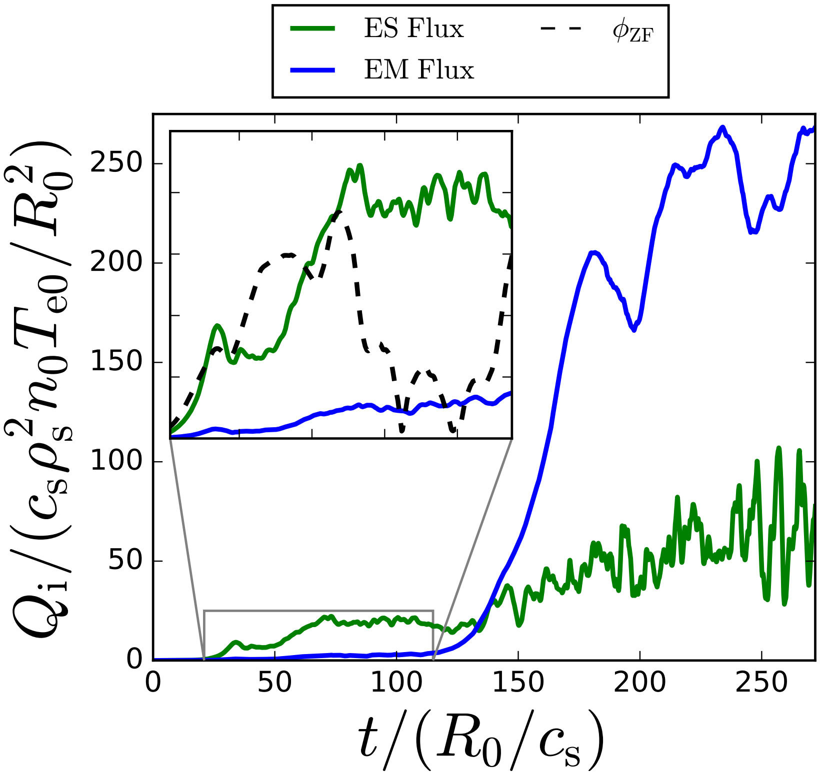

Figure 5.8: Time trace of the ion heat flux (green for electrostatic, blue for electromagnetic) for the slab system unstable to ITG and tearing modes (as well as the hybrid drift-tearing mode). There are three distinct quasi-stationary phases; the first two are electrostatically dominated, and the final phase is primarily electromagnetic. Zonal flow decay commensurate with increasing electromagnetic activity can be observed during the electrostatic turbulence (dashed black line), consistent with the previously-discussed magnetic-flutter-induced zonal flow erosion seen in earlier chapters.

While the additional hybrid drift-tearing mode is unstable at these wavenumbers as well, the fact that the spectrum drops off rapidly below the slab-ITG wavenumbers where the hybrid drift-tearing mode is still unstable suggests that the ITG mode is the dominant contributor to the turbulence during this phase. Transitioning to the second interval, the spectral peak shifts to lower wavenumbers and becomes wider; this suggests that the hybrid drift-tearing mode contributes more significantly to this intermediate interval.

For the third interval, the electromagnetic flux has become dominant, and the peak has shifted down to the tearing-unstable wavenumbers, specifically to where the tearing growth rate peaks. This state of electromagnetic turbulence is reminiscent of Fig. 5.1 from (Thuecks et al., 2017), in which experimental observations of fluctuation power spectra on the MST are dominated by magnetic energy at low frequencies and kinetic energy at higher frequencies. Contrasting this with the expectations of a pure MHD equipartition suggested the presence of microturbulence in the MST, even in standard operation without the increased gradients of PPCD. This lack of energy equipartition has also been noted in astrophysical plasmas (Boldyrev et al., 2011). One can see in these simulations that indeed a combined tearing- and micro-unstable system will produce such spectra. This multi-scale manifestation can also be observed in the transport cross phase α, which is defined for two fluctuating quantities A and B from the relation:

$$\langle AB \rangle = |A||B| \sin\alpha \ , \tag{5.4}$$

and serves as a measure for how much fluctuations at a given wavenumber can contribute to transport for a given turbulence amplitude. For electrostatic heat transport (cf. Eq. (1.20)), $A = \Phi$ and $B = T$; for electromagnetic flux $A = q_{\parallel}$ and $B = A_{\parallel}$. It is evident from Eq. (5.4) that maximal contributions to outward transport occur at $\alpha = \pi/2$, and maximal contributions to inward transport (or pinch) at $\alpha = -\pi/2$ (phases of $\alpha = 0$ or π means no contribution to transport). Cross phases for each time interval are shown in Fig. 5.10. For the first two periods, the cross phase for electrostatic transport resides near $\pi/2$, while for the electromagnetic transport it is close to π. Additionally, both transport channels exhibit a peak in phase at microturbulent wavenumbers, which shifts downward for the second interval; this is consistent with the flux spectra. For the electromagnetic interval, the $\langle q_{\parallel,\mathrm{i}} A_{\parallel} \rangle$ cross phase has shifted closer towards $\pi/2$ and down into the tearing instability range.

It is of interest to examine how this simulation containing both tearing and slab-ITG at distinct spatial scales compares to single-scale simulations of ITG microturbulence or tearing mode turbulence that resolve only their respective scales. Studying first how the slab-ITG

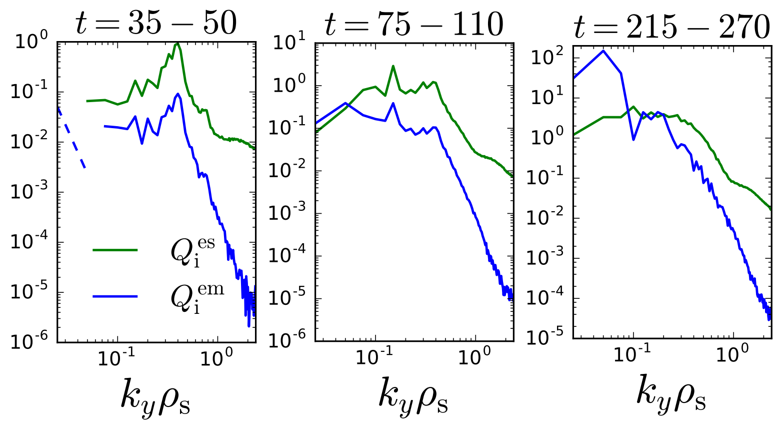

Figure 5.9: Ion flux spectra for both electrostatic (green) and electromagnetic (blue) channels; dashed line corresponds to inward (negative) flux. Early stages of the turbulences are governed primarily by slab-ITG physics. As the simulation progresses, the turbulence gradually shifts towards being more electromagnetic and larger-scale.

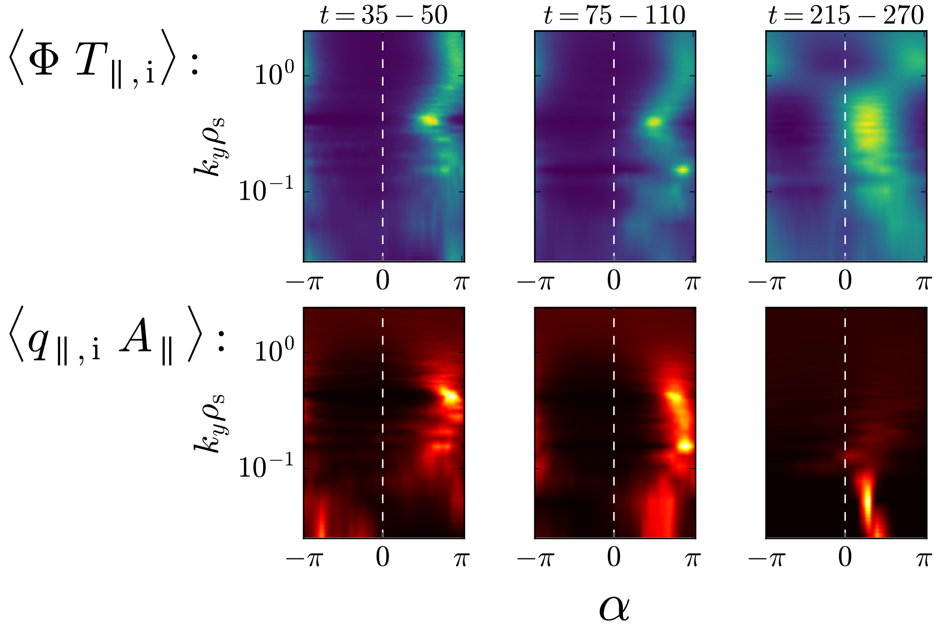

Figure 5.10: Cross phases for heat transport at each time interval discussed in the text. The phases show the same behavior with regards to small scales dominant early on and to the transition to larger scales at later times. Additionally, the shift of the phase for the electromagnetic term away from π at later times indicates an increased role in transport.

turbulence is modified by multi-scale effects, a nonlinear simulation without an equilibrium current gradient including only ion scales ($k_{y,\mathrm{min}} = 0.1$, 48 k_y modes) but the same ion temperature gradient is performed. Figure 5.11 shows the time trace of electrostatic ion heat flux for both the full multi-scale system with both tearing and ITG instability resolved at different scales and for a system that is only ITG unstable. The time window is chosen to compare the ITG-only case with the first interval of the multi-scale simulations in which the turbulence is localized primarily to the slab-ITG scales (as was discussed with Fig. 5.9). The ITG-only case reaches a saturated turbulence level within this time window, and does not vary from this quasistationary state at later times.

As evident from both Fig. 5.4 and comparing the linear growth phases of Fig. 5.11, the instability growth rates are larger for the system with only an ion temperature gradient. It is often assumed that flux levels scale directly with peak linear growth rate; one might predict for this reason that the transport levels for the ITG-only system would be larger than the electrostatic transport in the multi-scale system. However, this is clearly not the case, for even the lowest transport level of the multi-scale system significantly exceeds that of the ITG system. While this difference in transport level cannot be directly attributed to zonal flow reduction (which does not happen until the second interval of the multi-scale simulation, and as discussed likely does not directly affect slab-ITG saturation), this demonstrates that there are cross-scale dynamical effects that drive the transport higher than expectations set by linear or quasilinear physics. It should be noted that the zonal flow reduction observed in the multi-scale simulation does not occur in the single-scale slab ITG turbulence, consistent with the necessity of electromagnetic activity for zonal flow erosion.

In addition to studying how tearing effects modify the ITG-only turbulence, the reverse is also studied. To model turbulence and transport for a tearing-unstable system, both current and temperature gradients are retained (unlike the ITG-only case which did not include the current gradient). Heat fluxes in GENE are calculated utilizing averages in the x direction, and as such the periodic current gradient produces zero transport upon x-average; for this reason the standard constant temperature gradient is also included. As previously mentioned, the tearing instability is entirely two-dimensional and is virtually unaffected by the addition of the z dimension in simulations. This contrasts with the slab-ITG, an inherently three-dimensional instability. Thus, 2D simulations are used to ensure complete modeling of all the tearing mode physics, while conveniently removing the ITG part despite the presence of $\omega_{T\mathrm{i}}$. The hybrid drift-tearing mode discussed also persists in two dimensions; quantifying to what extent it contributes to the turbulent state is an important question to

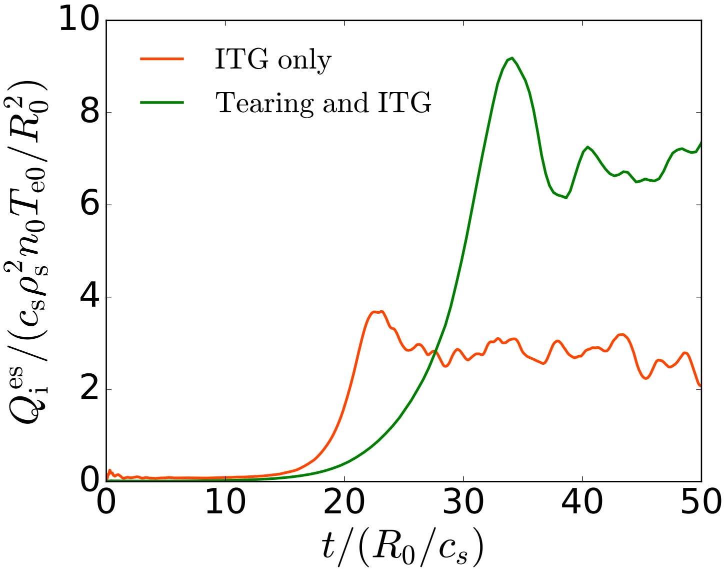

Figure 5.11: Comparison of electrostatic flux time traces for the multi-scale system (green) and the ITG-only system (orange). Despite larger linear growth rates in the latter, the saturated transport level is lower, suggesting the importance of cross-scale effects that allows turbulence to saturate at higher amplitudes, beyond those set linear or quasilinear expectations.

be addressed in future work. It is sufficient for the discussion here of comparisons to the combined tearing-slab-ITG system simulation that slab-ITG instability is not present.

These simulations again use the same physical parameters for the gradients, mass ratio, $k_{x,\mathrm{cs}}$, and β, and have $k_{y,\mathrm{min}} = 0.01$ with 48 k_y modes. A time trace of the electromagnetic heat transport is shown in Fig. 5.12. Similar to the result of comparison of ITG-only transport with the multi-scale case, there is here a modification of transport levels between the single-scale, 2D tearing simulation (which reaches a saturation $Q_\mathrm{i}^\mathrm{em} \approx 170$ shortly beyond the time window in Fig. 5.12) and the multi-scale. As both the tearing instability and the hybrid drift tearing mode gain no additional physics from 3D effects, this increase in transport level evident in the multi-scale is attributed to the presence of slab-ITG. Just as in the previous comparison, using growth rates alone to estimate relative differences in transport levels would not provide the correct scalings, further reinforcing the shortcomings of quasilinear concepts to inform transport physics when interactions between distinct scales are present.

The slab-ITG mode also appears to have a significant effect on the island structure. Figure 5.13 compares Poincaré plots between the two simulations, both taken from regimes of saturated electromagnetic turbulence. For the 2D simulation in which slab-ITG is not

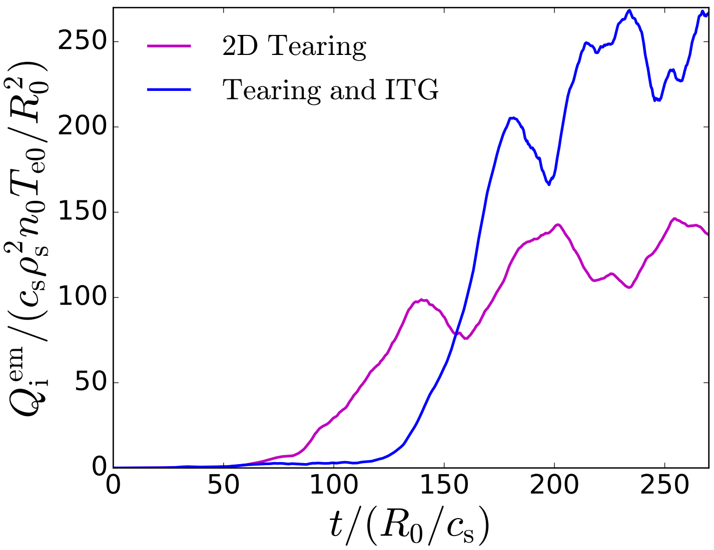

Figure 5.12: Comparison of electromagnetic flux time traces for the multi-scale system (blue) and the 2D tearing system (magenta). Similar to Fig. 5.11, linear growth rates are slightly higher for the single-scale simulation for $t < 120$, but cross-scale effects again result in transport larger than what quasilinear estimates would predict.

present, there are well-defined, distinct island structures with a k_y wavenumber corresponding approximately to the peak in linear growth rate and heat flux spectrum. However, the introduction of microinstability significantly stochastizes the magnetic field structure, resulting in a loss of coherent island region. A similar effect is seen in (Hornsby et al., 2015), in which increased gradients around island separatrices drive microinstabilities that produce field stochastization. It is possible that a similar phenomenon is occurring here; however, as evident from Fig. 5.13, the stochastization is not localized to the island boundary, but rather the entire magnetic field structure has become somehwat stochastic due to the microturbulence. This more stochastic structure can contribute to the larger electromagnetic transport seen in Fig. 5.12, as particles can traverse radial distances very rapidly along these wandering field lines.

It is worth mentioning the role that the hybrid drift-tearing mode might play in these analyses. An issue to address concerning the 2D tearing simulations with an ion temperature gradient regards how to distinguish between effects of slab-ITG from the hybrid drift-tearing mode, which does persist linearly out to ion-scale wavenumbers. In order to most effectively address this, one would ideally calculate the complete eigenspectrum for the linear operator

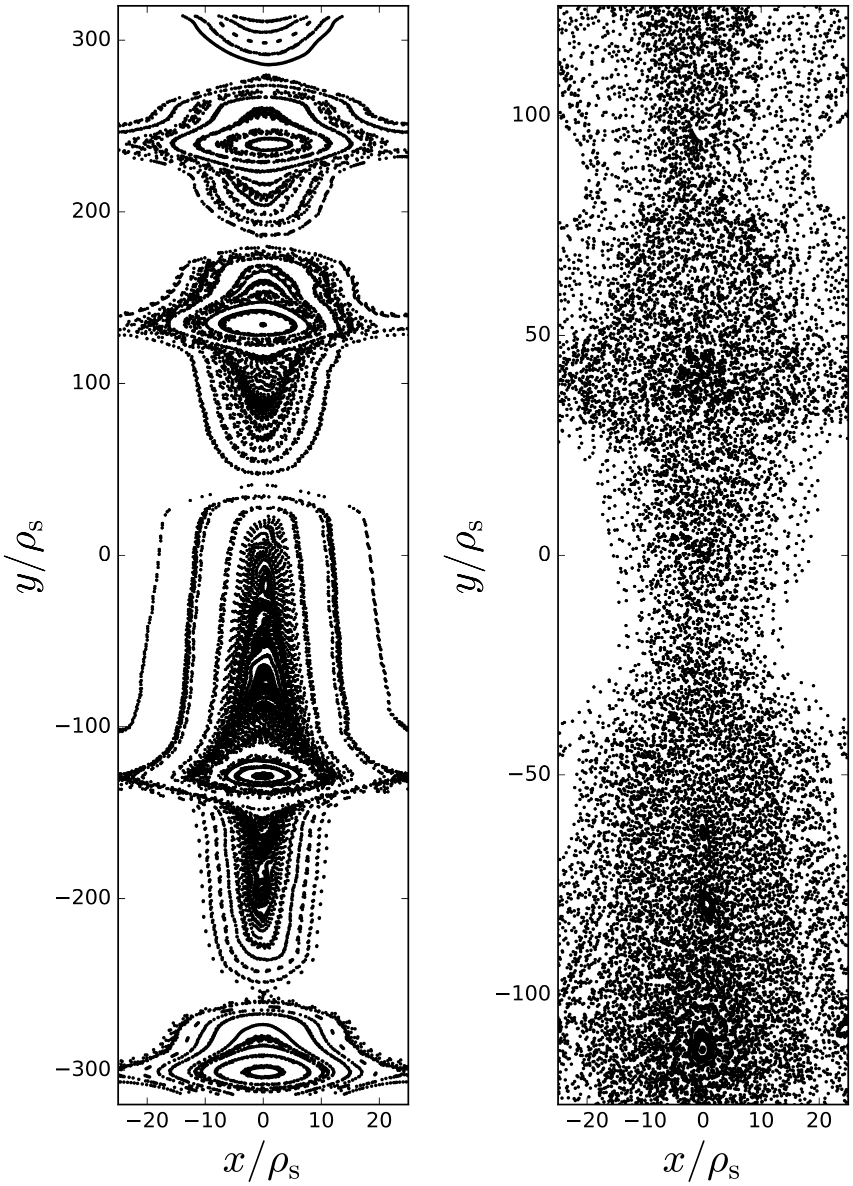

Figure 5.13: A comparison of magnetic island structure for (left) the single-scale, 2D tearing system and (right) the multi-scale, tearing+slab-ITG system. The tearing-only system exhibits separate well-defined island structure at the k_y approximately around where the linear growth rate and flux spectra peak. The multi-scale system exhibits a loss of coherent island structure, suggesting that the microturbulence serves to enhance magnetic stochasticity.

that has both a current and a temperature gradient and then use projections, as defined in (Pueschel et al., 2016; Fraser et al., 2018), to determine how much each different mode contributes to the overall saturated turbulent state. However, the rank of the discretized linear operator is so large for this system that a full calculation of all the eigenmodes is not tractable at this time. The results presented here do reflect the importance of the effect that high-k_y modes have on small-k_y tearing turbulence. Thus, in the interest of multi-scale physics investigations, whether the contributing high-k_y mode is slab-ITG or the hybrid drift-tearing mode (or likely, both) is of secondary importance.

5.4 Chapter Summary

In this chapter, multi-scale interactions between magnetic fluctuations and microturbulence were investigated through a slab system stripped of the geometric complexities that can arise in toroidal fusion configurations. The tearing modes were sourced via a new equilibrium current gradient drive term in the Gene code. Tearing mode instability at large scales and slab-ITG instability at small scales were found in a slab system with both an equilibrium ion temperature and current gradient. The combined gradients also produced a new mode which was characterized here. A nonlinear, multi-scale simulation exhibited dynamics at distinct spatial and temporal scales, with electrostatic ITG turbulence dominating early times and electromagnetic tearing turbulence dominating later in the simulation. Zonal flow decay as a response to electromagnetic effects was again seen for this system. However, zonal flows play a less important role in slab-ITG saturation, and so a corresponding increase in the electrostatic turbulence was not observed. Comparisons of this multi-scale simulation with single scale simulations at both large tearing scales and small ITG scales revealed significant effects of cross-scale interactions and the inability of simple linear or quasilinear estimates to inform multi-scale physics accurately.

6 MAGNETIC-DRIFT-DRIVEN COLLISIONLESS MICROTEARING

The primary focus of this thesis is the study of how interactions between large-scale magnetic activity and small-scale microturbulence affect turbulence and transport levels. This focus originates out of an interest in understanding specifically the dynamics governing RFP plasmas, as discussed thoroughly in chapter 3. In this chapter another physics phenomenon that is of particular relevance to the RFP configuration is explored: collisionless microtearing modes driven by magnetic drifts.

The microtearing instability is another drift-wave instability known to exist in various toroidal configurations, including the tokamak (Doerk et al., 2011; Hatch et al., 2016) and the RFP (Carmody et al., 2013; Predebon et al., 2010). It shares features with other microinstabilities discussed throughout this thesis, such as being driven by pressure gradients (specifically ∇T_{e}) and manifesting primarily at ion scales $k_y \sim 0.1 - 1$. It also differs significantly from these instabilities in that while TEM and ITG modes are electrostatic in nature, microtearing is an electromagnetic mode, meaning that it requires $A_\parallel$ fluctuations and can result in significant magnetic activity. Much like the macroscopic tearing mode, microtearing instability implies the existence of a current sheet layer, and is characterized by a Δ' parameter analogous to that used in standard tearing mode theory:

$$\Delta' \equiv \frac{1}{A_\parallel}\frac{\partial A_\parallel}{\partial x}\bigg|_{-d}^{d} , \tag{6.1}$$

where d is half the width of the perturbed current sheet in the x direction; note that this is distinct from the full width of the equilibrium current layer $a \gg d$. Integrating Ampère's Law over this current sheet layer, Δ' can be expressed in term of the parallel current density:

$$\frac{\partial^2 A_\parallel}{\partial x^2} = -\frac{4\pi}{c} J_\parallel \tag{6.2}$$

$$\frac{1}{A_\parallel}\frac{\partial A_\parallel}{\partial x}\bigg|_{-d}^{d} \equiv \Delta' = -\frac{4\pi}{c}\frac{1}{A_\parallel}\int_{-d}^{d} J_\parallel dx . \tag{6.3}$$

Equation (6.3) will be the basis for calculating the microtearing dispersion relation in this chapter. While Δ' has the same form as in the standard tearing mode, they differ importantly in free energy source. While the standard tearing mode draws energy from the relaxation of magnetic profiles, which restricts these modes to large spatial scales (Applegate et al., 2007), the microtearing mode relies upon the free energy in the electron temperature gradient (and is correspondingly not restricted to small wavenumbers). Traditionally, microtearing theory predicted that collisions in conjunction with temperature gradients were necessary for instability (Hazeltine et al., 1975). The basic mechanism is as follows: Consider electrons streaming along a magnetic field line. Upon introducing a radial field perturbation (and an associated $J_\parallel$ perturbation), electrons streaming along this radially perturbed line will sample regions of different collisionality due to the temperature gradient; regions of higher temperature will have lower collisionality, and lower temperature higher collisionality. This difference in collisionality results in a cumulative frictional force that drives additional current $J_\parallel$ along the field line, enhancing the original perturbation and thus producing instability.

Clearly, this physical picture would not produce instability in the absence of collisions. However, it has more recently been observed that for certain regimes, microtearing growth rates persist even in the limit of zero collisionality (Doerk et al., 2012; Predebon and Sattin, 2013; Swamy et al., 2014). There thus must be an additional physical mechanism by which the parallel current that produces microtearing is being reinforced. Several works have explored a variety of alternative driving mechanisms (Gladd et al., 1980; Cowley et al., 1986; Connor et al., 1990; Catto and Rosenbluth, 1981), but most still found microtearing to be stable without collisions. (Finn and Drake, 1984) established instability of a mode whose behavior matches the microtearing mode, driven unstable by magnetic curvature drifts. The gyrokinetic simulation results shown in (Predebon and Sattin, 2013) show that collisionless microtearing does indeed depend on magnetic curvature. Microtearing of this flavor would be significant for the RFP configuration, where the comparable B_θ and B_ϕ produce more magnetic field variation along the minor radius than seen in the tokamak, where it varies over the major radius, with correspondingly (order aspect ratio) larger curvature and ∇B drifts.

In what follows, a dispersion relation is derived describing how curvature and grad-B drifts modify linear microtearing instability. While this calculation is based on a drift-kinetic formulation, the observation of curvature-driven effects from a fluid model in (Finn and Drake, 1984) suggests that the kinetic nature of magnetic drifts in microtearing is less important and thus motivates an expansion in the magnetic drift resonance. The mathematical techniques used in this calculation are benchmarked against a well-established analytic theory for collisioness microtearing in the absence of magnetic drifts. The calculation indicates that the fluid expansion does not contribute to the instability, suggesting that the collisionless magnetic-drift-driven microtearing mode is inherently kinetic in nature.

6.1 Inclusion of Magnetic Drifts

The work in this chapter builds on prior work begun in (Carmody, 2014). To avoid redundancy, certain aspects of the calculation covered in the previous work will not be explicitly detailed but simply summarized. New aspects of the calculation will be explored in more detail. The non-adiabatic component of the perturbed drift-kinetic distribution function for electrons can be expressed as

$$g_{\mathrm{e}} = -\frac{eF_{\mathrm{M}}}{T_{\mathrm{e}}}\frac{\omega - \bar{\omega}_T^*}{\omega - k_\parallel v_\parallel - \bar{\omega}_D}\left(\Phi - \frac{v_\parallel A_\parallel}{c}\right) \, , \tag{6.4}$$

where e and T_{e} refer to the elementary charge and temperature, the equilibrium Maxwellian distribution function is given by $F_{\mathrm{M}} = \pi^{-3/2} n_0 v_{T\mathrm{e}}^{-3} \exp[-(v_\parallel^2 + v_\perp^2)/v_{T\mathrm{e}}^2]$, $v_{T\mathrm{e}}^2 = 2T_{\mathrm{e}}/m_{\mathrm{e}}$, ω is the mode frequency, $k_\parallel$ is the wavenumber parallel to the magnetic field, Φ is the electrostatic potential, $A_\parallel$ is the electromagnetic potential, and c is the speed of light. The driving gradients are found in $\bar{\omega}_T^* \equiv \omega_n + \omega_T\left(v_\parallel^2/v_{T\mathrm{e}}^2 + v_\perp^2/v_{T\mathrm{e}}^2 - \frac{3}{2}\right)$, and, importantly, the grad-B and curvature drifts are accounted for in $\bar{\omega}_D$, defined below:

$$\begin{aligned} \bar{\omega}_D \equiv \mathbf{v}_D \cdot \mathbf{k} = (\mathbf{v}_{\mathrm{c}} + \mathbf{v}_{\nabla B}) \cdot \mathbf{k} &= \left[\frac{v_\perp^2}{2\omega_{\mathrm{c}} B}\mathbf{b} \times \nabla B + \frac{v_\parallel^2}{\omega_{\mathrm{c}} B}\mathbf{b} \times \nabla B\right] \cdot \mathbf{k} \qquad (6.5) \\ &= \left[\frac{v_\perp^2 + 2v_\parallel^2}{2\omega_{\mathrm{c}} B}\mathbf{b} \times \nabla B\right] \cdot \mathbf{k} \equiv \omega_D \left(v_\parallel^2/v_{T\mathrm{e}} + v_\perp^2/2v_{T\mathrm{e}}\right) \quad . \qquad (6.6) \end{aligned}$$

A schematic process for deriving the dispersion relation is as follows: use the distribution function (see Eq. (6.4)) to calculate particle and current densities from velocity space moments, insert those quantities into the quasineutrality condition and Ampère's Law to get a closed set of equations, and solve for ω. The additional term $\bar{\omega}_D$ in the denominator introduced by the magnetic drifts makes the velocity space integrals analytically intractable, as it is a function of both $v_\perp^2$ and $v_\parallel^2$. The curvature-driven mode of (Finn and Drake, 1984) is derived from a fluid model, suggesting the possibility that magnetic-drift-related resonances are unimportant to this mode. The calculations in that work were not collisionless, so it is possible a different mode is being described in that fluid-like approach, but for the sake of analytic tractability, this assumption of negligible magnetic-drift resonance will be utilized here. This requires that $\bar{\omega}_D \ll \omega - k_\parallel v_\parallel$ from which one can expand:

$$\frac{1}{\omega - k_\parallel v_\parallel - \bar{\omega}_D} = \frac{1}{\omega - k_\parallel v_\parallel}\left(\frac{1}{1 - \frac{\bar{\omega}_D}{\omega - k_\parallel v_\parallel}}\right) \approx \frac{1}{\omega - k_\parallel v_\parallel}\left(1 + \frac{\bar{\omega}_D}{\omega - k_\parallel v_\parallel} + \cdots\right) . \tag{6.7}$$

Using this expansion, the distribution function can be written as

$$g_\mathrm{e} \approx -\frac{eF_\mathrm{M}}{T_\mathrm{e}}\left(\Phi - \frac{v_\parallel A_\parallel}{c}\right)\left(\frac{\omega - \bar{\omega}_T^*}{\omega - k_\parallel v_\parallel} + \frac{\bar{\omega}_D\left(\omega - \bar{\omega}_T^*\right)}{\left(\omega - k_\parallel v_\parallel\right)^2}\right) \equiv g_{\mathrm{e},0} + g_{\mathrm{e},\omega_D} . \tag{6.8}$$

6.2 Magnetic-Drift-Free Microtearing Dispersion

The density and current density obtained from the zeroth-order (in ω_D) distribution function $g_{\mathrm{e},0}$ correspond to the zero-magnetic-drift limit of the microtearing mode, described thoroughly in (Drake and Lee, 1977). To explicitly describe the mathematical techniques and processes used in this chapter and verify the accuracy of the approach, the collisionless dispersion relation from that work is rederived here using $g_{\mathrm{e},0}$. The calculation follows the schematic process outlined in the previous section, in which first the parallel current density is calculated from the distribution function:

$$J_{\parallel,e} = q_e \int v_\parallel g_e d^3\mathbf{v} , \tag{6.9}$$

$$J_{\parallel,0} = -e \int v_\parallel \left[-\frac{eF_M}{T_\mathrm{e}}\frac{\omega - \bar{\omega}_T^*}{\omega - k_\parallel v_\parallel}\left(\Phi - \frac{v_\parallel A_\parallel}{c}\right)\right] d^3\mathbf{v} . \tag{6.10}$$

The Maxwellian distribution is inserted, introducing the notation $v = v_\parallel / v_{Te}$ and $u = v_\perp / v_{Te}$ and evaluating the angular velocity dependence (for which the entire expression is constant):

$$J_{\parallel,0} = -e \int_0^\infty \int_{-\infty}^\infty 2\pi v_\perp v_\parallel \left[-\frac{e\pi^{-3/2} n_0 v_{Te}^{-3} e^{-(v^2+u^2)}}{T_\mathrm{e}}\frac{\omega - \bar{\omega}_T^*}{\omega - k_\parallel v_\parallel}\left(\Phi - \frac{v_\parallel A_\parallel}{c}\right)\right] dv_\parallel dv_\perp . \tag{6.11}$$

The definition of $\bar{\omega}_T^* \equiv \omega_n^* + \omega_T^*(v^2 + u^2 - \frac{3}{2})$ is written out, and the denominator expressed in terms of a newly defined variable $s \equiv \omega / k_\parallel v_{Te}$:

$$J_{\parallel,0} = \frac{2n_0 e^2}{k_\parallel T_\mathrm{e} \pi^{1/2}} \int_0^\infty \int_{-\infty}^\infty uve^{-v^2} e^{-u^2} \frac{\omega - \omega_n^* - \omega_T^*(v^2 + u^2 - \frac{3}{2})}{s - v}\left(\Phi - \frac{v_\parallel A_\parallel}{c}\right) dvdu . \tag{6.12}$$

As there are no resonances in $v_\perp$, evaluating the u integrals amount to taking moments of a Gaussian distribution:

$$J_{\parallel,0} = \frac{1}{2}\frac{2n_0e^2}{k_\parallel T_\mathrm{e}\pi^{1/2}}\int_{-\infty}^{\infty} ve^{-v^2}\frac{\omega-\omega_n^*-\omega_T^*(v^2-\frac{1}{2})}{s-v}\left(\Phi-\frac{v_{Te}vA_\parallel}{c}\right)dv\ . \qquad (6.13)$$

Collecting terms by their order in v, the integral can be expressed as a sum of derivatives of the plasma dispersion function, detailed in Appendix B.

$$J_{\parallel,0} = \frac{1}{2}\frac{2n_0e^2}{k_\parallel T_\mathrm{e}\pi^{1/2}}\left[\int_{-\infty}^{\infty} ve^{-v^2}\frac{(\omega-\omega_n^*+\frac{1}{2}\omega_T^*)-\omega_T^*v^2}{s-v}\Phi dv\right.$$
$$\left.-\int_{-\infty}^{\infty} v^2e^{-v^2}\left(\frac{(\omega-\omega_n^*+\frac{1}{2}\omega_T^*)-\omega_T^*v^2}{s-v}\right)\frac{v_{Te}A_\parallel}{c}dv\right]\ , \qquad (6.14)$$

$$J_{\parallel,0} = \frac{n_0e^2}{k_\parallel T_\mathrm{e}}\left[\left(\omega-\omega_n^*+\frac{1}{2}\omega_T^*\right)\left(\frac{1}{2}Z'(s)\right)-\omega_T^*\left(\frac{1}{4}Z'(s)-\frac{s}{4}Z''(s)\right)\Phi\right.$$
$$\left.-\left(\omega-\omega_n^*+\frac{1}{2}\omega_T^*\right)\left(\frac{s}{2}Z'(s)\right)\frac{v_{Te}A_\parallel}{c}-\omega_T^*\left(\frac{1}{4}sZ'(s)-\frac{1}{4}s^2Z''(s)\right)\frac{v_{Te}A_\parallel}{c}\right]. \qquad (6.15)$$

After some algebraic manipulations, as well as using the definition of the electron plasma frequency $n_0e^2/T_\mathrm{e} = 2\omega_\mathrm{pe}^2/4\pi v_{T\mathrm{e}}^2$ the resultant expression is

$$J_{\parallel,0} = \frac{2\omega_\mathrm{pe}^2}{4\pi v_{T\mathrm{e}}^2k_\parallel^2}\left(\frac{1}{2}(\omega-\omega_n^*)Z'(s)+\omega_T^*\frac{s}{4}Z''(s)\right)\left(k_\parallel\Phi-\frac{\omega A_\parallel}{c}\right)\ , \qquad (6.16)$$

which is the same as the current density derived in (Drake and Lee, 1977). For the most general form of a dispersion relation, one requires expressions for both Φ and $A_\parallel$ to close the set of equations. However, following (Drake and Lee, 1977) and in the interest of analytic tractability, the assumption is made that $\Phi \to 0$ for this calculation. Additionally gyrokinetic studies of microtearing have found it to persist in the absence of electrostatic potential fluctuations (Predebon and Sattin, 2013). In this case, only Ampère's Law is needed to close the system and solve for ω. Inserting Eq. (6.16) into Eq. (6.3) and setting $\Phi = 0$:

$$\Delta_0' = \frac{4\pi}{c}\frac{1}{A_\parallel}\int_{-d}^{d}\frac{2\omega_\mathrm{pe}^2}{4\pi v_{T\mathrm{e}}^2k_\parallel^2}\left(\frac{1}{2}(\omega-\omega_n^*)Z'(s)+\omega_T^*\frac{s}{4}Z''(s)\right)\frac{\omega A_\parallel}{c}dx\ . \qquad (6.17)$$

Before proceeding, one must account for the implicit x-dependencies present in Eq. (6.17). It is assumed that $A_\parallel$ is approximately constant over the perturbed current sheet layer, originally posited in (Furth et al., 1963). Also, this calculation utilizes the slab approximation, in which $k_\parallel = k_y x/L_s$, where L_s is the magnetic shear scale length. A consequence of this expression is that the argument s of the plasma dispersion function also depends on x, such that $s = (\omega L_s/k_y v_{T\mathrm{e}})(1/x)$, and $dx = -(\omega L_s/k_y v_{T\mathrm{e}})(1/s^2)ds$. Applying these definitions and simplifying:

$$\Delta_0' = -\frac{\omega_{\mathrm{pe}}^2}{c^2}\frac{L_s}{k_y v_{T\mathrm{e}}}\int \Big((\omega - \omega_n^*)Z'(s) + \omega_T^*\frac{s}{2}Z''(s)\Big)\, ds \ . \tag{6.18}$$

Careful consideration must be taken regarding the bounds of integration on s, a point at which the calculation presented here differs significantly from the previous attempt by (Carmody, 2014). In x-space, it is assumed that the current density peaks significantly within the perturbed layer and then drops off quickly, such that the integration bounds can be extended from $(-d, d)$ to $(-\infty, \infty)$ to a good approximation (a common practice for this type of calculation, cf. Eq. (31) of (Baalrud et al., 2018). When converting the integral to s, a discontinuity arises at $x = 0$, and so the integral must be split up into two parts: one covering from $(0_-, -\infty)$ (as x approaches zero from negative values) and $(\infty, 0_+)$. The second term in the integral of Eq. (6.18) can be integrated by parts, noting that $Z'(s) \propto 1/s^2$ as $s \to \infty$, so that the boundary term evaluates to zero:

$$\Delta_0' = -\frac{\omega_{\mathrm{pe}}^2}{c^2}\frac{L_s}{k_y v_{T\mathrm{e}}}\left[\int_{0_-}^{-\infty} + \int_{\infty}^{0_+}\right]\left(\omega - \omega_n^* - \frac{1}{2}\omega_T^*\right) Z'(s)ds \ , \tag{6.19}$$

$$\Delta_0' = -\frac{\omega_{\mathrm{pe}}^2}{c^2}\frac{L_s}{k_y v_{T\mathrm{e}}}\left(\omega - \omega_n^* - \frac{1}{2}\omega_T^*\right)\left(Z(0_+) - Z(0_-)\right) \ . \tag{6.20}$$

Evaluating the discontinuity of the plasma dispersion function as the argument passes through zero requires additional work and tools from complex analysis, as s is inherently complex and $Z(s)$ is defined for $\mathrm{Im}(s) > 0$ but requires analytic continuation for $\mathrm{Im}(s) < 0$. Consider evaluation of the integral used to define the plasma dispersion function,

$$Z(s) \equiv \pi^{-1/2}\int_{-\infty}^{\infty}\frac{e^{-v^2}}{v - s}dv \ , \tag{6.21}$$

in the limit that both parts of the complex variable $s = \epsilon + i\delta \to 0$ from two separate routes, one in which $\epsilon, \delta > 0$ (to determine $Z(0_+)$) and one with $\epsilon, \delta < 0$ (to determine $Z(0_-)$). The

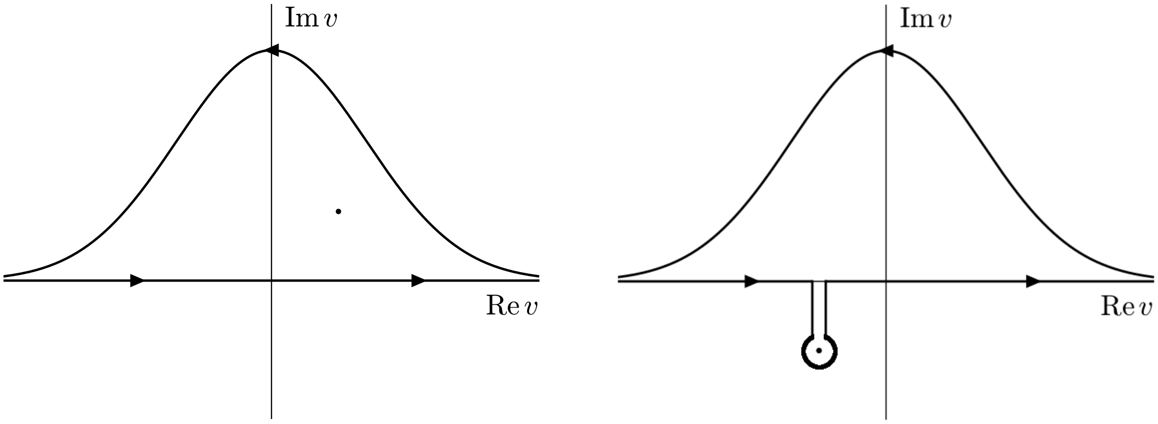

Figure 6.1: Contours of integration extending v into the complex plane, used for (top) Equation (6.22), in which $s = \epsilon + i\delta \to 0_+$ and (bottom) Equation (6.23) in which $s = -\epsilon - i\delta \to 0_-$.

integral can be evaluated along these paths using techniques of contour integration, with the contours given in Fig. 6.2. Using the residue theorem, integration over the two contours is as follows:

$$\pi^{-1/2} \int_{\text{Real line}} \frac{e^{-v^2}}{v - s_+} dv + I_+ = 2\pi i \pi^{-1/2} e^{-s_+^2} \ , \tag{6.22}$$

$$\pi^{-1/2} \int_{\text{Real line}} \frac{e^{-v^2}}{v - s_-} dv + 2\pi i \pi^{-1/2} e^{-s_-^2} + I_- = 2\pi i \pi^{-1/2} e^{-s_-^2} \ . \tag{6.23}$$

$s_\pm$ refers to $\epsilon + i\delta$ and $-\epsilon - i\delta$, respectively. The part of the integral along the real line is simply $Z(s_\pm)$, and $I_\pm$ corresponds to the integral over the curve in the upper half of the plane. As both integrals are taken in the same direction, the function is analytic in the upper half plane, and the contour in the upper half plane is identical, $I_+ = I_-$. Subtracting Eq. (6.23) from Eq. (6.22) in the limit that $s_+, s_- \to 0$, one finds

$$Z(0_+) - Z(0_-) = 2\pi^{1/2} i \ . \tag{6.24}$$

This relation has great utility in the following calculation including magnetic drift effects. Inserting it into Eq. (6.20) and rearranging terms (including defining $k_0 = \omega_{\text{pe}}/c$), one arrives at the expression found in (Drake and Lee, 1977):

$$\omega = \omega_n^* + \frac{1}{2}\omega_T^* + i\frac{\Delta_0' k_y v_{Te}}{2k_0^2 L_s \pi^{1/2}} \; . \tag{6.25}$$

Importantly, for high wavenumbers where one can expect microtearing, $\Delta_0' < 0$, and thus this mode is stable in the collisionless limit. The following section will explore how magnetic drifts act to modify the governing equations for instability.

6.3 Magnetic-Drift-Dependent Dispersion Relation

Having confirmed that the mathematical techniques used in this approach reproduce existing results, these methods are now used to calculate the dispersion relation caused by the inclusion of magnetic drifts that were not accounted for in (Drake and Lee, 1977). Writing out the integral for the current density to first order in the magnetic drift expansion:

$$J_{\parallel,\omega_D} = -e\int d^3\mathbf{v}\, v_\parallel \left(-\frac{eF_M}{T_{\mathrm{e}}}\frac{\bar{\omega}_D(\omega-\bar{\omega}_T^*)}{(\omega-k_\parallel v_\parallel)^2}\left(\Phi - \frac{v_\parallel A_\parallel}{c}\right)\right) \; , \tag{6.26}$$

where $\bar{\omega}_D$ and $\bar{\omega}_T^*$ are both functions of v and u as defined in the previous sections. An identical mathematical procedure to the previous section can be used to the point of u integration (simply integrating higher-order moments of the Gaussian). As in the comparison with (Drake and Lee, 1977), $\Phi = 0$ will be assumed in this calculation. After u integration and gathering terms by order in v, one has

$$J_{\parallel,\omega_D} = -\frac{\omega_D n_0 e^2}{\pi^{1/2} T_{0e} k_\parallel^2}\frac{1}{v_{T\mathrm{e}}}\int_{-\infty}^{\infty} dv e^{-v^2}\frac{v^2(\omega-\omega_n^*) + \frac{1}{2}(\omega-\omega_n^*-\frac{1}{2}\omega_T^*) - \omega_T^* v^4}{(s-v)^2} v^2 \frac{v_{Te}A_\parallel}{c} \; . \tag{6.27}$$

As before, this integral is evaluated using derivatives of the plasma dispersion function. Due to higher powers of v in the integral, there will be higher-order derivatives of $Z(s)$:

$$\begin{aligned} J_{\parallel,\omega_D} = -\frac{\omega_D n_0 e^2}{T_{0e}\omega^2}\frac{s^2 v_{Te}^2}{v_{Te}}\frac{v_{Te}A_\parallel}{c}\Bigg[&(\omega-\omega_n^*)\left(\frac{1}{16}Z^{(5)} + \frac{3}{4}Z^{(3)} + \frac{3}{4}Z^{(1)}\right) \\ &+ \frac{1}{2}(\omega-\omega_n^*-\frac{1}{2}\omega_T^*)\left(\frac{1}{4}Z^{(3)} + \frac{1}{2}Z^{(1)}\right) - \omega_T^*\left(\frac{1}{64}Z^{(7)} + \frac{15}{32}Z^{(5)} + \frac{45}{16}Z^{(3)} + \frac{15}{8}Z^{(1)}\right)\Bigg] \; . \end{aligned} \tag{6.28}$$

$Z^{(n)}$ corresponds to the n-th derivative of Z, and the argument of the plasma dispersion function has been suppressed. This equation is then inserted into Ampere's Law, using the same change of variables from x to s and using the same modified limits of integration. Omitting algebraic manipulations for the sake of brevity, one arrives at the following equation:

$$\begin{aligned}\Delta'_{\omega_D} = &-\frac{2\omega_{pe}^2}{c^2}\frac{\omega L_s}{k_y v_{Te}}\frac{\omega_D}{\omega^2}\left(\int_{0_-}^{-\infty}+\int_{\infty}^{0_+}\right)ds\Bigg[(\omega-\omega_n^*)(\frac{1}{16}Z^{(5)}+\frac{3}{4}Z^{(3)}+\frac{3}{4}Z^{(1)})\\ &+\frac{1}{2}\left(\omega-\omega_n^*-\frac{1}{2}\omega_T^*\right)\left(\frac{1}{4}Z^{(3)}+\frac{1}{2}Z^{(1)}\right)-\omega_T^*\left(\frac{1}{64}Z^{(7)}+\frac{15}{32}Z^{(5)}+\frac{45}{16}Z^{(3)}+\frac{15}{8}Z^{(1)}\right)\Bigg]\,.\end{aligned} \tag{6.29}$$

Δ_{ω_D} is the tearing parameter evaluated from the $\mathcal{O}(\omega_D)$ current density. Bearing in mind that $Z^{(n)}(s) \to 0$ as $s \to \infty$, the integration of this equation is straightforward. Like in Eq. (6.20), the resultant equation will be expressed as the discontinuity in the plasma dispersion function (and its derivatives). To clean up the expression, the following notation will be used: $Z_{\pm}^{(n)}(0) \equiv Z^{(n)}(0_+) - Z^{(n)}(0_-)$; this gives

$$\begin{aligned}\Delta'_{\omega_D} = -\frac{2\omega_{pe}^2}{c^2}\frac{\omega L_s}{k_y v_{Te}}\frac{\omega_D}{\omega^2}\Bigg[&(\omega-\omega_n^*)\left(\frac{1}{16}Z_{\pm}^{(4)}(0)+\frac{3}{4}Z_{\pm}^{(2)}(0)+\frac{3}{4}Z_{\pm}(0)\right)\\ &+\frac{1}{2}\left(\omega-\omega_n^*-\frac{1}{2}\omega_T^*\right)\left(\frac{1}{4}Z_{\pm}^{(2)}(0)+\frac{1}{2}Z_{\pm}(0)\right)-\omega_T^*\Big(\frac{1}{64}Z_{\pm}^{(6)}(0)+\frac{15}{32}Z_{\pm}^{(4)}(0)\\ &+\frac{45}{16}Z_{\pm}^{(2)}(0)+\frac{15}{8}Z_{\pm}(0)\Big)\Bigg]\,.\end{aligned} \tag{6.30}$$

Iterating on the property of plasma dispersion functions that $Z'(s) = -2(1 + sZ(s))$, one can relate the differences in higher order derivatives at $s = 0$ to the difference of the function itself at $s = 0$ (see Appendix B), the value of which is known from Eq. 6.24 as $2i\pi^{1/2}$. Inserting those relations, one finds:

$$
\begin{aligned}
\Delta'_{\omega_D} = -\frac{2\omega_{pe}^2}{c^2}\frac{\omega L_s}{k_y v_{T\mathrm{e}}}\frac{\omega_D}{\omega^2}\Bigg[&(\omega-\omega_n^*)\left(\frac{1}{16}\left(24i\pi^{1/2}\right)+\frac{3}{4}\left(-4i\pi^{1/2}\right)+\frac{3}{4}\left(2i\pi^{1/2}\right)\right)\\
&+\frac{1}{2}\left(\omega-\omega_n^*-\frac{1}{2}\omega_T^*\right)\left(\frac{1}{4}\left(-4i\pi^{1/2}\right)+\frac{1}{2}\left(2i\pi^{1/2}\right)\right)-\omega_T^*\bigg(\frac{1}{64}\left(-240\pi^{1/2}i\right)\\
&+\frac{15}{32}\left(24i\pi^{1/2}\right)+\frac{45}{16}\left(-4i\pi^{1/2}\right)+\frac{15}{8}\left(2i\pi^{1/2}\right)\bigg)\Bigg]=0\ . \qquad (6.31)
\end{aligned}
$$

Equation (6.31) shows that in the $\Phi = 0$ limit, there is no contribution to instability from first-order magnetic drift effects. (Carmody, 2014) found this to be true as well, using a different approach to the calculation. However, gyrokinetic simulations described in (Predebon and Sattin, 2013) observed collisionless microtearing instability, even in the $\Phi = 0$ regime, but only if magnetic drift effects are present. This motivates expanding to higher order in the magnetic drift parameter ω_D, examining now $\mathcal{O}(\omega_D^2)$ effects for $\Phi = 0$:

$$
J^{(2)}_{\parallel,\omega_D} = e\int d^3\mathbf{v}\, v_\parallel\left(-\frac{eF_M}{T_\mathrm{e}}\frac{\bar{\omega}_D^2(\omega-\bar{\omega}_T^*)}{(\omega-k_\parallel v_\parallel)^3}\frac{v_\parallel A_\parallel}{c}\right)\ . \qquad (6.32)
$$

The procedure is identical to calculations in the previous two orders: the u integral is evaluated as moments of a Gaussian distribution, and the v integrals (now with $(v-s)^{-3}$ in the denominator) can again be expressed as higher-order derivatives of the plasma dispersion function as detailed in Appendix B. As before, the higher-order derivatives can be expressed in terms of the original $Z(s)$ function and integrated over the unstable current sheet layer. The details of the calculation are largely the same, so they are mostly omitted. However, one point in the calculation will be pertinent in the discussion that follows. Carrying out the calculation through the v and u integrations and writing out Ampère's Law in terms of s:

$$
\begin{aligned}
\Delta' = \frac{4\pi}{c^2}\frac{L_s}{k_y}\frac{e^2 n_0\omega_D^2}{T_\mathrm{e}}\frac{v_{Te}}{\omega^2}\int ds\, s\Bigg[&\frac{1}{2}\left(\omega-\omega_n^*-\frac{3}{2}\omega_T^*\right)\left(\frac{1}{8}Z^{(4)}+\frac{1}{4}Z^{(2)}\right)\\
&+(\omega-\omega_n^*-\omega_T^*)\left(\frac{1}{32}Z^{(6)}+\frac{3}{8}Z^{(4)}+\frac{3}{8}Z^{(2)}\right)+\left(\omega-\omega_n^*-\frac{1}{2}\omega_T^*\right)\bigg(\frac{1}{128}Z^{(8)}+\frac{15}{64}Z^{(6)}\\
&+\frac{45}{32}Z^{(4)}+\frac{15}{16}Z^{(2)}\bigg)-\omega_T^*\left(\frac{1}{512}Z^{(10)}+\frac{28}{256}Z^{(8)}+\frac{210}{128}Z^{(6)}+\frac{420}{64}Z^{(4)}+\frac{105}{32}Z^{(2)}\right)\Bigg]\ .
\end{aligned}
$$

(6.33)

This integration differs slightly from the previous cases in that there is an additional s term in the integral, a consequence of the additional power of $\omega/k_\parallel$ introduced in the denominator. This extra s can be dealt with via integration by parts. As all derivatives of the Z function go to zero at infinity faster than s grows and are defined at $s=0$, the boundary term $(sZ^{(n)})$ that arises evaluates to zero, and integration by parts is simply a matter of lowering the order of each derivative of the Z function in the above expression. Carrying through the rest of the calculation as before, one finds at the end of the calculation that to $\mathcal{O}(\omega_D^2)$ there is still no contribution to Δ'. While a proof that Δ' is unaffected to all orders in ω_D for the $\Phi = 0$ limit is beyond the scope of this chapter, the following argues that it is a plausible conclusion.

Consider the n-th term in the ω_D expansion; the corresponding current density after $v_\perp$ (or u) integration can be expressed as

$$J_{\parallel,\omega_D}^{(n)} \propto \int dv_\parallel v_\parallel^2 e^{-v_\parallel^2} \frac{\bar{\omega}_D^n \left(\omega - \bar{\omega}_T^*\right)}{(\omega - k_\parallel v_\parallel)^{n+1}} \propto \int dv_\parallel v_\parallel^2 e^{-v_\parallel^2} \left(\frac{s}{\omega}\right)^{n+1} \frac{\bar{\omega}_D^n \left(\omega - \bar{\omega}_T^*\right)}{(s-v)^{n+1}} \ . \tag{6.34}$$

Both $\bar{\omega}_D$ and $\bar{\omega}_T^*$ contain only even powers of v, so for any n, the numerator will always have only even powers of v. As is apparent in the integrals listed in Appendix B, integrals with even powers of v in the numerator result in odd derivatives of the Z function when n is odd, and even derivatives of Z when n is even. When the current density is evaluated, one arrives at the following for Ampère's Law:

$$\Delta' \propto \begin{cases} \int ds\, s^{n-1} \sum\limits_{i \text{ even}} Z^{(i)}(s), & \text{for even } n \\ \int ds\, s^{n-1} \sum\limits_{i \text{ odd}} Z^{(i)}(s), & \text{for odd } n \end{cases} , \tag{6.35}$$

where an s^{-2} factor has been included to account for the change of variables from x to s. For the cases in which n is even, the factor s will be raised to an odd power, meaning after using the integration-by-parts approach used to handle Eq. (6.33), the expression will have only odd derivatives of the Z function. Similarly, when n is odd, s will be raised to an even power, meaning after integration by parts, the expression will have only odd derivatives of Z. Thus, from this argument it can be concluded that Ampère's Law will contain only odd derivatives of the Z function, regardless of order in the ω_D expansion. The calculation up to this point suggests that odd derivatives of Z exhibit a symmetry with respect to the current layer such that integrating over the layer always evaluates to zero. While this is not a proof, it is reasonable to speculate that this trend would continue to any order of odd Z derivatives.

If this property indeed holds true to any order, while ultimately producing a null result for the dispersion relation, it does provide information about the collisionless microtearing mode that has been observed in gyrokinetic simulations to depend on magnetic drift effects in the $\Phi = 0$ limit. Because this calculation has shown that neglecting the magnetic drift resonance results in no additional contribution to instability, the instability must be inherently kinetic in nature. Additionally, as an inherently kinetic instability, it is distinct from the mode described in (Finn and Drake, 1984) which exists within a fluid limit. It is possible that a more sophisticated closure, such as one described in (Hammett and Perkins, 1990), which successfully reproduces certain kinetic effects like Landau damping, may allow for an analytic description of this instability. Additionally, explorations into the behavior of this mode considering $\Phi \neq 0$ case using a kinetic treatment may elucidate additional properties of the magnetic drift effect on microtearing. Both of these ideas are beyond the scope of this thesis but merit further investigation.

6.4 Chapter Summary

This chapter presented an analytic theory that set out to describe the role that magnetic drifts play in collisionless microtearing instabilities. A neglect of the magnetic drift resonance, motivated by the success of a fluid theory in describing a mode with similar features including curvature drift dependencies, was employed for analytic tractability. The mathematical techniques used in this chapter were borrowed from a well-established analytic theory for collisionless tearing modes,used here in the $\Phi = 0$ regime to calculate a dispersion relation to multiple orders in an expansion in which $\omega_D \ll \omega - k_\parallel v_\parallel$. It was found definitively that magnetic drifts contribute no additional instability drive to at least second order in ω_D, and a plausibility argument is made that this finding may extend to any order in ω_D. This suggests that the collisionless, magnetic-drift-drive microtearing that has been observed in gyrokinetics is distinct from the mode present in previous fluid models, requiring a more accurate description of the magnetic drift resonance to capture the relevant physics.

7 CONCLUSION

This thesis has explored the interaction between magnetic fluctuations and microturbulence, with a special emphasis on the role of zonal flows. Of central importance to this interaction is the physical phenomenon of zonal flow decay induced by the radial movement of particles streaming along perturbed field lines (a result of large-scale magnetic fluctuations). This eroded zonal flow then is less effective at quenching turbulence and transport at ion microturbulent scales, and thus resolving both large-scale magnetic activity and small-scale microturbulence is critical to accurately predicting transport levels. This inherently multi-scale physics is seen across different toroidal confinement devices, including tearing modes in the Madison Symmetric Torus Reversed-Field Pinch and Resonant Magnetic Perturbations in the DIII-D tokamak. The effect extends to even more fundamental plasma regimes than toroidal fusion devices, manifesting in a simple slab system that is unstable to both tearing instabilities and microinstability. Additionally, specific linear instability properties of a magnetic instability that occurs at micro-unstable ($\sim$ ion gyroradius) scales were examined. Key results from this thesis are summarized below, followed by a discussion on potential areas for future research.

7.1 Tearing Modes and Microturbulence in the RFP

The initial investigations discussed in this thesis involved gyrokinetic simulations of the Madison Symmetric Torus Reversed-Field Pinch while working closely with experimentalists to identify linear instabilities and characterize turbulence in improved-confinement MST discharges. It was noted that in these improved-confinement PPCD discharges, a reduction of tearing mode activity resulted in increased density gradients towards the edge of the device, driving high-frequency fluctuations. Simulations identified these fluctuations as ∇n-driven Trapped-Electron Modes. Nonlinear simulations of these discharges exhibit unprecedentedly strong zonal flows that entirely suppress turbulence and transport; importantly, these simulations did not provide any mechanism to account for radial magnetic field fluctuations brought about by residual tearing mode fluctuations. When accounting for these tearing modes via an externally imposed radial magnetic field fluctuation, the simulations produced much larger transport levels attributed to the zonal flow being weakened by magnetic flutter. Similar analysis was performed for a separate PPCD discharge which was unstable to ITG instead of ∇n-TEM. This discharge differed significantly in that without tearing fluctuations, the transport was still finite despite the presence of significant zonal structures, and additionally the inclusion of radial tearing fluctuations did little to affect transport levels. In the tearing-free limit, it was found that the very-low-q geometry of the RFP has a large Rosenbluth-Hinton residual, which corresponds to a minimal reduction of zonal flow amplitude via neoclassical shielding effects. ITG- and TEM-dominated discharges differ in two key aspects, collisionality and secondary instability growth rates. Collisionality serves to damp TEM significantly (more so than the concurrent collisional zonal flow damping) while having little effect on ITG, and secondary growth rates as a proxy for zonal flow growth calculated in the simulations were higher for the TEM than for the ITG discharge. These combined effects serve to explain the discrepancy in the tearing-free regime. It was also found that the ITG present was a more slab-like branch of the instability, which depends far less on zonal flows for saturation than its toroidal counterpart, so while tearing fluctuations degrade zonal flows in both cases, the effect on transport was much smaller for the ITG-dominated discharge. However, it is still evident that for microturbulence which depends upon zonal flows for turbulent saturation, inclusion of magnetic fluctuations generated from larger-scale dynamics are essential for a complete physical picture.

7.2 RMPs and Microturbulence in the Tokamak L-Mode

The finding that this magnetic fluctuation-zonal-flow-microturbulence interaction plays such a significant role in MST transport levels motivated additional work to determine if this phenomenon is unique to the RFP, or if it extends to other toroidal fusion devices. To this end, a joint experimental-theoretical effort studied the effect of Resonant Magnetic Perturbations on microturbulence levels in the DIII-D tokamak. Beam Emission Spectroscopy probes on the DIII-D tokamak measured a direct increase in density fluctuations at microturbulent frequencies with the application of an $n = 3$ RMP during an L-mode discharge. Gyrokinetic simulations were performed to connect the observed behavior with the previously discussed zonal flow decay mechanism. Both ∇T-TEM and ITG instabilities were present in the discharge, contributing to the turbulence. Nonlinear simulations modeled the RMP using an externally imposed $A_\parallel$ perturbation identical in structure to that used in the MST studies to model tearing fluctuations. Much like in the experiment, density fluctuations increased commensurately with RMP amplitude. However, key differences arise when comparing the B_r amplitude required to achieve this increase between experiment and simulations. At experimental values of β, the flux-tube simulations produced an electromagnetic mode at very large spatial scales that is not present in the experiment, which made nonlinear convergence unattainable. To mitigate this mode, β was reduced by a factor of four; a consequence of this was that a much larger B_r was needed in simulation to produce magnetic diffusivity comparable to the experiment (which used B_r values much smaller than typical ELM-supression values). Additionally, the turbulence levels scaled non-monotonically over a certain region of RMP amplitudes, which was attributed to the effect of turbulent temperature and density corrugations as the RMP island widths approach corrugation scale lengths. Across all RMP amplitudes, there were signatures of decreasing zonal flow, connecting the observed changes in turbulence to magnetic flutter decay. Additionally, this effect only occurred for RMPs that exhibit flux-surface-breaking parity, in agreement with prior work that observed flux-surface-preserving RMPs to have little effect on turbulence.

7.3 Multi-scale Interactions in a Slab Plasma System

Having established in Chapters 3 and 4 the importance of magnetic fluctuation-zonal-flow-microturbulence interactions for setting transport levels across different types of magnetic fluctuations and toroidal fusion devices, effort was turned towards examining a plasma slab system. Magnetic activity in this system was introduced via a modification of the linear gyrokinetic operator to allow for radially periodic equilibrium plasma current gradients, which can drive collisionless tearing modes. The slab system with both current and ion temperature gradients was unstable to tearing modes at low wavenumbers, slab-ITG modes at high wavenumbers, and a new mode distinct from either of the others modes that spanned both scales and was characterized at length via structure and parametric dependencies. Nonlinear simulations of this system portrayed a separation of dynamics at both temporal and spatial scales, with small-scale electrostatic turbulence dominating in the early phases of the simulation and large-scale electromagnetic turbulence dominating later on. Comparing to single-scale simulations of an only slab-ITG-unstable system and a tearing-unstable system separately, the saturated turbulence level of the system with both instabilities together was considerably higher, despite linear growth rates being lower than either of the single-scale cases. This demonstrated a modification of turbulence that can be attributed to nonlinear, cross-scale physics. Additionally, a decay in zonal flow concurrent with an increase in electromagnetic activity during the dominantly electrostatic turbulent phase was observed, providing an additional regime in which magnetic-flutter-induced zonal-flow decay occurs. In the electromagnetic regime, there were signatures of both tearing activity and microturbulence present in flux spectra, qualitatively similar to experimental measurements made in standard operation MST plasmas, which suggested underlying physics similarities between the reduced system studied here and the RFP.

7.4 Curvature Drift Effects on Collisionless Microtearing Instability

An analytic calculation was performed to describe microtearing modes in the collisionless limit, which are potentially of great importance to the RFP configuration. Though previous analytical work required collisions for instability, more recent computational models observed the destabilization of collisionless microtearing via curvature drift. An analytic calculation starting from the drift-kinetic equation, assuming a fluid expansion in the curvature drift resonance, was performed to derive a modification to the linear dispersion relation by curvature drifts. This work suggested that in the $\Phi = 0$ limit, the enhancement of collisionless microtearing due to magnetic drifts observed in gyrokinetic simulations is a dominantly kinetic effect, as a fluid expansion of the magnetic drift resonance contributed no additional terms to instability to at least second order in the expansion. These findings distinguished this mode from the curvature-drift-driven branch of microtearing that occurs in a semicollisional regime, which can be described using the Braginskii equations.

7.5 Areas for Future Research

Further Computational Explorations of RMPs on DIII-D

This thesis reported on initial efforts regarding gyrokinetic investigations of RMP-microturbulence interaction in DIII-D plasmas, but there is still interesting physics that remains to be explored. One open question regards the anomalous mode that appears at very low k_y and is destabilized by β; whether this is an artifact of the flux-tube approximation that can be removed with global (either full-flux-surface or full-volumne) simulations or something more remains to be determined. If converged simulations can be achieved at experimental β, then more quantitatively accurate comparisons can be made between experimental and numerically applied RMPs.

An additional physics question concerns the role that plasma rotation plays on the effect discussed in this work. It is known that plasma rotation shields RMPs and prevents them from penetrating into the plasma as effectively (Fitzpatrick, 1993), and that the DIII-D L-mode tokamak has non-negligible rotation. It is likely that this rotation would have an effect on the RMP-induced zonal flow decay and subsequently the turbulence levels; investigating exactly how this manifests is an open challenge.

Advancing Understanding of Gyrokinetic Systems with Equilibrium Current Gradient

Part of this work involved introducing the capability for equilibrium current gradients into the GENE linear gyrokinetic operator, which allowed for investigations into a system with both an ion temperature gradient and a current gradient. This opens the door to many different physics investigations. Acquiring a more complete understanding of the hybrid drift-tearing mode that is formed beyond just a characterization of its parametric dependencies, as well as finding a way to more definitively describe how much it actually contributes to the turbulence, is an important task. This capability lends itself well to applications not only to toroidal plasma devices (specifically the RFP with its large current gradients), but also to astrophysical plasmas, such as using gyrokinetics to model reconnection in the presence of pressure gradients. Given the low collisionality of astrophysical plasmas, this capability may in fact be better suited to such studies. One possible matter of interest is to examine if tearing modes can nonlinearly excite small-scale linear instabilities that are otherwise linearly stable through nonlinear cascade processes. Additionally, a more long-term project would be adapting this current gradient implementation to toroidal geometries and radially global simulation regimes in order to acquire a more physically accurate depiction of how core tearing modes and edge microturbulence interact in a Reversed-Field Pinch.

The Role of Stable Eigenmodes in Tearing Mode Turbulence

Another application of the current gradient capability now available in GENE is to use the eigenmode solver to characterize eigenmodes in tearing-unstable systems. Specifically, this would allow a study into the effect that stable eigenmodes have on tearing mode turbulence. There has been extensive work showing the importance of stable modes in turbulence saturation for a variety of systems and instabilities (Baver et al., 2002; Hatch et al., 2012; Terry et al., 2006; Makwana et al., 2011; Whelan et al., 2018). Recent work

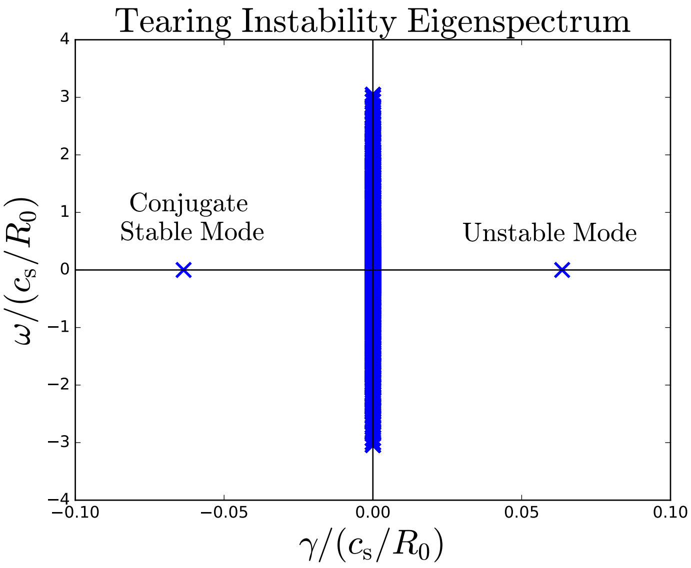

Figure 7.1: Eigenspectrum at $k_y = 0.05$ for a system with only a current gradient. There exist a large number of marginally stable modes along the y-axis (corresponding to zero growth rate), an unstable mode at zero frequency, and then a conjugate stable mode with damping rate that is equal in magnitude to the unstable mode growth rate. This eigenspectrum is very similar to that of a Kelvin-Helmholtz unstable system, in which the unstable/conjugate stable mode pair alone are able to account for a significant portion of the turbulent dynamics.

studying stable modes in shear-flow-unstable systems has shown that aspects of a turbulent, Kelvin-Helmholtz-unstable system can be well described using a truncated mode expansion that includes only the unstable mode and its conjugate stable mode (Fraser et al., 2018). As the equations that describe Kelvin-Helmholtz and collisionless tearing instabilities are similar upon the exchange of flow velocity and magnetic field, it is reasonable to expect similar physics may be present in for a tearing-unstable system. Preliminary investigations looking at the eigenmodes of a system with only a current gradient show a spectrum very similar to that seen in the Kelvin Helmholtz work, with a single unstable mode and conjugate stable mode, in addition to a band of marginal modes (see Fig. 7.1). As tearing modes can be found both in fusion plasmas and astrophysical systems, being able to explain aspects of their physics using truncated models is of great value.

A TEARING PERTURBATION IMPLEMENTATION

In Chapters 3 and 4, the Gene code is modified to include radial magnetic field fluctuations beyond those self-consistently generated by plasma dynamics. This is done here by including a constant-in-time resonant $A_\parallel$ perturbation. The details of the implementation, adapted from (Carmody et al., 2015), are discussed in what follows. Beginning with Ampere's Law,

$$k_\perp^2 A_\parallel^{\text{sc}} = j_\parallel = \frac{\beta}{2}\sum_j q_j n_{0j} v_{Tj} \pi B_0 \int v_\parallel J_0(\lambda_j) f_j(k) dv_\parallel d\mu \ , \tag{A.1}$$

where $f_j = g_j - (q_j v_{Tj} v_\parallel F_{j0}/T_{j0})A_\parallel$ is the distribution function of species j, while β is the ratio of plasma pressure to magnetic field pressure, q_e is electron charge, B_0 is the background magnetic field, $v_\parallel$ is the velocity parallel to the magnetic field, μ is the magnetic moment, J_0 is the zeroth-order Bessel function, and $\lambda_j \equiv (\sqrt{2B_0\mu/m_j})k_\perp/\Omega_j$. To include the tearing perturbation, one may add an external perturbation $A_\parallel^{\text{ext}}$ to the self-consistent $A_\parallel^{\text{sc}}$, such that $A_\parallel \to A_\parallel^{\text{sc}}(k_x, k_y, z, t) + A_\parallel^{\text{ext}}(0, k_{y,\text{min}}, z)$. Plugging this perturbed distribution function $f_j = g_j + \frac{q_j}{m_j c}\frac{\partial F_{0j}}{\partial v_\parallel}(A_\parallel^{\text{sc}} + A_\parallel^{\text{ext}})$ into Eq. (A.1), one obtains

$$k_\perp^2 A_\parallel^{\text{sc}} = \frac{\beta}{2} q_e n_{0e} v_{Te} \pi B_0 \int v_\parallel J_0(\lambda)(g - q_e v_\parallel v_{Te} F_0/T_{0e}(A_\parallel^{\text{sc}} + A_\parallel^{\text{ext}}))dv_\parallel d\mu \tag{A.2}$$

Solving for $A_\parallel^{\text{sc}}$:

$$\begin{aligned} k_\perp^2 A_\parallel^{\text{sc}} = \frac{\beta}{2} q_e n_{0e} v_{Te} \pi B_0 \int \Big[& v_\parallel J_0(\lambda) g - v_\parallel J_0(\lambda) q_e v_\parallel v_{Te} F_0/T_{0e} A_\parallel^{\text{sc}} \\ & + v_\parallel J_0(\lambda) q_e v_\parallel v_{Te} F_0/T_{0e} A_\parallel^{\text{ext}} \Big] dv_\parallel d\mu \end{aligned} \tag{A.3}$$

$$\begin{aligned} A_\parallel^{\text{sc}} = & \frac{\frac{\beta}{2} q_e n_{0e} v_{Te} \pi B_0 \int v_\parallel J_0(\lambda) g dv_\parallel d\mu}{k_\perp^2 + \frac{\beta}{2} q_e n_{0e} v_{Te} \pi B_0 \int v_\parallel J_0^2(\lambda) q_e v_\parallel v_{Te} F_0/T_{0e} dv_\parallel d\mu} \\ & - \frac{\frac{\beta}{2} q_e n_{0e} v_{Te} \pi B_0 \int v_\parallel J_0^2(\lambda) q_e v_\parallel v_{Te} F_0/T_{0e} dv_\parallel d\mu}{k_\perp^2 + \frac{\beta}{2} q_e n_{0e} v_{Te} \pi B_0 \int v_\parallel J_0^2(\lambda) q_e v_\parallel v_{Te} F_0/T_{0e} dv_\parallel d\mu} A_\parallel^{\text{ext}} \end{aligned} \tag{A.4}$$

Writing $A_\parallel^{\text{tot}} = A_\parallel^{\text{sc}} + A_\parallel^{\text{ext}}$,

$$A_\parallel^{\text{tot}} = \frac{\frac{\beta}{2} q_e n_{0e} v_{Te} \pi B_0 \int v_\parallel J_0(\lambda) g dv_\parallel d\mu}{k_\perp^2 + \frac{\beta}{2} q_e n_{0e} v_{Te} \pi B_0 \int v_\parallel J_0^2(\lambda) q_e v_\parallel v_{Te} F_0 / T_{0e} dv_\parallel d\mu} - \frac{\frac{\beta}{2} q_e n_{0e} v_{Te} \pi B_0 \int v_\parallel J_0^2(\lambda) q_e v_\parallel v_{Te} F_0 / T_{0e} dv_\parallel d\mu}{k_\perp^2 + \frac{\beta}{2} q_e n_{0e} v_{Te} \pi B_0 \int v_\parallel J_0^2(\lambda) q_e v_\parallel v_{Te} F_0 / T_{0e} dv_\parallel d\mu} A_\parallel^{\text{ext}} + A_\parallel^{\text{ext}} \quad \text{(A.5)}$$

$$A_\parallel^{\text{tot}} = \frac{\sum_j \frac{\beta}{2} q_j n_{0j} v_{Tj} \pi B_0 \int v_\parallel J_0(\lambda_j) g dv_\parallel d\mu}{k_\perp^2 + \sum_j \frac{\beta}{m_j} q_j^2 n_{0j} \pi B_0 \int v_\parallel^2 J_0^2(\lambda_j) F_0 dv_\parallel d\mu} + \frac{k_\perp^2 A_\parallel^{\text{ext}}}{k_\perp^2 + \sum_j \frac{\beta}{m_j} q_j^2 n_{0j} \pi B_0 \int v_\parallel^2 J_0^2(\lambda_j) F_0 dv_\parallel d\mu} \quad \text{(A.6)}$$

The first term on the right-hand-side of Eq. (A.6) represents the standard picture of $A_\parallel$ evolution without any perturbation, taken from Ampere's law; the second term is the contribution of an externally imposed perturbation. Note that Ref. Carmody et al. (2015) neglected the prefactor on the second term in Eq. (A.6). The functional form of the tearing-parity perturbation is implemented as a Gaussian in the z direction (parallel to the background magnetic field), $A_\parallel^{\text{ext}} = A_0 e^{-z^2}$. In chapter 3, the RMP was applied at the largest y scale permitted by the simulation domain. This scale was still in the microturbulence range, not reflecting the larger spatial scales of MST tearing modes. For DIII-D RMPs in chapter 4, physically realistic scale separation between the RMP and the microturbulence was utilized in simulation. The value chosen for the amplitude of the perturbation in the MST simulations is informed from experimental measurements: high-n B_ϕ and B_θ fluctuations are measured outside the reversal surface, and B_r is determined relative to these via the tearing eigenfunction solver RESTER (Sovinec, 1995).

B DETAILS OF THE PLASMA DISPERSION FUNCTION

This appendix lists properties of the plasma dispersion function that are used to calculate integrals over parallel velocity in Chapter 6. Beginning with the definition of $Z(s)$, higher order v moments can be calculated via integration by parts and the following property: $Z'(s) = -2(1 + sZ(s))$

$$\pi^{-1/2}\int_{-\infty}^{\infty}\frac{e^{-v^2}}{(v-s)}dv = Z(s) \tag{B.1}$$

$$\pi^{-1/2}\int_{-\infty}^{\infty}\frac{e^{-v^2}}{(v-s)^2}dv = Z^{(1)}(s) \tag{B.2}$$

$$\pi^{-1/2}\int_{-\infty}^{\infty}\frac{ve^{-v^2}}{(v-s)^2}dv = -\frac{1}{2}Z^{(2)}(s) \tag{B.3}$$

$$\pi^{-1/2}\int_{-\infty}^{\infty}\frac{v^2e^{-v^2}}{(v-s)^2}dv = \frac{1}{4}Z^{(3)} + \frac{1}{2}Z^{(1)} \tag{B.4}$$

$$\pi^{-1/2}\int_{-\infty}^{\infty}\frac{v^3e^{-v^2}}{(v-s)^2}dv = -\frac{1}{8}Z^{(4)} - \frac{3}{4}Z^{(2)} \tag{B.5}$$

$$\pi^{-1/2}\int_{-\infty}^{\infty}\frac{v^4e^{-v^2}}{(v-s)^2}dv = \frac{1}{16}Z^{(5)} + \frac{3}{4}Z^{(3)} + \frac{3}{4}Z^{(1)} \tag{B.6}$$

$$\pi^{-1/2}\int_{-\infty}^{\infty}\frac{v^5e^{-v^2}}{(v-s)^2}dv = -\frac{1}{32}Z^{(6)} - \frac{5}{8}Z^{(4)} - \frac{15}{8}Z^{(2)} \tag{B.7}$$

$$\pi^{-1/2}\int_{-\infty}^{\infty}\frac{v^6e^{-v^2}}{(v-s)^2}dv = \frac{1}{64}Z^{(7)} + \frac{15}{32}Z^{(5)} + \frac{45}{16}Z^{(3)} + \frac{15}{8}Z^{(1)} \tag{B.8}$$

$$\pi^{-1/2}\int_{-\infty}^{\infty}\frac{v^7e^{-v^2}}{(v-s)^2}dv = -\frac{1}{128}Z^{(8)} - \frac{21}{64}Z^{(6)} - \frac{105}{32}Z^{(4)} - \frac{105}{16}Z^{(2)} \tag{B.9}$$

$$\pi^{-1/2}\int_{-\infty}^{\infty}\frac{v^8e^{-v^2}}{(v-s)^2}dv = \frac{1}{256}Z^{(9)} + \frac{28}{128}Z^{(7)} + \frac{210}{64}Z^{(5)} + \frac{420}{32}Z^{(3)} + \frac{105}{16}Z^{(1)} \tag{B.10}$$

In performing the $\mathcal{O}(\omega_D^2)$ calculation, it is necessary to evaluate integrals with $(v-s)^3$ in the denominator. This is simply done by taking s derivatives of the above equations and including an additional factor of $\frac{1}{2}$.

For part of the calculation, it is useful to represent varying orders of derivatives of the plasma dispersion function at $s = 0$ as multiples of the plasma dispersion function at $s = 0$. This can be done by using the relation $Z'(s) = -2\left(1 + sZ\right)$, which upon iteration gives:

$$Z^{(n)} = -2\left((n-1)Z^{(n-2)} + sZ^{(n-1)}\right), n \geq 2\ . \tag{B.11}$$

From this, any higher-order derivative can be expressed in terms of the function and its first derivative. The following relations are used in the derivation of magnetic-drift-driven microtearing instability.

$$Z^{(8)}(0) = -1680Z(0) \tag{B.12}$$

$$Z^{(6)}(0) = -120Z(0) \tag{B.13}$$

$$Z^{(5)}(0) = 32Z'(0) \tag{B.14}$$

$$Z^{(4)}(0) = 12Z(0) \tag{B.15}$$

$$Z^{(3)}(0) = -4Z'(0) \tag{B.16}$$

$$Z^{(2)}(0) = -2Z(0) \tag{B.17}$$

$$Z^{(1)}(0) = -2 \tag{B.18}$$

C INCLUSION OF A CURRENT GRADIENT DRIVE IN GENE

In Eq. (5.1) of Chapter 5, the linear operator used in the gyrokinetic code Gene is modified to include a current gradient drive in the local flux-tube limit. This appendix briefly sketches how the terms in that equation were derived. Beginning with Eq. 2.14, and simply by assuming no pressure gradients, curvature, z-dimensional effects, or collisions:

$$\frac{\partial g_j}{\partial t} + \vec{v}_{E\times B} \cdot \vec{\nabla} F_{0j} + \vec{v}_{E\times B} \cdot \vec{\Gamma}_j = 0 \ , \tag{C.1}$$

where $\vec{\Gamma}_j = \vec{\nabla} g_j - \frac{q_j}{m_j v_\parallel}\frac{\partial F_{0j}}{\partial v_\parallel}\vec{\nabla}\chi_j + \frac{q_j}{m_j c}\bar{A}_{1\parallel}\vec{\nabla}\frac{\partial F_{0j}}{\partial v_\parallel}$. Assume now that the equilibrium is a shifted Maxwellian:

$$F_{0j} = \left(\frac{m_j}{2\pi T_{0j}}\right) n_{0j} \exp\left[-\frac{m_j/2(v_\parallel - v_{0j}(x))^2 + \mu B_0}{T_{0j}}\right] \tag{C.2}$$

Inserting this into Eq. (C.1), one arrives at

$$\frac{\partial g_j}{\partial t} + \vec{v}_{E\times B} \cdot \frac{m_j}{T_{0j}}(v_\parallel - v_{0j}) F_{0j} \vec{\nabla} v_{0j} + \vec{v}_{E\times B} \cdot \vec{\Gamma}_j = 0. \tag{C.3}$$

The $E \times B$ velocity can be expressed as $\vec{v}_{E\times B} = \frac{c}{B_0}\vec{b}_0 \times \vec{\nabla}\chi$. Following the treatment of vector expressions as detailed in Chapter 2 of (Merz, 2008), Eq. (C.3) can be expanded in the following way:

$$\vec{v}_{E\times B} \cdot \vec{\nabla} v_{0j} = \frac{c}{B_0}\left(\vec{b}_0 \times \vec{\nabla}\chi\right) \cdot \vec{\nabla} v_{0j} = \partial_y \chi \partial_x v_{0j} \tag{C.4}$$

$$\vec{v}_{E\times B} \cdot \vec{\Gamma}_j = \frac{c}{B_0}\left(\vec{b}_0 \times \vec{\nabla}\chi\right) \cdot \vec{\Gamma}_j = \partial_x \chi \Gamma_{jy} - \partial_y \chi \Gamma_{jx} \ , \tag{C.5}$$

where the prefactor $Jb^3 \frac{c}{B_0}\gamma_1$ that arises from the vector expressions has been omitted, as it in the end is removed by normalization. The original governing assumptions stated that χ has no equilibrium component, however the inclusion of a radially-dependent equilibrium flow results in a correspondingly altered potential, such that $\chi \to \chi_0(x) + \chi(x, y)$. This new potential is then inserted into Eq. (C.3) and simplified:

$$\frac{\partial g_j}{\partial t} = \partial_y \chi \partial_x v_{0j} \frac{m_j}{T_{0j}}(v_\parallel - v_{0j}) F_{0j} - \left(\partial_x(\chi_0 + \chi)\Gamma_{jy} - \partial_y \chi \Gamma_{jx}\right) \ , \tag{C.6}$$

$$\frac{\partial g_j}{\partial t} = \partial_y \chi \partial_x v_{0j} \frac{m_j}{T_{0j}} (v_\parallel - v_{0j}) F_{0j} - \partial_x \chi_0 \Gamma_{jy} - (\partial_x \chi \Gamma_{jy} - \partial_y \chi \Gamma_{jx}) \ , \tag{C.7}$$

$$\frac{\partial g_j}{\partial t} = \partial_y \chi \partial_x v_{0j} \frac{m_j}{T_{0j}} (v_\parallel - v_{0j}) F_{0j} - \partial_x \chi_0 \left(\partial_y g_j - \frac{q_j}{m_j v_\parallel} \frac{\partial F_{0j}}{\partial v_\parallel} \partial_y \chi_j + \frac{q_j}{m_j c} \bar{A}_{1\parallel} \partial_y \frac{\partial F_{0j}}{\partial v_\parallel} \right) - (\partial_x \chi \Gamma_{jy} - \partial_y \chi \Gamma_{jx}) \ , \tag{C.8}$$

$$\frac{\partial g_j}{\partial t} = \partial_y \chi \partial_x v_{0j} \frac{m_j}{T_{0j}} (v_\parallel - v_{0j}) F_{0j} - \partial_x \chi_0 \partial_y g_j + \partial_x \chi_0 \frac{q_j}{m_j v_\parallel} \frac{\partial F_{0j}}{\partial v_\parallel} \partial_y \chi_j - (\partial_x \chi \Gamma_{jy} - \partial_y \chi \Gamma_{jx}) \ , \tag{C.9}$$

where in Eq. (C.8) the definition for Γ_{jy} was inserted into the second term on the RHS, and the y-derivative of the equilibrium Maxwellian evaluates to zero. Rearranging terms, one arrives at

$$\frac{\partial g_j}{\partial t} = \partial_y \chi_j \left(\partial_x v_{0j} \frac{m_j}{T_{0j}} (v_\parallel - v_{0j}) F_{0j} + \partial_x \chi_0 \frac{q_j}{m_j v_\parallel} \frac{\partial F_{0j}}{\partial v_\parallel} \right) - \partial_x \chi_0 \partial_y g_j - (\partial_x \chi \Gamma_{jy} - \partial_y \chi \Gamma_{jx}) \ . \tag{C.10}$$

'Undoing' the derivative of the equilibrium distribution function on the RHS, and recognizing from the definition of χ that $\chi = -(v_\parallel/c) A_{\parallel,0}$ (as there is no equilibrium Φ), the equation can be written as

$$\frac{\partial g_j}{\partial t} = \partial_y \chi_j \left(\partial_x F_{0j} - \partial_x A_{\parallel,0} \frac{q_j}{m_j c} \frac{\partial F_{0j}}{\partial v_\parallel} \right) - \partial_x \chi_0 \partial_y g_j - (\partial_x \chi \Gamma_{jy} - \partial_y \chi \Gamma_{jx}) \ . \tag{C.11}$$

From the definition of g_j given in Eq. (2.11), one can see the parenthesis in the first term on the RHS is simply the x-derivative of that term. Extracting an x derivative from the second term in the parenthesis will produce an additional term, but it is $\mathcal{O}(\delta^2)$ and neglected here. The resultant equation is

$$\frac{\partial g_j}{\partial t} = \partial_y \chi_j \partial_x G_{0j} - \partial_x \chi_0 \partial_y g_j - (\partial_x \chi \Gamma_{jy} - \partial_y \chi \Gamma_{jx}) \ , \tag{C.12}$$

which exhibits the new term of Eq. (5.1) plus the $E \times B$ nonlinearity.

REFERENCES

Anderson, J. K., C. B. Forest, T. M. Biewer, J. S. Sarff, and J. C. Wright. 2004. Equilibrium reconstruction in the madison symmetric torus reversed field pinch. *Nucl. Fusion* **44**.

Applegate, D. J., C. M. Roach, J. W. Connor, S. C. Cowley, W. Dorland, R. J. Hastie, and N. Joiner. 2007. Micro-tearing modes in the mega ampere spherical tokamak. *Plasma Phys. Control. Fusion* **49**:1113.

Baalrud, S. D., A. Bhattacharjee, and W. Daughton. 2018. Collisionless kinetic theory of oblique tearing instabilities. *Phys. Plasmas* **25**:022115.

Barton, J., W. Wehner, E. Schuster, F. Felici, and O. Sauter. 2015. Simultaneous closed-loop control of the current profile and the electron temperature profile in the TCV tokamak. *2015 IEEE American Control Conference.*

Baver, D. A., P. W. Terry, and R. Gatto. 2002. Nonlinear stability and instability in collisionless trapped electron mode turbulence. *Phys. Plasmas* **9**:3318.

Beer, M. A. 1995. Gyrofluid models of turbulent transport in tokamaks. *Ph. D. Thesis, Princeton University.*

Biglari, H., P. H. Diamond, and P. W. Terry. 1990. Influcence of sheared poloidal rotation on edge turbulence. *Phys. Fluids B* **2**:1.

Biskamp, Dieter. 2003. *Magnetohydrodynamic turbulence.* Cambridge University Press.

Boldyrev, S., J. C. Perez, J. E. Borovsky, and J. J. Podesta. 2011. Spectral scaling laws in magnetohydrodynamic turbulence simulations and in the solar wind. *The Astrophysical Journal* 741(1).

Brizard, A. J., and T. S. Hahm. 2007. Foundations of nonlinear gyrokinetic theory. *Rev. Mod. Phys.* **79**:421.

Burrell, K. H. 1997. Effects of eÃ—b velocity shear and magnetic shear on turbulence and transport in magnetic confinement devices. *Phys. Plasmas* **4**:1499.

Carmody, D., M. J. Pueschel, J. K. Anderson, and P. W. Terry. 2015. Microturbulence studies of pulsed poloidal current drive discharges in the reversed field pinch. *Phys. Plasmas* **22**:012504.

Carmody, D., M. J. Pueschel, and P. W. Terry. 2013. Gyrokinetic studies of microinstabilities in the reversed field pinch. *Phys. Plasmas* **20**:052110.

Carmody, D. R. 2014. Microinstabilities and turbulent transport in the reversed field pinch. *Ph. D. Thesis, University of Wisconsin-Madison.*

Catto, P. J., and M. N. Rosenbluth. 1981. Trapped electron modifications to tearing modes in the low collision frequency limit. *Phys. Fluids* **24**:243.

Chapman, B. E., A. F. Almagri, J. K. Anderson, D. L. Brower, K. J. Caspary, D. J. Clayton, D. Craig, D. J. Den Hartog, W. X. Ding, D. A. Ennis, G. Fiksel, S. Gangadhara, S. Kumar, R. M. Magee, R. O'Connell, E. Parke, S. C. Prager, J.A. Reusch, J. S. Sarff, H. D. Stephens, and Y. M. Yang. 2010. Generation and confinement of hot ions and electrons in a reversed-field pinch plasma. *Plasma Phys. Control. Fusion* **52**:124048.

Connor, J. W., S. C. Cowley, and R. J. Hastie. 1990. Micro-tearing stability in tokamaks. *Plasma Phys. Control. Fusion* **32**:799.

Coppi, B., and F. Pegoraro. 1977. Theory of the ubiquitous mode. *Nucl. Fusion* **17**:969.

Cowley, S. C., R. M. Kulsrud, and T. S. Hahm. 1986. Linear stability of tearing modes. *Phys. Fluids* **29**:3230.

Cowley, S. C., R. M. Kulsrud, and R. Sudan. 1991. Considerations of ion-temperature-gradient-driven turbulence. *Phys. Fluids B* **3**:2767.

Dannert, T. 2005. Gyrokinetische simulation von plasmaturbulenz mit gefangenen teilchen und elektromagnetischen effekten. *Ph. D. Thesis, Technische Universität München.*

Dannert, T., and F. Jenko. 2005. Gyrokinetic simulation of collisionless trapped-electron mode turbulence. *Phys. Plasmas* **12**:072309.

D'Haeseleer, W. D., W. N. G. Hitchon, J. D. Callen, and J. L. Shohet. 1991. Flux coordinates and magnetic field structure. *Springer.*

Dimits, A. M., M. A. Beer G. Bateman, B. I. Cohen, W. Dorland, G. W. Hammett, C. Kim, J. E. Kinsey, M. Kotschenreuther, A. H. Kritz, L. L. Lao, J. Mandrekas, W. M. Nevins, S. E. Parker, A. J. Redd, D. E. Shumaker, R. Sydora, and J. Weiland. 2000. Simulations of ion temperature gradient turbulence in tokamaks. *Phys. Plasmas* **7**:969.

Dimits, A. M., T. J. Williams, J. A. Byers, and B. I. Cohen. 1996. Scalings of ion-temperature-gradient-driven anomalous transport in tokamaks. *Phys. Rev. Lett.* **77**:71.

Doerk, H., F. Jenko, T. Görler, D. Told, M. J. Pueschel, and D. R. Hatch. 2012. Gyrokinetic prediction of microtearing turbulence in standard tokamaks. *Physics of Plasmas* **19**:055907.

Doerk, H., F. Jenko, M. J. Pueschel, and D. R. Hatch. 2011. Gyrokinetic microtearing turbulence. *Phys. Rev. Lett.* **106**.

Drake, J. F., and Y. C. Lee. 1977. Kinetic theory of tearing instabilities. *Phys. Fluids* **20**:1341.

Duff, J. R., Z. R. Williams, D. L. Brower, B. E. Chapman, W. X. Ding, M. J. Pueschel, J. S. Sarff, and P. W. Terry. 2018. Observation of trapped-electron-mode microturbulence in reversed field pinch plasmas. *Phys. Plasmas* **25**:010701.

Edenhofer, O., R. Pichs-Madruga, Y. Sokona, K. Seyboth, P. Matschoss, S. Kadner, T. Zwickel, P. Eickemeier, G. Hansen, S. Schlömer, and C. von Stechow. 2012. Renewable energy sources and climate change mitigation: Special report of the intergovernmental panel on climate change. *Cambridge University Press.*

Ernst, D., P. T. Bonoli, P. J. Catto, W. Dorland, C. L. Fiore, R. S. Granetz, M. Greenwald, A. E. Hubbard, M. Porkolab, M. H. Redi, J. E. Rice, K. Zhurovich, and Alcator C-Mod Group. 2004. Role of trapped electron mode turbulence in internal transport barrier control in the alcator c-mod tokamak. *Phys. Plasmas* **11**:2637.

Ernst, D. R., N. Basse, W. Dorland, C. L. Fiore, L. Lin, A. Long, M. Porkolab, K. Zeller, and K. Zhurovich. 2006. Identification of tem turbulence through direct comparison of nonlinear gyrokinetic simulations with phase contrast imaging density fluctuation measurements. *Proc. 21st IAEA Fusion Energy Conf.* IAEA-CN-149/TH/1-3.

Ernst, D. R., J. Lang, W. M. Nevins, M. Hoffman, Y. Chen, W. Dorland, and S. Parker. 2009. Role of zonal flows in trapped electron mode turbulence through nonlinear gyrokinetic particle and continuum simulation. *Phys. Plasmas* **16**:055906.

Evans, T. E., R. A. Moyer, K. H. Burrell, M. E. Fenstermacher, I. Joseph, A. W. Leonard, T. H. Osbourne, G. D. Porter, M. J. Schaffer, P. B. Snyder, P. R. Thomas, J. G. Watkins, and W. P. West. 2006. Edge stability and transport control with resonant magnetic perturbations in collisionless tokamak plasmas. *Nat. Physics* **2**:419-423.

Faber, B. J., M. J. Pueschel, J. H. E. Proll, P. Xanthopoulos, P. W. Terry, C. C. Hegna, G. M. Weir, K. M. Likin, and J.N. Talmadge. 2015. Gyrokinetic studies of trapped electron mode turbulence in the helically symmetric experiment stellarator. *Phys. Plasmas* **22**:072305.

Faber, B. J., M. J. Pueschel, P. W. Terry, C. C. Hegna, and J. E. Roman. 2018. Stellarator microinstabilities and turbulence at low magnetic shear. *Journal of Plasma Physics* **84**:5.

Finn, J. M., and J .F. Drake. 1984. Magnetic curvature-drift instability. *Phys. Rev. Lett.* **53**:24.

Fitzpatrick, R. 1993. Interaction of tearing modes with external structures in cylindrical geometry (plasma). *Nuclear Fusion* **33**:1049.

———. 1995. Helical temperature perturbations associated with tearing modes in tokamak plasmas. *Phys. Plasmas* **2**:825.

Fraser, A. E., M. J. Pueschel, P. W. Terry, and E. G. Zweibel. 2018. Role of stable modes in driven shear-flow turbulence. *Phys. Plasmas* **25**:122303.

Freidberg, J. P. 2014. *Ideal mhd.* Cambridge University Press.

Frieman, E. A., and L. Chen. 1982. Nonlinear gyrokinetic equations for lowâŁłfrequency electromagnetic waves in general plasma equilibria. *Phys. Fluids* **25**:502.

Furth, H. P., J. Killeen, and M. N. Rosenbluth. 1963. Finite resistivity instabilities of a sheet pinch. *Phys. Fluids* **6**:4.

Galperin, B., and P. L. Read. 2019. *Zonal jets: Phenomenology, genesis, and physics.* Cambridge University Press.

Gladd, N. T., J. F. Drake, C. L. Chang, and C. S. Liu. 1980. Electron temperature gradient driven microtearing mode. *Phys. Fluids* **23**:1182.

Goldston, R. J., and P. H. Rutherford. 1995. *Introduction to plasma physics.* CRC Press.

Hahm, T. S. 1988. Nonlinear gyrokinetic equations for tokamak microturbulence. *Phys. Fluids* **31**:2670.

Hammett, G. W., and F. W. Perkins. 1990. Fluid moment models for landau damping with application to the ion-temperature-gradient instability. *Phys. Rev. Lett.* **64**:3019.

Hastie, R. J., A. Sykes, M. Turner, and J. A. Wesson. 1977. Stabilization of tearing modes in tokamaks. *Nucl. Fusion* **17**:513.

Hatch, D. R., M. Kotschenreuther, S. Mahajan, P. Valanju, F. Jenko, D. Told, T. Görler, and S. Saarelma. 2016. Microtearing turbulence limiting the jet-ilw pedestal. *Nucl. Fusion* **56**:104003.

Hatch, D. R., M. J. Pueschel, F. Jenko, W. M. Nevins, P. W. Terry, and H. Doerk. 2012. Origin of magnetic stochasticity and transport in plasma microturbulence. *Phys. Rev. Lett.* **108**:235002.

Hazeltine, R. D., D. Dobrott, and T. S. Wang. 1975. Kinetic theory of tearing instability. *Phys. Fluids* **18**:1778.

Hegna, C. C., P. W. Terry, and B. J. Faber. 2018. Theory of itg turbulent saturation in stellarators: Identifying mechanisms to reduce turbulent transport. *Phys. Plasmas* **25**:022511.

Helander, P., T. Bird, F. Jenko, R. Kleiber, G. G. Plunk, J. H. E. Proll, J. Riemann, and P. Xanthopoulos. 2015. The universal instability in general geometry. *Phys. Plasmas* **22**:072305.

Hernandez, V., J. E. Roman, and V. Vidal. 2005. Slepc: A scalable and flexible toolkit for the slution of eigenvalue problems. *ACM Trans. Math. Softw.* **31**:3.

Ho, Y. L. 1991. Numerical simulation of fluctuation suppression via DC helicity injection in a reversed field pinch. *Nucl. Fusion* **31**:341.

Holland, C. 2016. Validation metrics for turbulent plasma transport. *Phys. Plasmas* **23**:060901.

Holland, C., and P. H. Diamond. 2004. A simple model of interactions between electron temperature gradient and drift-wave turbulence. *Phys. Plasmas* **11**:1043.

Holland, C., P. H. Diamond, S. Champeaux, E. Kim, O. Gurcan, M. N. Rosenbluth, G. R. Tynan, N. Crocker, W. Nevins, and J. Candy. 2003. Investigations of the role of nonlinear couplings in structure formation and transport regulation: experiment, simulation, and theory. *Nucl. Fusion* **43**:761.

Holod, I., Z. Lin, S. Taimourzadeh, R. Nazikian, D. Spong, and A. Wingen. 2017. Effect of resonant magnetic perturbations on microturbulence in diii-d pedestal. *Nucl. Fusion* **57**:016005.

Hornsby, W. A., P. Migliano, R. Buchholz, S. Grosshauser, A. Weikl, D. Zarzoso, F. J. Casson, E. Poli, and . G. Peeters. 2015. The nonlinear evolution of the tearing mode in electromagnetic turbulence using gyrokinetic simulations. *Plasma Phys. Control. Fusion* **58**:104028.

Horton, W., D. I. Choi, and W. M. Tang. 1981. Toroidal drift modes driven by ion pressure gradients. *Phys. Fluids* **24**:1077.

Howard, N. T., C. Holland, A. E. White, M. Greenwald, , and J. Candy. 2016. Multi-scale gyrokinetic simulations: Comparison with experiment and implications for predicting turbulence and transport. *Nucl. Fusion* **56**:014004.

Ishizawa, A., and N. Nakajima. 2007. Multi-scale-nonlinear interactions among micro-tearing, double tearing instability and zonal flows. *Nucl. Fusion* **47**:15401551.

Jenko, F., W. Dorland, M. Kotschenreuther, and B. N. Rogers. 2000. Electron temperature gradient driven turbulence. *Phys. Plasmas* **7**:1904.

Lapillonne, X., S. Brunner, T. Dannert, S. Jolliet, A. Marinoni, T. Görler L. Villard, F. Jenko, and F. Merz. 2009. Clarifications to the limitations of the s-α equilibrium model for gyrokinetic computations of turbulence. *Phys. Plasmas* **16**:032308.

Lawson, J. D. 1957. Some criteria for a power producing thermonuclear reactor. *Proc. Phys. Soc. B* **70**:6.

Liewer, P. C. 1985. Measurements of microturbulence in tokamaks and comparisons with theories of turbulence and anomalous transport. *Nucl. Fusion* **25**:543-621.

Littlejohn, R. G. 1981. Hamiltonian formulation of guiding center motion. *Phys. Fluids* **24**:1730.

Maeyama, S., Y. Idomura, T. H. Watanabe, M. Nakata, M. Yagi, N. Miyato, A. Ishizawa, , and M. Nunami. 2015. Cross-scale interactions between electron and ion scale turbulence in a tokamak plasma. *Phys. Rev. Lett.* **114**:255002.

Makwana, K. D., P. W. Terry, and J. H. Kim. 2012. Role of stable modes in zonal flow regulated turbulence. *Phys. Plasmas* **19**:062310.

Makwana, K. D., P. W. Terry, J. H. Kim, and D. R. Hatch. 2011. Damped eigenmode saturation in plasma fluid turbulence. *Phys. Plasmas* **18**:012302.

Makwana, K. D., P. W. Terry, M. J. Pueschel, and D. R. Hatch. 2014. Subdominant modes in zonal-flow-regulated turbulence. *Phys. Rev. Lett.* **112**:095002.

McDevitt, C. J., and P. H. Diamond. 2006. Multiscale interaction of a tearing mode with drift wave turbulence: A minimal self-consistent model. *Phys. Plasmas* **13**:032302.

McKee, G. R., R. J. Fonck, C. Holland, G. R. Tynan, K. H. Burrell, J. Candy, P. H. Diamond, K. Hallatschek, D. K. Gupta, F. L. Hinton, J. E. Kinsey, D. J. Schlossberg, M. W. Shafer, R. E. Waltz, and J. Yu. 2006. Characterization of zonal flows and their dynamics in the diii-d tokamak, laboratory plasmas, and simulation. *Proc. 21st IAEA Fusion Energy Conf.*

McKee, G. R., Z. Yan, C. Holland, R. J. Buttery, T. E. Evans, R. A. Moyer, S. Mordijck, R. Nazikian, T. L. Rhodes, and O. Schmitz. 2013. Increase of turbulence and transport with resonant magnetic perturbations in elm-suppressed plasmas on DIII-D. *Nucl. Fusion* **53**:113011.

Merz, F. 2008. Gyrokinetic simulation of multimode plasma turbulence. *Ph. D. Thesis, Westfälischen Wilhelms-Universität Münster.*

Miller, G. 1989. Nonlinear tearing modes in the reversed field pinch. *Phys. Fluids B* **1**:384.

Nevins, W. M., E. Wang, and J. Candy. 2011. Magnetic stochasticity in gyrokinetic simulations of plasma microturbulence. *Phys. Rev. Lett.* **106**:065003.

Nishizawa, T., M. D. Nornberg, D. J. Den Hartog, and D. Craig. 2016. Upgrading a high-throughput spectrometer for high-frequency (<400 khz) measurements. *Rev. Sci. Instrum.* **87**:11E530.

Nishizawa, T. and A. .F. Almagri, J. K. Anderson, W. Goodman, M. J. Pueschel, M. D. Nornberg, S. Ohshima, J. S. Sarff, P. W. Terry, and Z. R. Williams. 2019. Direct measurement of a toroidally directed zonal flow in a toroidal plasma. *Phys. Rev. Lett.* **122**:105001.

Petschek, H. E. 1964. Magnetic field annihilation. *NASA Special Publication* **50**:425.

Porcelli, F. 1991. Collisionless m=1 tearing mode. *Phys. Rev. Lett.* **66**:425.

Predebon, I., and F. Sattin. 2013. On the linear stability of collisionless microtearing modes. *Phys. Plasmas* **20**:040701.

Predebon, I., F. Sattin, M. Veranda, D. Bonfiglio, and S. Cappello. 2010. Microtearing modes in reversed field pinch plasmas. *Phys. Rev. Lett.* **105**.

Predebon, I., and P. Xanthopoulos. 2015. Ion temperature gradient turbulence in helical and axisymmetric rfp plasmas. *Phys. Plasmas* **22**:052308.

Pueschel, M. J., B. J. Faber, J. Citrin, C. C. Hegna, P. W. Terry, and D. R. Hatch. 2016. Stellarator turbulence: Subdominant eigenmodes and quasilinear modeling. *Phys. Rev. Lett* **116**:085001.

Pueschel, M. J., T. Görler, F. Jenko, D. R. Hatch, and A. J. Cianciara. 2013a. On secondary and tertiary instability in electromagnetic plasma microturbulence. *Phys. Plasmas* **20**:102308.

Pueschel, M. J., D. R. Hatch, T. Görler, W. M. Nevins, F. Jenko, P. W. Terry, and D. Told. 2013b. Properties of high-β microturbulence and the non-zonal transition. *Phys. Plasmas* **20**:102301.

Pueschel, M. J., F. Jenko, D. Told, and J. Büchner. 2011. Gyrokinetic simulations of magnetic reconnection. *Phys. Plasmas* **18**:112102.

Pueschel, M. J., P. W. Terry, F. Jenko, D. R. Hatch, W. M. Nevins, T. Görler, and D. Told. 2013c. Extreme heat fluxes in gyrokinetic simulations: A new critical β. *Phys. Rev. Lett.* **110**:155005.

Rechester, A. B., and M. N. Rosenbluth. 1978. Electron heat transport in a tokamak with destroyed magnetic surfaces. *Phys. Rev. Lett.* **40**:38.

Rewoldt, G., and W. M. Tang. 1990. Toroidal microinstability studies of high temperature tokamaks. *Phys. Fluids B* **2**:318.

Rogers, B. N., W. Dorland, and M. Kotschenreuther. 2000. Generation and stability of zonal flows in ion-temperature-gradient mode turbulence. *Phys. Rev. Lett.* **85**:5336.

Rosenbluth, M. N., and F. L. Hinton. 1998. Poloidal flow driven by ion-temperature-gradient turbulence in tokamaks. *Phys. Rev. Lett.* **80**:724.

Sarff, J. S., S. A. Hokin, H. Ji, S. C. Prager, and C. R. Sovinec. 1994. Fluctuation and transport reduction in a reversed field pinch by inductive poloidal current drive. *Phys. Rev. Lett.* **72**:3670.

Scott, B. D., A. B. Hassam, and J. F. Drake. 1985. Nonlinear evolution of driftâŁłtearing modes. *Phys. Fluids* **28**:275.

Sovinec, C. R. 1995. *Ph. D. Thesis, University of Wisconsin-Madison.*

Sugama, H ., and T.-H. Watanabe. 2006. Collisionless damping of zonal flows in helical systems. *Phys. Plasmas* **13**:012501.

Swamy, A. K., R. Ganesh, J. Chowdhury, S. Brunner, J. Vaclavik, and L. Villard. 2014. Global gyrokinetic stability of collisionless microtearing modes in large aspect ratio tokamaks. *Phys. Plasmas* **21**:082513.

Tangri, V., P. W. Terry, and R. E. Waltz. 2011. A circular equilibrium model for local gyrokinetic simulations of ion temperature gradient fluctuations in reversed field pinches. *Phys. Plasmas* **18**:052310.

Terry, P. W. 2000. Suppression of turbulence and transport by sheared flow. *Rev. Mod. Phys.* **72**:109.

Terry, P. W., D. A. Baver, and S. Gupta. 2006. Role of stable eigenmodes in saturated local plasma turbulence. *Phys. Plasmas* **13**:022307.

Terry, P. W., D. A. Baver, and D. R. Hatch. 2009. Reduction of inward momentum flux by damped eigenmodes. *Phys. Plasmas* **16**:122305.

Terry, P. W., D. Carmody, H. Doerk, W. Guttenfelder, D. R. Hatch, C. C. Hegna, A. Ishizawa, F. Jenko, W. M. Nevins, I. Predebon, M. J. Pueschel, J. S. Sarff, and G. G. Whelan. 2015. Overview of gyrokinetic studies of finite- β microturbulence. *Nucl. Fusion* **55**:104011.

Terry, P. W., R. Gatto, and D. A. Baver. 2002. Nonlinear damping of plasma zonal flows excited by inverse spectral transfer. *Phys. Rev. Lett.* **89**:205001.

Terry, P. W., M. J. Pueschel, D. Carmody, and W. M. Nevins. 2013. The effect of magnetic flutter on residual flow. *Phys. Plasmas* **20**:112502.

Thuecks, D. J., A. F. Almagri, J. S. Sarff, and P. W. Terry. 2017. Evidence for drift waves in the turbulence of reversed field pinch plasmas. *Phys. Plasmas* **24**:022309.

Told, D., F. Jenko, T. Görler, F.J. Casson, E. Fable, and ASDEX Upgrade Team. 2013. Characterizing turbulent transport in asdex upgrade l-mode plasmas via nonlinear gyrokinetic simulations. *Phys. Plasmas* **20**:122312.

Walker, J., S. Boldyrev, and N. F. Loureiro. 2018. Influence of tearing instability on magnetohydrodynamic turbulence. *Phys. Rev. E* **98**:033209.

Waltz, R. E., M. E. Austin, K. H. Burrell, and J. Candy. 2006. Gyrokinetic simulations of off-axis minimum-q profile corrugations. *Phys. Plasmas* **13**:052301.

Watanabe, T.-H., H. Sugama, and S. Ferrando-Margalet. 2008. Reduction of turbulent transport with zonal flows enhanced in helical systems. *Phys. Rev. Lett.* **100**:195002.

Whelan, G. G., M. J. Pueschel, and P. W. Terry. 2018. Nonlinear electromagnetic stabilization of plasma microturbulence. *Phys. Rev. Lett.* **120**:175002.

Williams, Z. R., M. J. Pueschel, P. W. Terry, and T. Hauff. 2017. Turbulence, transport, and zonal flows in the madison symmetric torus reversed-field pinch. *Phys. Plasmas* **24**:122309.

Winsor, N., J. L. Johnson, and J. M. Dawson. 1968. Geodesic acoustic waves in hydromagnetic systems. *Phys. Fluids* **11**:2448.

BP Statistical Review of World Energy. 2018.

Xanthopoulos, P., W. A. Cooper, F. Jenko, Yu. Turkin, A. Runov, and J. Geiger. 2009. A geometry interface for gyrokinetic microturbulence investigations in toroidal configurations. *Phys. Plasmas* **16**:082303.